3D Single Molecule Imaging In Whole Cells Enabled By Lattice Light-Sheet Illumination

Dissertation zur Erlangung
des naturwissenschaflichen Doktorgrades
der Julius-Maximilians-Universität
Würzburg

vorgelegt von

Felix Wäldchen

aus Gießen

Würzburg, 2019

Eingereicht am: 23.05.2019
bei der Fakultät für Physik und Astronomie.

1. Gutachter: Prof. Dr. Markus Sauer
2. Gutachter: Prof. Dr. Bert Hecht
3. Gutachter: .....
der Dissertation.

Vorsitzender: Prof. Dr. Matthias Bode

1. Prüfer: Prof. Dr. Markus Sauer
2. Prüfer: Prof. Dr. Bert Hecht
3. Prüfer: Prof. Dr. Matthias Kadler
im Promotionskolloquium.

Tag des Promotionskolloquiums: 01.07.2020

Doktorurkunde ausgehändigt am: .....

To my wife, Sina

Abstract

Single molecule localization microscopy has seen a remarkable growth since its first experimental implementations about a decade ago. Despite its technical challenges, it is already widely used in medicine and biology and is valued as a unique tool to gain molecular information with high specificity. However, common illumination techniques do not allow the use of single molecule sensitive super-resolution microscopy techniques such as direct stochastic optical reconstruction microscopy (*d*STORM) for whole cell imaging. In addition, they can potentially alter the quantitative information.

In this thesis, I combine *d*STORM imaging in three dimensions with lattice light-sheet illumination to gain quantitative molecular information from cells unperturbed by the illumination and cover slip effects. Lattice light-sheet illumination uses optical lattices for beam shaping to restrict the illumination to the detectable volume. I describe the theoretical background needed for both techniques and detail the experimental realization of the system as well as the software that I developed to efficiently evaluate the data.

Eventually, I will present key datasets that demonstrate the capabilities of the developed microscope system with and without *d*STORM. My main goal here was to use these techniques for imaging the neural cell adhesion molecule (NCAM, also known as CD56) in whole cells. NCAM is a plasma membrane receptor known to play a key role in biological processes such as memory and learning. Combining *d*STORM and lattice light-sheet illumination enables the collection of quantitative data of the distribution of molecules across the whole plasma membrane, and shows an accumulation of NCAM at cell-cell interfaces. The low phototoxicity of lattice light-sheet illumination further allows for tracking individual NCAM dimers in living cells, showing a significant dependence of its mobility on the actin skeleton of the cell.

Zusammenfassung

Die Einzelmoleküllokalisationsmikroskopie hat seit der ersten experimentellen Umsetzung vor etwa 10 Jahren einen bemerkenswerten Aufschwung erfahren. Trotz des hohen technischen Anspruchs findet sie bereits weite Verbreitung in der Biologie und Medizin und wird als einzigartiges Werkzeug geschätzt, um molekulare Information mit hoher Spezifität zu erlangen. Dennoch erschweren die gebräuchlichen Beleuchtungsmethoden die Anwendung von Methoden der Einzelmoleküllokalisationsmikroskopie wie *d*STORM (*engl.* direct stochastic optical reconstruction microscopy) auf das Volumen ganzer Zellen, denn hier kann die Beleuchtung selbst die quantitativen Daten beeinflussen.

In dieser Arbeit kombiniere ich dreidimensionale *d*STORM-Bildgebung mit Gitterlichtblattbeleuchtung (*engl.* lattice light-sheet illumination) um quantitative, molekulare Information ohne durch die Beleuchtung verursachte Störungen zu gewinnen. Die Gitterlichtblattbeleuchtung nutzt optische Gitter zur Strahlformung, um das beleuchtete Volumen auf das detektierbare Volumen zu beschränken. Ich stelle den nötigen, theoretischen Hintergrund für beide Methoden dar und beschreibe die experimentelle Umsetzung sowie die von mir zur effizienten Datenauswertung entwickelte Software.

Schließlich präsentiere ich verschiedene Datensätze, die die Fähigkeiten des Systems mit und ohne *d*STORM demonstrieren. Mein Hauptziel war hierbei, beide Methoden zu nutzen, um das neuronale Zelladhäsionsmolekül (NCAM, *engl.* neural cell adhesion molecule) in ganzen Zellen abzubilden. NCAM (auch bekannt als CD56) ist ein Rezeptor auf der Plasmembran, der für seine Schlüsselrolle im Zusammenhang mit biologischen Prozessen wie Lernen und Gedächtnis bekannt ist. Die Kombination von *d*STORM und Gitterlichtblattbeleuchtung ermöglicht das sammeln quantitativer Daten der Verteilung über die komplette Plasmamembran, wobei sich eine Akkumulation an Zell-Zell Kontaktflächen zeigt. Die niedrige Photoschädigung der Gitterlichtblattbeleuchtung ermöglicht weiterhin das Verfolgen von einzelnen NCAM-Dimeren in lebenden Zellen. Dort zeigt sich eine signifikante Abhängigkeit ihrer Mobilität vom Aktinskelett der Zelle.

Contents

1 Introduction

The invention of the microscope at the turn of the 15^{th} to the 16^{th} century marks a turning point in the history of science. Viewing small objects at high magnification gave access to a new world that had been invisible to human eyes so far. Soon, microorganisms, blood cells, yeast and spermatozoa were described by *Antony van Leeuvenhoek* using his microscopes, thereby laying the foundations of microbiology. In general, being able to observe an object of interest with one's own eyes by the help of an optical system is a very powerful insight experience.

However, the performance of microscopes was entirely dependent on the craftsmanship and experience of the technician building the microscope. This changed when *Ernst Abbe* provided the first comprehensive approach to the theory of physical optics and optical aberrations in 1873 [Abb73]. In the history of microscopy, the field of physics has always fruitfully interacted with biology and medicine to improve the method that then enabled new insights with unprecedented detail. Some prime examples are the invention of Köhler illumination (*August Köhler*, 1893), phase contrast (*Frits Zernike*, 1933) and differential interference contrast (*Georges Nomarski*, 1952).

More recently, the use of fluorescent dyes as stains for biological structures has enabled light microscopy to provide highly specific images of biological ultrastructure. However, the resolution of a microscope is ultimately limited by the wavelength of light, setting a limit to the detail one can discern in a given specimen. Circumventing this "diffraction barrier" in far-field microscopy started with first efforts in the 1990's with various concepts to separate the light emission of single molecules [MK89; Bet95; van+98]. Yet, it took over a decade to create viable solutions that work on biological samples, marking the advent of super-resolution microscopy [RBZ06; Bet+06; Hei+08].

Direct stochastic optical reconstruction microscopy (*d*STORM) is one of those methods that circumvent the diffraction barrier. By separating the emission of

individual fluorescent dyes in time, it is possible to localize them with high precision, well below the diffraction limit. *d*STORM makes it possible to reconstruct images of the underlying structure with a resolution approaching molecular dimensions. This enables observing completely new targets in biology and medicine, such as single receptors on cell surfaces.

At the same time, the illumination used for sophisticated super-resolution techniques did not evolve as rapidly. Commonly employed techniques allow illuminating either small volumes very close to the glass surface or the whole sample with a column of light. This leads to several adverse effects, since the illuminated volume is much bigger than the slice of the specimen that can be imaged. First, in living specimen this causes unnecessary high levels of phototoxicity due to the high light dose. Secondly, high background levels and poor signal-to-noise ratios are generated, since regions that do not contribute to the microscopic image are illuminated.

Lately, light-sheet illumination has been introduced to fluorescence microscopy to address this issue [HS09]. The basic idea was introduced by *Siedentopf* and *Zsigmondy* in 1902, who used it to observe colloidal particles in solution [SZ02]. Here, a separate set of optics is employed to illuminate the sample through another objective, that is positioned perpendicular to the microscope objective. This allows for only illuminating the slice of the sample that can be viewed at the same time. For microscopes with low magnification, such as the ones used for observing whole organisms, this slice is quite thick and the requirements to the light-sheet are not very strict. However, when using a microscope with high magnification, the observable volume (depth of field) is quite thin, making sophisticated beam-shaping optics for the light-sheet illumination necessary. In lattice light-sheet illumination microscopy (LLSM), optical lattices are generated to produce a light-sheet that meets these strict requirements [Che+14].

In this thesis, I combine *d*STORM with lattice light-sheet illumination to benefit from superior signal-to-noise and localize single molecules throughout the whole cell in three dimensions. By only illuminating the volume that can be observed at the same time, unperturbed imaging of single molecules is ensured. First, I will detail the complex theory behind both methods, before I describe the experimental realization, including the discussion of specific light-sheets for *d*STORM that I simulated. Since LLSM allows for imaging big volumes very rapidly, the amount of data that it produced is often in the TB range and requires dedicated strategies

to efficiently evaluate it. To this end, I have developed a Python package called "lls-tools" that acts as a bridge between other established software and carries out operations specific to LLSM. Finally, I will showcase various samples I imaged with the LLSM in both conventional as well as *d*STORM detection mode.

In this context, imaging CD56 receptors on the whole plasma membrane of cells was a major goal during this thesis. In general, receptors on the plasma membrane of cells are responsible for modulating cellular processes and act as a link to the outside world. The molecular organization and distribution of the receptors on the membrane is crucial to their functionality. This is why plasma membrane receptors have been studied since the beginning of the 20^{th} century and many drugs have been found that specifically target a certain receptor, leading to well established therapies [OAH06]. Since the advent of single molecule localization microscopy (SMLM), this technique was successfully used to study receptors and gain quantitative information [SH17].

CD56 receptors, also known as neural cell adhesion molecule (NCAM), is expressed by natural killer cells and plays an important role in pathogen recognition. It is involved in many fundamental biological processes, such as cell-cell adhesion, learning and memory [Zie+17].

Commonly, single molecule imaging of receptors is performed at the basal membrane [Ros+13; Bau+16]. Here, high-NA oil immersion objectives together with TIRF illumination can be used to their full potential, since the receptors are close to the cover slip. However, the glass surface and coatings that help the cells adhere can potentially alter the spatial distribution as well as the dynamics of membrane receptors [HCL16; Pon+18]. This makes imaging away from the cover slip necessary. Here, lattice light-sheet illuminations with *d*STORM plays a key role in providing unperturbed imaging of the whole plasma membrane receptor distribution.

Moreover, reducing the illumination volume to the required minimum with LLSM allows for tracking individual CD56 receptor on the apical side of the plasma membrane with minimal phototoxic effect to the cell. This enables studying the dependence of their dynamics on the underlying actin skeleton of the cell.

Apart from presenting my own work, I also hope to enable others to continue operating the LLSM in combination with *d*STORM successfully.

2 Theoretical Foundations

> If I have seen further it is by standing on the shoulders of Giants.
>
> *(Newton, 1675)*

Lattice light-sheet microscopy (LLSM) and single molecule localization with *direct* stochastic optical reconstruction microscopy (*d*STORM), the methods that form the foundation of this thesis, are highly sophisticated. Hence, the theory that empowers these methods is quite vast. Although impossible to cover the theory in all its detail within the scope of this work, in this chapter I will outline the most important aspects and provide references for further reading.

I will begin by presenting the physics behind the phenomenon of fluorescence that has been proven so valuable to optical science. Then, I will introduce the reader to the principles of geometrical optics that are necessary to understand the function of a simple microscope and the basic beam path of the LLSM. Following, I will expand the optical theory to Fourier optics that fully handles the wave nature of light and introduces the peculiarity of the diffraction limit that restricts the achievable resolution in conventional microscopes. Nevertheless, several techniques have been developed in the past 10 years that allow for a circumvention of this limit. They will be discussed in more detail in chapter 2.4 together with their application to three dimensions. Finally, I will address different concepts of illumination for single molecule detection. In this context, the theory of optical lattices is of special importance to my thesis and will be presented in chapter 2.5.2 in the hope of elucidating its benefits for light-sheet microscopy to the reader. While this chapter might be too detailed for an experienced optical physicist, I also hope to provide insight into the LLSM theory to readers coming from a slightly different background.

2.1. Fluorescence

The phenomenon of fluorescence has seen a remarkable growth in the past three decades. First, fluorescence spectroscopy and time-resolved fluorescence have been established as important research tools in biochemistry and biophysics. Nowadays, the use of fluorescence has expanded across different fields of research. The specificity of fluorescence signals allowed it to replace proven methods for the most part, such as tracing of radioactive markers. This came hand-in-hand with increased detection efficiency due to newly developed sophisticated instruments. Now, fluorescence is widely used in biotechnology, flow cytometry, medical diagnostics, DNA sequencing, forensics and genetic analysis [Lak06].

The history of fluorescence goes back to *Herschel* and *Stokes*. Interestingly, like many other things that came to microscopy, the phenomenon of fluorescence was also discovered by an astronomer. In 1845, *Herschel* published two papers, marking the first observation of fluorescence in quinine solution [Her45a; Her45b]. He noted that this transparent solution, when exposed to sunlight, exhibits a blue shine where the sunlight enters the liquid. With the scientific knowledge of that time, this phenomenon could not be explained. Seven years later, *Stokes* had expanded these experiments considerably [Sto52]. Using different pieces of colored glass, he was able to detect a shift in wavelength between the incoming light and the emitted light. This shift is called the *Stokes shift* and its origination will be explained subsequently.

Light interacts with matter in very specific ways. When matter is exposed to an electromagnetic light wave, the energy can be absorbed and the affected atoms or molecules can be excited. *Einstein* proofed, that the energy arrives in well-defined quanta, called photons [Ein05]:

$$E = h\frac{c}{\lambda} = h\nu \tag{2.1}$$

Here, $h \approx 6.626 \times 10^{-34}\,\mathrm{Js}$ is the *Planck* constant, c is the speed of light, λ is its wavelength and ν its frequency, respectively. It is worth noting that for visible light, as it is used in this work, wavelengths range from 400 nm to 700 nm and thus the energy per photon is in the range of 3.1 eV to 1.8 eV, respectively.

The energy levels of an atom are defined by its electronic structure, i.e. the

distribution of its electrons in space as solutions to the *Schrödinger Equation*. For this work, however, considering molecules is much more relevant. In molecules, additional energy levels are present due to vibrational and rotational degrees of freedom (DOF). These energy levels superimpose the electronic energy levels.

Rotational and vibrational energy levels typically have an energy difference of µeV and meV, respectively, whereas electronic energy level differences are in the order of eV [Dem13]. In an ensemble of molecules, the *Boltzmann* factor gives the ratio of occupation of different energy levels

$$\frac{N_i}{N_j} = e^{-\frac{E_i - E_j}{kT}} \quad , \tag{2.2}$$

where N denotes the respective number of molecules occupying a certain energy state, E denotes the respective energy of those states, $k \approx 8.62 \times 10^{-5}\,\mathrm{eV/K}$ is the *Boltzmann* constant and T the temperature. This immediately lets us appreciate, that at room temperature, only rotational and vibrational DOF are occupied. However, considering energy differences of eV, we immediately see that those energy levels are not thermally populated

$$\frac{N_i}{N_j} \sim 10^{-18} \quad \text{for } E_i - E_j = 1\,\mathrm{eV} \text{ and } T = 300\,\mathrm{K} \tag{2.3}$$

and are thus left to optical excitation.

Due to the fact that fluorescence mostly happens from the S_1 state, but absorption excites electrons to higher energy states, the fluorescence emission is red-shifted with respect to the excitation light. This is the origin of the *Stokes shift*.

To excite a molecule optically, the energy of an incoming photon must equal the energy difference between a populated state and a vacant state. In this case, the photon can be absorbed and the energy will lift an electron from the ground state S_0 to vibrational energy level of an excited state S_n. This is depicted in the *Jablonski* diagram (Figure 2.1). From there, it well relax to the lowest vibrational state. If the electron was excited to a state higher than S_1, usually an internal conversion to the lowest excited state S_1 occurs. For these radiation-free processes, the excess energy is absorbed into vibrational or rotational modes of molecule or other molecules around it. From S_1, the electron can go back to S_0 and emit the energy difference as a photon. This process is called fluorescence.

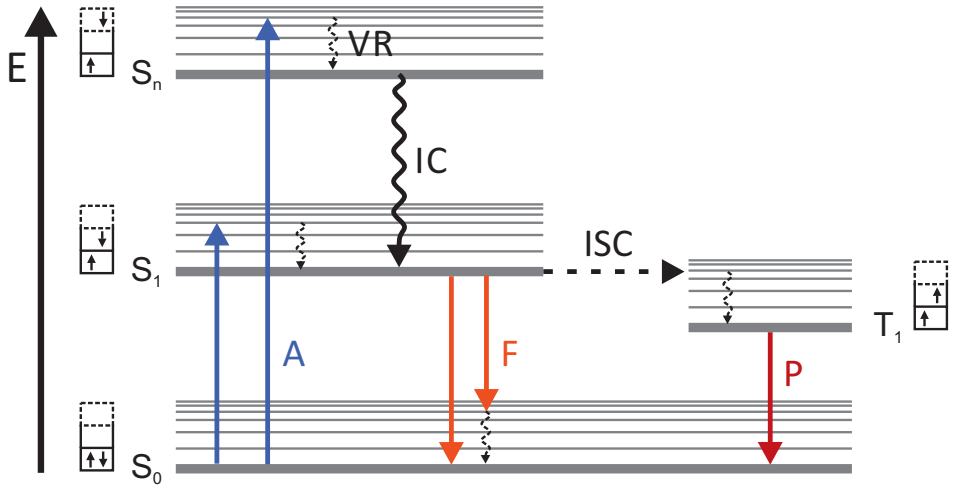

Figure 2.1.: Jablonski diagram, depicting molecular energy transitions leading to light emission (luminescence). An electron residing in the singlet ground state S_0 can be excited to a vibrational state of a higher electronic state S_1, S_n upon absorption (A) of a photon with appropriate energy. Vibrational relaxation (VR) to the lowest vibrational state occurs quickly and is, for $n > 1$, followed by internal conversion (IC) to the lowest vibrational state of S_1. From there, a radiative return to the ground state can happen, called fluorescence (F). Another possibility is intersystem crossing (ISC) to a more stable triplet state T_1, from where a radiative return to the ground state happens eventually. This transition is called phosphorescence (P).

Table 2.1.: Typical time scales of photophysical processes.

Transition	Denotation	Timescale [s]
$S_0 \rightarrow S_1 ... S_n$	Absorption	10^{-15}
$S_n \rightarrow S_1$	Internal Conversion	10^{-12}
$S_n \rightarrow S_n$	Vibrational Relaxation	10^{-12}
$S_1 \rightarrow S_0$	Fluorescence	10^{-9}
$S_1 \rightarrow T_1$	Intersystem Crossing	10^{-8}
$T_1 \rightarrow S_0$	Phosphorescence	$> 10^{-6}$

There is also a chance that the electron transits to the quantum-mechanically forbidden triple state T_1 via intersystem crossing [LC05]. From there, it will eventually also go back to the ground state S_0 while emitting a photon. The difference here is, that the T_1 state is very long lived compared to S_1, since the transition $T_1 \rightarrow S_0$ is also quantum-mechanically forbidden. The lifetime of T_1 can be up to

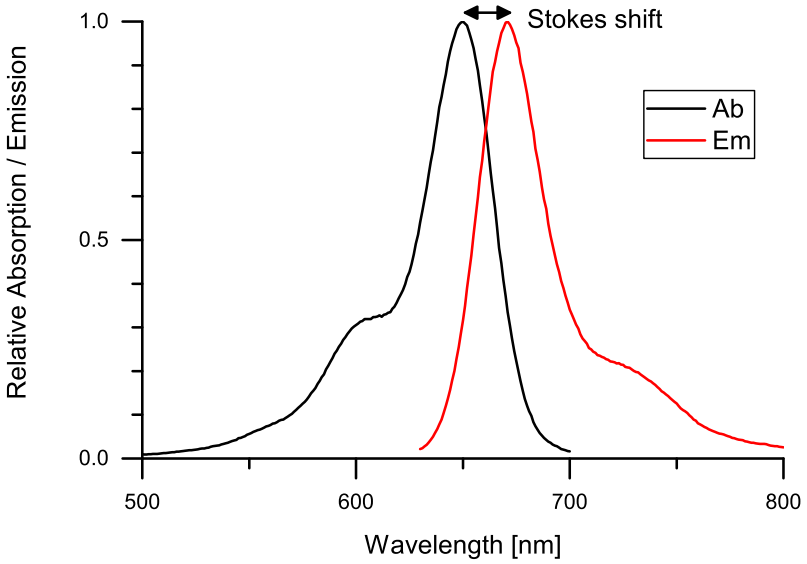

Figure 2.2.: Fluorescence spectrum of an organic dye, namely Alexa Fluor® 647. Absorption and emission spectra maxima are shifted by the Stokes shift. This allows for separation between scattered emission light and fluorescence in a microscope.

several seconds or even minutes to hours. The eventual decay is called phosphorescence. The typical time scales of the different processes mentioned in Figure 2.1 are summarized in Table 2.1.

In Figure 2.2, the spectrum of Alexa Fluor® 647 is depicted. This is a commonly used organic dye in super-resolution microscopy. The Stokes shift between the excitation and emission maxima is clearly visible. This shift is of major relevance for microscopy. When a structure of interest is labeled with a fluorescent dye (also called fluorophore), the fluorescence light can be separated based on its wavelength, i.e. by a dichroic beam splitter. This allows to discern between light that contains information about the structure and light that does not (i.e. scattered excitation light).

In summary, fluorescence microscopy can provide highly specific images of relevant biological structures with high signal-to-noise ratio (SNR) and is therefore a valuable tool in biology and medicine.

2.2. Prerequisites of Geometrical Optics

We already know that light exists as electromagnetic wave. Optics in general describes the propagation of electromagnetic waves through media and their behavior at interfaces between different media. However, in many situations, the wave nature of light can be ignored and using the rules of geometrical optics already allows great insight into the function of many optical devices. In many aspects, geometrical optics can be seen as an idealized approximation to wave optics when the wavelength of light is small compared to the physical dimensions of the optical system:

$$\lambda \ll d \tag{2.4}$$

In this chapter, I will revisit the formalism of geometrical optics and introduce the reader to important optical devices. Finally, I will review the primary aberations that can appear in optical devices. For an even deeper insight, I recommend the respective chapters in the book "Optics" by *Eugene Hecht* [Hec17]. For German readers, [Dem17] and [HM17] are also well worth a read. This chapter is inspired by these books.

2.2.1. Basic Principles

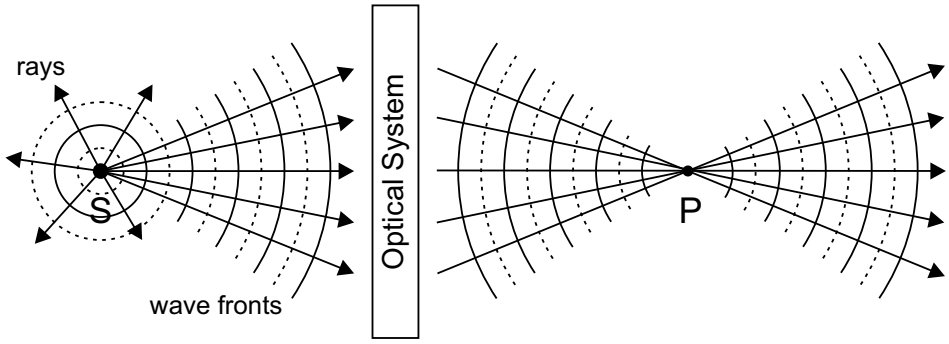

Figure 2.3.: Definition of light rays. A light source S emits light isotropically as spherical waves. A light ray is defined as orthonormal trajectory of the wavefronts, marking the direction of propagation in isotropic medium. An optical system can alter the direction of light rays, resulting in a convergence in point P in this example. In this case, the system is said to be stigmatic for points S and P. Inspired by [Hec17]

Whenever the wavelength of light becomes neglectable compared to the sizes of the physical structures in the system, the approximation of geometrical optics holds true. In this case, the propagation direction of light and its alteration by optical elements, such as mirrors and lenses, is sufficient to analyze a given system.

Let us consider a point source of light S that emits isotropically (Figure 2.3). Light rays are the orthonormal trajectories of the wavefronts. In isotropic medium, they coincide with the *Poynting* vector of the wave, that marks the direction of energy flow and the direction of propagation. For a small volume around each ray, we can approximate the electric field as a plane wave, since the curvature of the wave front inside the volume is neglectable. This leads us to the following basic principles of geometrical optics, that can be verified both experimentally and theoretically:

- In a homogeneous medium, light rays are straight lines.
- At the interface between two media, a light ray is reflected according to the law of reflection and refracted according to *Snell's law*.
- The direction of a ray can be reversed without changing its behavior in a system
- Two rays coinciding at the same point do not interfere with each other.

An optical system such as the one depicted in Figure 2.3 is called *stigmatic*. The diverging cone of rays emitted by a point source S is transformed into a converging cone of rays, that are *focused* in P.

Figure 2.4 highlights the two basic processes at optical interfaces. A light ray can be reflected by a surface (i.e. a mirror), in which case the angle of reflection equals the angle of incidence. If the light ray travels further into the second medium, it is refracted according to Snell's law:

$$n_1 \sin \alpha_1 = n_2 \sin \alpha_2 \tag{2.5}$$

When traveling into an optical denser medium ($n_2 > n_1$), the ray is refracted towards the surface normal. The refractive index is defined as the speed of light in

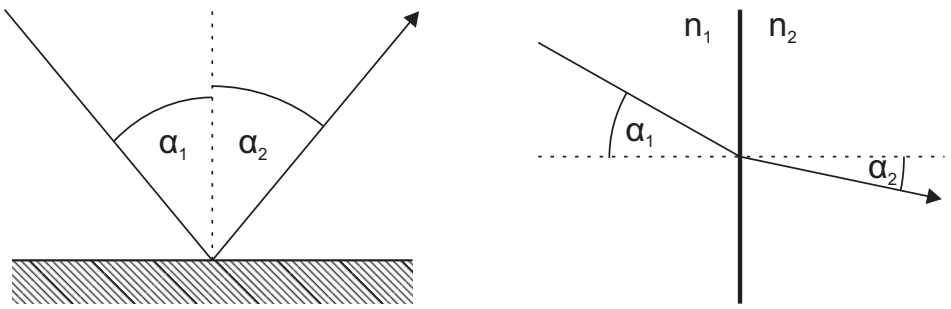

Figure 2.4.: Laws of reflection and refraction. (Left) An incoming light ray is reflected at a surface. The angle of incidence equals the angle of reflection, $\alpha_1 = \alpha_2$. (Right) A light ray is refracted at the interface of two media with refractive indexes n_1 and n_2, with $n_2 > n_1$. *Snell's law* states that $n_1 \sin\alpha_1 = n_2 \sin\alpha_2$.

vacuum c_0 compared to the speed of light in the medium c_m:

$$n_m = \frac{c_0}{c_m} \tag{2.6}$$

The refractive index depends on the wavelength of light for most materials, which makes designing optical systems with equal optical properties for a range of wavelengths challenging. Of course, reflection and refraction can happen at the same time, dividing the energy of the incoming beam into a reflected beam and a refracted beam. The exact ratio is described by the coefficients of reflection and transmission and depends on the angle of incidence and the polarization of the beam.

2.2.2. Lenses and the Paraxial Approximation

Before I introduce refraction at curved surfaces, such as lenses, I will establish *Fermat's principle*. It states that when considering all possible paths between two points S and P, a beam of light takes the one that is traversed in the least time. More precisely, I define the optical path length (OPL)

$$\mathrm{OPL} = \sum_i n_i s_i \ , \tag{2.7}$$

where n_i is the refractive index and s_i the distance traveled in a respective medium. Then, a beam of light takes the path that has the smallest OPL. We note that in

this case the derivative with respect to variations of that path must be zero.

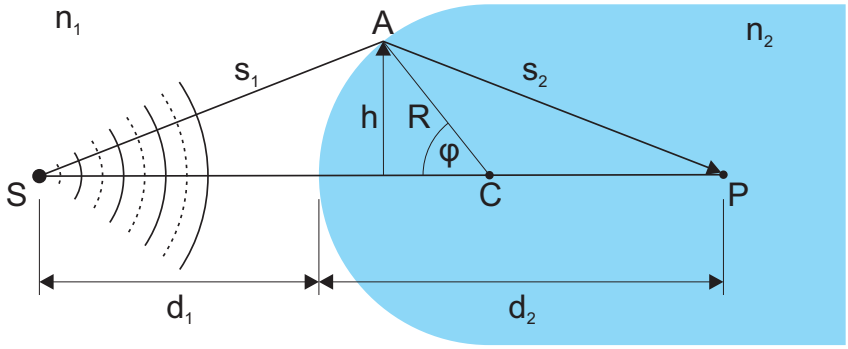

Figure 2.5.: Refraction at a spherical surface with refractive index $n_2 > n_1$. An arbitrarily chosen ray of light travels from the source S a distance s_1 to the spherical surface of radius R that is centered at C. There, it is refracted according to *Snell's law* and travels a distance s_2 towards point P on the optical axis.

Now let us again consider a light ray from a point emitter S, impinging on a spherical surface of different refractive index ($n_2 > n_1$). The surface has radius R and is centered at C. Since *Snell's law* tells us, that the ray will be refracted towards the surface normal, it will eventually arrive at a point P on the optical axis. The optical axis shall here be defined as the axis of rotational symmetry of the system. The OPL of the path to that point is

$$\mathrm{OPL} = n_1 s_1 + n_2 s_2 \quad . \tag{2.8}$$

Using the law of cosines on the triangles SAC and ACP immediately yields

$$\begin{aligned} s_1 &= \sqrt{R^2 + (d_1 + R)^2 - 2R\,(d_1 + R)\cos\varphi} \quad \text{and} \\ s_2 &= \sqrt{R^2 + (d_2 - R)^2 - 2R\,(d_2 - R)\cos\varphi} \quad . \end{aligned} \tag{2.9}$$

From *Fermat's principle* it follows, that the derivate with respect to φ must vanish:

$$\frac{d}{d\varphi}\mathrm{OPL} = \frac{n_1 R\,(d_1 + R)\sin\varphi}{2s_1} - \frac{n_2 R\,(d_2 - R)\sin\varphi}{2s_2} = 0 \tag{2.10}$$

$$\Leftrightarrow \frac{n_1}{s_1} + \frac{n_2}{s_2} = \frac{1}{R}\left(\frac{n_2 d_2}{s_2} - \frac{n_1 d_1}{s_1}\right) \tag{2.11}$$

Equation (2.11) is exact for any ray going from S to P, but rather complicated, since it depends on the distances s_1 and s_2 and thus on the point of incidence on the surface A. However, for rays close to the optical axis, φ is mall and therefore $s_i \approx d_i$, which simplifies (2.11) to

$$\frac{n_1}{d_1} + \frac{n_2}{d_2} = \frac{n_2 - n_1}{R} \quad . \tag{2.12}$$

This is called the *paraxial approximation* and rays that arrive at small angles with the optical axis are called *paraxial rays*. This concept is widely used in geometrical optics. It tells us, that any ray coming from the source point in a paraxial cone will eventually arrive at the same point P. More specifically, this means that the series expansion of the trigonometric functions are discarded after the first-order term:

$$\sin\varphi = \varphi - \frac{\varphi^3}{3!} + \frac{\varphi^5}{5!} + \mathcal{O}\left(\varphi^7\right) \approx \varphi \tag{2.13}$$

$$\cos\varphi = 1 - \frac{\varphi^2}{2!} + \frac{\varphi^4}{4!} + \mathcal{O}\left(\varphi^6\right) \approx 1 \tag{2.14}$$

$$\tan\varphi = \varphi + \frac{\varphi^3}{3} + \frac{2\varphi^5}{15} + \mathcal{O}\left(\varphi^7\right) \approx \varphi \tag{2.15}$$

The theory is therefore also called first-order theory. As a result, (2.12) is now independent of the location of A. In 1841, *Gauss* was the first to establish this theory and used it to design lenses theoretically for the first time. Hence it was also termed *Gaussian optics*. For the remainder of this and the following chapter, I will only be considering this approximation.

We can now further examine (2.12): Choosing $d_2 \to \infty$ corresponds to an image infinitely far away from the source or parallel rays propagating to the right in Figure 2.5. The object distance d_1 then becomes

$$f_o = d_1(d_2 \to \infty) = \frac{n_1}{n_2 - n_1} R \quad . \tag{2.16}$$

This distance is called the *object focal length* f_o and the corresponding point is named F_o. Likewise, we get the *image focal length* f_i by choosing $d_1 \to \infty$, which corresponds to parallel rays coming in from the left:

$$f_i = d_2(d_1 \to \infty) = \frac{n_2}{n_2 - n_1} R \tag{2.17}$$

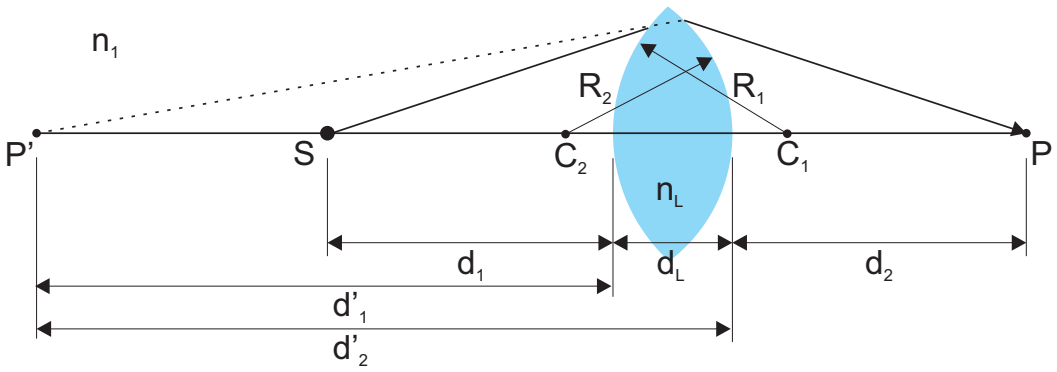

Figure 2.6.: Refraction by a spherical lens of refractive index n_L in surrounding medium with refractive index n_1. The two spherical surfaces have radii R_1 and R_2 and are centered at C_1 and C_2, respectively. A light ray coming from the source S is refracted at the first surface and then appears to the second surface as if coming from point P'. At the second surface it is finally refracted towards point P.

Finally, I can introduce the spherical lens. Spherical lenses are the most abundant lenses in modern optics, consisting of two spherical surface with radii R_1 and R_2. The reason why most lenses have spherical surfaces is not that they give the best performance, but because spherical surfaces are easy to manufacture and therefore cheaper[1]. Figure 2.6 shows such a lens. A ray starts from point S and is refracted at a first spherical surface with radius R_1 centered at C_1. To the second surface, it looks as if the ray would be coming undisturbed from point P'. The second surface has radius R_2, is centered at C_2 and refracts the ray towards point P on the optical axis. From (2.12) we get

$$\frac{n_1}{d_1} + \frac{n_L}{d_1'} = \frac{n_L - n_1}{R_1} \quad . \tag{2.18}$$

Applying the same equation to the second surface yields

$$\frac{n_L}{d_1' + d_L} + \frac{n_1}{d_2} = \frac{n_1 - n_L}{R_2} \quad . \tag{2.19}$$

[1] A typical lens, $f = 50\,\text{mm}$ and $\emptyset = 1$ " currently is about 10 times cheaper with spherical surfaces than with optimized aspherical surfaces. See `https://www.thorlabs.com/navigation.cfm?guide_id=2087`

Adding (2.18) and (2.19), we arrive at

$$\frac{n_1}{d_1} + \frac{n_1}{d_2} = (n_L - n_1)\left(\frac{1}{R_1} - \frac{1}{R_2}\right) + \frac{n_L d_L}{(d_1' - d_L)\, d_1'} \quad . \tag{2.20}$$

Now for $d_L \to 0$ we arrive at the *thin-lens equation*:

$$\frac{1}{d_1} + \frac{1}{d_2} = \frac{n_L - n_1}{n_1}\left(\frac{1}{R_1} - \frac{1}{R_2}\right) \tag{2.21}$$

From here it is obvious that the object and image focal lengths,

$$\lim_{d_1 \to \infty} d_2 = f_i = f_o = \lim_{d_2 \to \infty} d_1 \tag{2.22}$$

are the same, so we can drop the subscripts and get the *Lensmaker's formula*:

$$\frac{1}{f} = \frac{n_L - n_1}{n_1}\left(\frac{1}{R_1} - \frac{1}{R_2}\right) \tag{2.23}$$

This formula can in most cases be simplified further by setting $n_1 = 1$ when the lens is operated in air or vacuum. Now, looking back to (2.21) we also get

$$\frac{1}{f} = \frac{1}{d_1} + \frac{1}{d_2} \quad , \tag{2.24}$$

which is the *Gaussian lens formula.*

2.2.3. Image Formation and Optical Systems

Now that we have established the basic laws associated with geometrical optics in the previous chapter, we can advance to the process of image formation. Let us consider an object O that extends perpendicular to the optical axis in front of a thin lens. With a purely geometrical argument, we can determine the position of the image created by the lens. From the paraxial approximation we know that all rays coming from the same source point in a paraxial cone, will arrive at the same image point. Thus, it is sufficient to construct two rays and find their intersection: The first ray travels parallel to the optical axis. From the previous chapter we know that this ray will intercept the image side focal point F_i after the lens. The second ray intersects the object side focal point F_o and will therefore be parallel to the

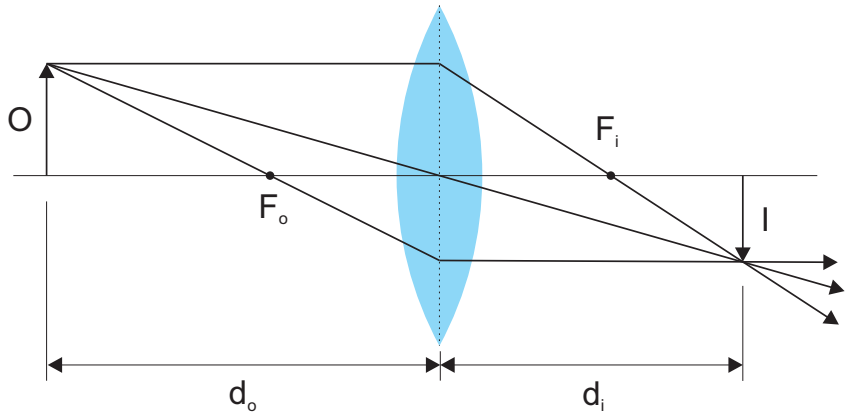

Figure 2.7.: Image formation with a thin lens. For an object O that is distance D_o in front of a thin lens, the image is found by constructing at least two rays and finding their intersection after the lens. The image I is finally formed at a distance d_i.

optical axis. This already gives us the position of the image. As a bonus, we can construct a third ray, commonly termed the chief ray, that goes through the center of the lens. For a thin lens, this ray passes through without disturbance, since the refraction on both surfaces eliminates each other. Note that I have adopted the drawing of the *principal plane* (indicated by the dashed line) above. In essence, we can assume that the refraction only happens at this plane in the lens, since it is sufficiently thin. More precisely, principal planes can be constructed for thick lenses as well. However, they don't always line up with the center of the lens.

In the above case, the image I is real, inverted and demagnified by a factor $M = \frac{d_i}{d_o}$. A *real* image is an image that can be directly viewed on a screen, wheres a *virtual* image requires additional optics to be viewed. Point P' in Figure 2.6 represent a virtual image of point S, that is finally image onto point P by the second spherical surface.

In Table 2.2, the conditions of image formation with thin converging lenses are summarized. In the treatment of lenses, I have been focusing on converging lenses. There are also diverging lenses, that are designed by concave instead of convex surfaces. They can be useful in certain cases, for example to build a *Galilei* beam expander. However, for the optical systems presented in this work, only converging lenses have been used. Therefore, I will exclude diverging lenses from this chapter. In the remaining part of this chapter, I would like to introduce two optical systems

that are important to the deeper understanding of the microscope designed in this work. Here, I will introduce them from the perspective of geometrical optics and will later come back to these devices to expand on their theory.

Table 2.2.: Conditions of image formation using thin converging lenses.

Object Distance d_o	Image Distance d_i	Image Properties
$\infty < d_o < 2f$	$f < d_i < 2f$	real, inverted, demagnified
$d_i = 2f$	$d_o = 2f$	real, inverted, same size
$2f < d_o < f$	$\infty < d_i < 2f$	real, inverted, magnified
$d_o = f$	$d_i = \infty$	no image in finite space
$f < d_i < 0$	$d_i < 0$	virtual, upright, magnified[2]
$d_o = 0$	$d_i = 0$	virtual, upright, same size

The *Keplerian* Telescope

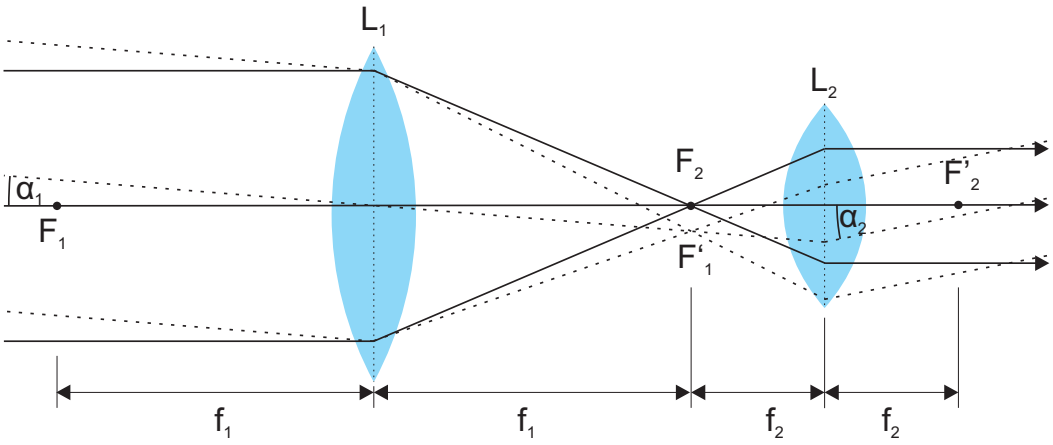

Figure 2.8.: *Keplerian* telescope, also used as beam expander. The system consists of two converging lenses with coinciding focal planes. A parallel beam that enters the system is demagnified in diameter, while its angle is increased.

The first optical system I would like to introduce is the *Keplerian* telescope (Figure 2.8). It is not entirely clear, who first invented this simple, yet powerful and

[2] So far, I have presented optical distances as absolute numbers and omitted the sign convention for clarity. Please note that in this case, a negative distance d_i means that the virtual image is created on the object side of the lens.

versatile arrangement of lenses, though most attribute it to *Kepler* who introduced it in 1611. Also termed astronomical telescope, it was then primarily used to observe stars and other celestial bodies.

The system consists of two converging lenses separated by a distance equal to the sum of their focal lengths. A parallel beam of light, that is parallel to the optical axis, will be focused on the focal point $F_1' = F_2$. After that, the cone of light diverges again and fills the second lens. From the second lens, the light again emerges as parallel beam of light. The diameter of the beam of light is compressed by a factor of

$$M = \frac{f_2}{f_1} \ . \tag{2.25}$$

Here, M is called the magnifying power. (2.25) directly follows from the intercept theorem between the two lenses. In the arrangement in Figure 2.8, M is less than 1. However, by reversing the arrangement, one can easily build a beam expander as well.

When using the arrangement to observe objects at a distance (e.g. stars), we have to consider parallel rays that enter the device at an angle α_1 (dashed lines in Figure 2.8). Theses rays will be focused in the mutual focal plane of both lenses, but slightly off the optical axis. The rays will then leave the device in parallel, but at an angle α_2, that is increased by a factor

$$M_{\text{ang}} = \frac{f_1}{f_2} = \frac{\alpha_2}{\alpha_1} \ . \tag{2.26}$$

M_{ang} is called the angular magnification. This follows by observing the central ray in paraxial approximation, where $\tan\alpha \approx \alpha$.

If one would look through this telescope, one would place the second lens in front of one's eye. The objects would still appear at infinity, allowing the eye to relax, while the angular magnification would let them appear further apart, allowing us to discern fainter objects.

The above system also has very interesting properties when handled in *Fourier optics* theory (cf. chapter 2.3) and is in this context also called 4f-system.

The Infinity-Corrected Microscope

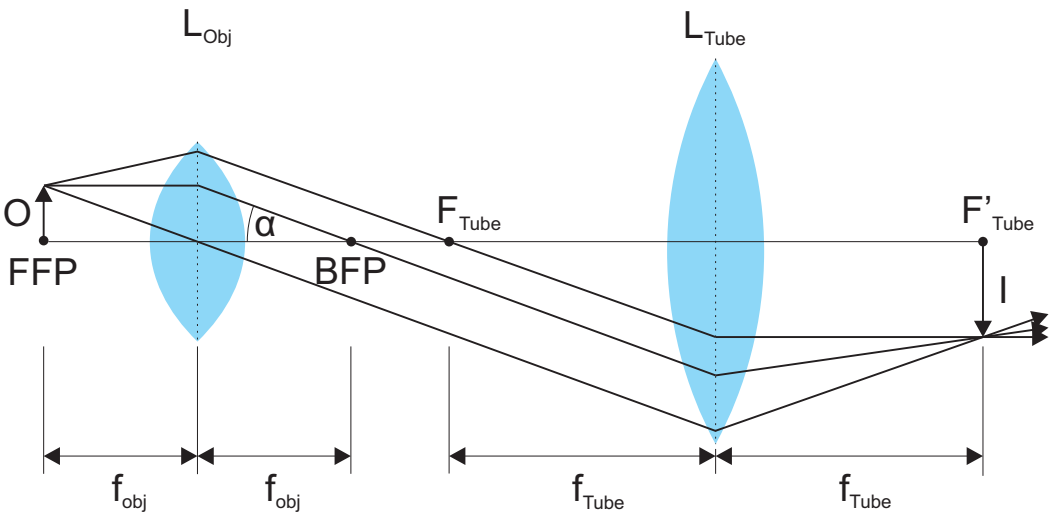

Figure 2.9.: Infinity-corrected compound microscope. An object O is placed in the front focal plane (FFP) of the objective lens L_{obj}. The objective then produces an image at infinity, given raise to parallel light emerging from it at an angle α. The parallel rays are then focused into the focal plane of the tube lens L_{Tube} to produce an image at finite distance. The space between the two lenses is called "infinity space".

Nowadays, the infinity-corrected microscope is the most abundant type of microscopes. Previously, there have also been designs with a fixed image plane of the objective lens. However, the infinity-corrected microscope has some advantages, that I will outline in the following.

The optical schematic is depicted in Figure 2.9. The object O is placed at the focal plane of the first lens, called objective lens L_{obj}. This focal plane is called the front focal plane (FFP), whereas the focal plane of the objective facing away from the object is named the back focal plane (BFP). Light emerging from the object will leave the objective lens as a parallel beam at angle α to the optical axis. Finally, the parallel beam of light will be focused by the tube lens L_{Tube} into its focal plane. The total magnification of the system depends on the ratio of the focal lengths of the two lenses.

$$M = \frac{f_{\text{Tube}}}{f_{\text{Obj}}} \tag{2.27}$$

The space between the two lenses is called the "infinity space", since the rays are parallel there.

The image I at the focal plane of the tube lens can be viewed with an eyepiece. For digital microscopy, a camera sensor is placed at F'_{Tube} to capture the magnified image.

The infinity-corrected design has some advantages for modern microscopy. Since they rays are parallel in the infinity space, the distance between objective and tube lens can be varied within certain boundaries. This makes it possible to introduce additional optical elements into the beam path, such as dichroic mirrors, fluorescent filters or even phase masks. Furthermore, placing these elements in infinity spaces reduces aberrations, since individual rays will encounter them at small angles.

2.2.4. Primary Aberrations

In the previous chapters, I used the idealized Gaussian optics to gain simplicity at the cost of restricting applicability to a small, paraxial region around the optical axis. The paraxial treatment was based on the assumption, that the trigonometric functions involved in the equations can be truncated after the first order term. To understand the implications of this approximations, we assume a rotationally symmetric system and analyze the optical path length between to points on the optical axis. The optical path length given by the paraxial approximation is OLP_0, whereas the optical path length including higher order terms is $\text{OPL}(u, w)$. Here, u and w are generalized coordinates for aperture and field of an optical system, respectively. The difference in optical path length and therefore the wavefront error can be calculated as [HM17]:

$$\begin{aligned}\text{OPL}(u,w) - \text{OPL}_0 =& a_1 u^2 + a_2 wu\cos\varphi \\ &+ b_1 u^4 + b_2 wu^3 + b_3 w^2 u^2 \cos^2\varphi + b_4 w^2 u^2 + b_5 w^3 u\cos\varphi \\ &+ \mathcal{O}((wu)^5)\end{aligned}$$

Here, φ is the angle of a specific ray to the optical axis when entering the system. The first two terms, lead by a_i, describe a shift in focus and can be eliminated by choosing an appropriate reference point. The remaining terms describe the *aberations* in an optical system, that is they describe the deviations from the assumption

of the paraxial approximation. Of special importance are the terms in the second row, all of fourth order in uw. Those describe the five *primary aberrations*. They have first been described mathematically by *Seidel* in the 1850s and are thus also called *Seidel aberrations*.

I have already shown, that spherical surfaces only create a perfect image in the paraxial approximation. Nevertheless, spherical lenses are used in most optical devices. Thus, primary aberrations occur regularly and must be corrected to obtain adequate image quality. In the following, I will briefly show the five primary monochromatic aberrations phenomenologically and give hints as how to avoid them (Figure 2.10). I will also briefly show how chromatic aberrations can effect system performance. While doing so, I will pretend each aberration appears independently without the others. Of course, this is usually not the case for a real system.

Spherical Aberrations ($\sim u^4$)

Spherical aberrations occur when the distance of a ray to the optical axis is not neglectable as it impinges on a spherical surface. If one thinks back to (2.12), I set $s_i \approx d_i$, which neglects the height of the ray above the optical axis. It turns out that the focal length of a lens depends on this height. Specifically, the further away a ray is from the optical axis, the shorter is the focal length for this ray. The envelope around the focus, with the paraxial focal point at its tip, is called caustic.

Since high-resolution microscopy relies on high numerical apertures, spherical aberrations are the most important aberrations. They can be reduced by either limiting the aperture of the lens (which would mean loss of light and signal), by using lens doublets, or by lenses with aspherical surfaces. It also helps to distribute the refraction evenly among the two surfaces of a lens. The side of a lens with the lesser radius of curvature is then facing the collimated beam.

Spherical aberration is also the primary aberration when the refractive index mismatch at the glass-surface of a typical microscope is not accounted for and leads to significant signal deterioration.

Coma ($\sim u^3 w$)

Comatic aberrations are introduced into the system, if an object point is not on the optical axis and the system has a big aperture. They originate from the fact

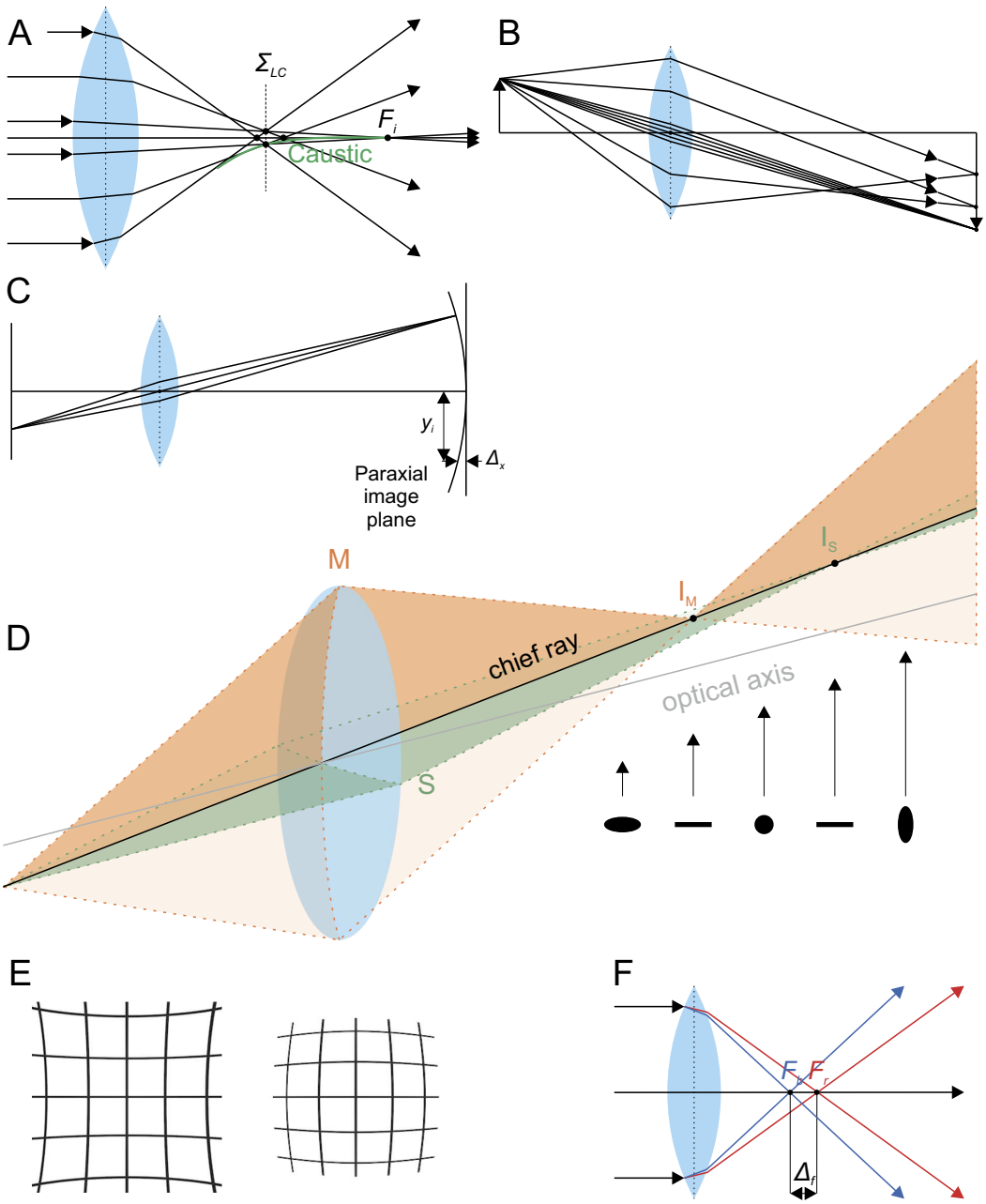

Figure 2.10.: Primary monochromatic aberrations and chromatic aberration. (A) Spherical aberration with the circle of least confusion Σ_{LC} and the paraxial focus F_i. (B) Coma. (C) Field curvature with distance Δ_x at height y above the optical axis. (D) Astigmatism, with image points I_M and I_S for the meridional (M) and sagittal (S) rays, with the PSF at different distances depicted in black. (E) Pincushion (left) and barrel (right) distortion of the image plane. (F) Chromatic aberration with different focal lengths F_b, F_r depending on the wavelength of light.

that we introduced principal planes in the paraxial approximation, at which the refraction is happening. In reality, if one still wants to have principal surfaces to facilitate ray tracing, the principal surface is more of a curved surface. This leads to different magnifications of the image, depending on the height of a specific ray at the lens. Phenomenologically, an off-axis point is imaged as a cone, with the paraxial image point at the tip and an opening angle of 60°.

It is important to note that coma depends on the specific type of lens and, as with spherical aberrations, on its orientation. Furthermore, coma can be entirely eliminated by placing a stop at the correct location within a system.

Astigmatism ($\sim u^2w^2$)

Astigmatism means "not point-like" and occurs for object points that are an appreciable distance away from the optical axis. For considering this type of aberration, we have to define two planes in the optical system. The *meridional plane* contains the optical axis and the chief ray. The *sagittal plane* contains the chief ray and is otherwise perpendicular to the meridional plane. It is noteworthy, that for an object point on the optical axis, the two planes are not distinguishable and therefore astigmatism does not occur.

The rays in the meridional plane are refracted stronger than those in the sagittal plane. This leads to two different focal lengths with respect to these planes. When the meridional rays are focused, the sagittal rays are still spread, resulting in a vertical line on a screen. At the point where the sagittal rays come to a focus, the meridional rays are already diverging again, resulting in a vertical line on a screen. Those two points are shifted by the *astigmatic shift*. Between those two points, there is the *circle of least confusion*, where the rays in both planes are equally close to their focus and the object appears point-like.

Astigmatism can be reduced or eliminated by the choice of lens type, the placement of apertures and by combining several lenses. We will see in chapter 2.4.2, that astigmatism does not have to be a disadvantage, but can rather be used to decode the third dimension in 3D single molecule microscopy.

Field Curvature ($\sim w^2u^2$)

Examining the image formation of extended planar objects leads to the conclusion, that the image "plane" can only be considered flat in the paraxial region, but it is actually a paraboloid otherwise. This aberration was first described mathematically by *Petzval* in the 19$^{\text{th}}$ century and is called *field curvature*. The axial deviation from a flat image plane can be described as

$$\Delta z = \frac{y_i^2}{2} \sum_j \frac{1}{n_j f_j} \quad , \tag{2.28}$$

where j iterates over all thin lenses in the system [Hec17]. This makes it possible to eliminate field curvature, for example by choosing a second lens with the same absolute focal length, but negative sign (i.e. a diverging lens).

Distortion ($\sim uw^3$)

The last of the five primary aberrations is distortion. It originates from the fact that the magnification M can depend on the off-axis image position. This leads to an image that is "stretched", with the optical axis at its center. An outward stretch is called barrel distortion, whereas an inward compression is called pincushion distortion. The effect is best visible when imaging a rectangular array of lines as a test target. Again, this effect can also be diminished by placing a stop at specific locations within the system.

Chromatic Aberrations ($\sim \lambda$)

The five primary aberrations mentioned previously occur for any type of light. However, for polychromatic light with, dispersion effects have to be taken into account. That is, the refractive index of any glass depends on the wavelength of the light that travels through it. Usually, n is a monotonic decreasing function of λ. This instantly makes essential properties such as the focal length of a lens and the magnification of a system dependent on the wavelength. If more than one wavelength is to be used in a system at any one time, one cannot record images in sequence and correct chromatic shifts in-between. Instead, the system itself has to be corrected for a specific wavelength range.

To mitigate chromatic aberrations, it is possible to carefully choose glasses with different dispersive powers and combine them to lens doublets or triplets. However, since the dispersion functions are not linear, a lens can only be corrected for specific, predefined wavelengths. A lens that is corrected for two wavelengths (usually the F and C *Fraunhofer lines*, corresponding to wavelengths of 486 nm and 656 nm) is called *achromat*. If it is corrected for more than two wavelengths (usually the d Fraunhofer line at 588 nm), it is called *apochromat*.

2.3. Fourier Optics

In the previous chapter, we have seen that the foundations of geometrical optics allow us to model many optical systems and draw important conclusions about them. However, when structures in the system are on the order of the wavelength of light, geometrical optics do not suffice anymore to describe an optical system. Then, we have to enter the realm of wave optics, often also called physical optics. Here, we particularly account for the wave nature of light and all of its implications, most importantly interference and diffraction. Since many optical systems are *linear* and *invariant*, *Fourier Analysis* provides convenient tools to describe the system's response. In the following, I will revisit Fourier Analysis in two dimensions in relation to optics. I will then present the scalar diffraction theory for light propagation. Following, I will introduce the angular spectrum representation, a decomposition of the electric field into plane waves that is especially useful. The *Fraunhofer Approximation* lets us then make some simplifications to the propagation integrals for sufficiently great distances. Finally, I will use the theory to calculate the fundamental resolution limit in microscopy, often termed *Diffraction Barrier*.

For most chapters, I will only be able to state the most important facts and equations within the scope of this work. For a more comprehensive introduction to Fourier optics, I recommend the books by *Goodman* [Goo17] and *Novotny* and *B. Hecht* [NH06] and for a more simulation-oriented approach the book by *Schmidt* [Sch10]. The aforementioned book by *E. Hecht* [Hec17] also has a well-written chapter on Fourier optics. These books are the foundation of what is reported here and many calculations go back to [BW93].

2.3.1. Revisiting 2D Fourier Analysis for Optical Systems

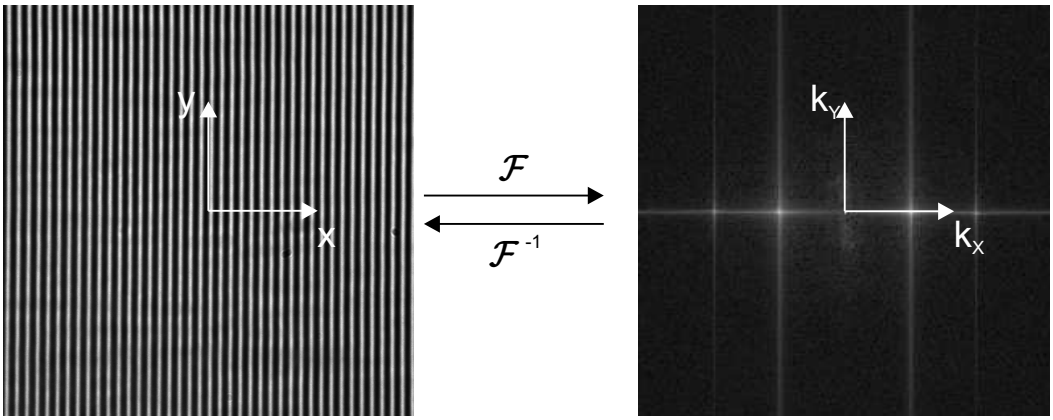

Figure 2.11.: 2D Fourier transform of a microscopic image of a 400 lp /mm Ronchi ruling. (Left) Image of the ruling as acquired by the microscope. (Right) 2D Fourier transform with distinct lines at the spatial frequency of the ruling.

Commonly, the *Fourier transform* (sometimes also referred to as the *Fourier spectrum* or *frequency spectrum*) of a function g of two independent variables x and y is defined by

$$\mathcal{F}\{g\} = \frac{1}{2\pi} \iint_{-\infty}^{\infty} g(x,y)\, e^{-i(k_x x + k_y y)}\, dxdy \quad . \tag{2.29}$$

Here, $g(x,y)$ can in general be complex valued, which in turn leads to a complex valued Fourier transform $\mathcal{F}$ that depends on two independent variables k_x and k_y. We call these variables *spatial frequencies*. The *inverse Fourier transform* of a function $G(k_x, k_y)$ is then defined as

$$\mathcal{F}^{-1}\{G\} = \frac{1}{2\pi} \iint_{-\infty}^{\infty} G(k_x,k_y)\, e^{i(k_x x + k_y y)}\, dk_x dk_y \quad . \tag{2.30}$$

Of course, these integrals may not exist for certain functions. However, as *Bracewell* wrote [Bra00], "physical possibility is a valid sufficient condition for the existence of a transform."

One way to think of a Fourier transform is as a decomposition into a linear

combination of elementary oscillating functions. In the inverse transform, $G(k_x, k_y)$ can be thought of as individual weighting factors for spatial frequencies (k_x, k_y) in order to synthesize the desired function $g(x, y)$. In the integral, $e^{i(k_x x + k_y y)}$ represents a plane wave in (x, y) space traveling at an angle $\varphi = \tan^{-1}\left({}^{k_y}/_{k_x}\right)$ with respect to the x axis and at a wavelength of $\lambda = \left(2\pi\sqrt{k_x^2 + k_y^2}\right)^{-1}$.

As an example, Figure 2.11 shows a *Ronchi* ruling with 400 lp /mm, imaged on a microscope on the left. The calculated Fourier transform of the intensity values is displayed on the right, with the spatial frequency of the ruling clearly visible as vertical lines at certain frequencies k_x. The inverse Fourier transform of the image on the right again results in the image on the left. This offers a quick way to precisely calibrate the pixel size of a microscope.

Before we embark on specific application of Fourier analysis on optical wave propagation, I would like to state some useful theorems from the rich mathematical structure of Fourier analysis. I will display them without proofs, which can be found in [Goo17] for instance.

Fourier integral theorem $\mathcal{F}\mathcal{F}^{-1}\{g(x, y)\} = \mathcal{F}^{-1}\mathcal{F}\{g(x, y)\} = g(x, y)$ at each point of continuity of g. We could already observe an example of this theorem in Figure 2.11.

Linearity theorem $\mathcal{F}\{ag + bh\} = a\mathcal{F}\{g\} + b\mathcal{F}\{h\}$ Fourier transforming a weighted sum of two functions g and h simply gives the weighted sum of their individual transforms.

Similarity theorem Let $\mathcal{F}\{g(x, y)\} = G(k_x, k_y)$, then $\mathcal{F}\{g(ax, by)\}$ $= \frac{1}{|ab|} G\left(\frac{k_x}{a}, \frac{k_y}{b}\right)$. In essence, this means that a stretch of coordinates in the space domain results in a shrinking of coordinates in the frequency domain, plus a normalization of the amplitude.

Shift theorem Let $\mathcal{F}\{g(x, y)\} = G(k_x, k_y)$, then $\mathcal{F}\{g(x - a, y - b)\}$ $= G(k_x, k_y)\, e^{-i(ak_x + bk_y)}$. A shift in space domain introduces a linear face shift in the frequency domain.

Convolution theorem Let $\mathcal{F}\{g(x, y)\} = G(k_x, k_y)$ and $\mathcal{F}\{h(x, y)\} = H(k_x, k_y)$. Then $\mathcal{F}\left\{\iint_{-\infty}^{+\infty} g(\eta, \vartheta)\, h(x - \eta, y - \vartheta)\, d\eta d\vartheta\right\} = G(k_x, k_y)\, H(k_x, k_y)$. Here, the integral represents a convolution of two functions g and h. Convolving

these two functions is equivalent to multiplying their Fourier transforms and then taking the inverse Fourier transform. This theorem is particularly useful in many computational problems, since multiplying and Fourier transforms are very fast compared to integrating over the whole real space.

2.3.2. Linear Systems

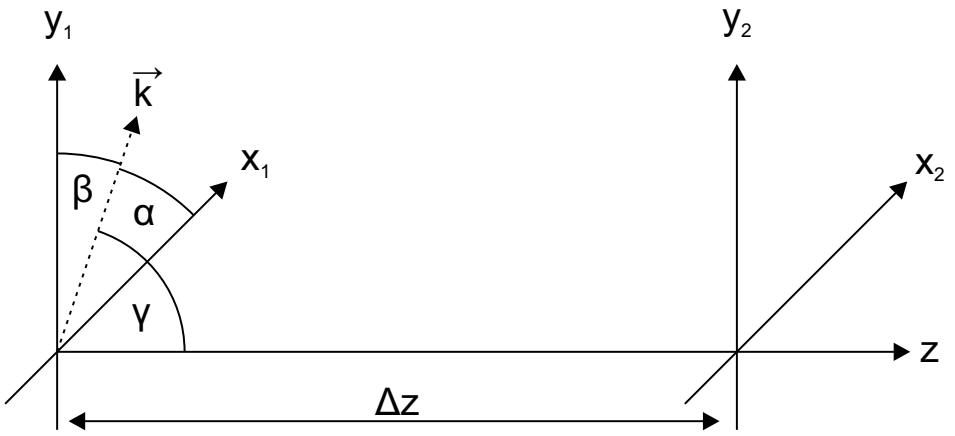

Figure 2.12.: Definition of coordinates for optical systems. The input plane (x_1, y_1) and the output plane (x_2, y_2) are parallel and offset by a distance Δz. A wave traveling in direction $\vec{k}$ has angles α, β, γ with the x, y, z axis, respectively.

In this chapter I would like to take a moment and define a *Linear Optical System* as well as the coordinate system for optical wave propagation. In signal processing theory, a system depicted by an operator $\mathcal{L}\{\}$ that acts on a time-dependent function (i.e. electrical voltage) $f(t)$:

$$f_2(t_2) = \mathcal{L}_{1D}\{f_1(t_1)\} \tag{2.31}$$

is said to be linear, if

$$a\,\mathcal{L}_{1D}\{f(t)\} + b\,\mathcal{L}_{1D}\{g(t)\} = \mathcal{L}_{1D}\{af(t) + bg(t)\} \tag{2.32}$$

for all input functions f, g and complex constants a, b. In an optical system, one usually observes the change of a function by a system from the input plane to the

parallel output plane (Figure 2.12). The function of interest is here the electrical field in these planes, so f, g are in our case complex-valued functions of two coordinates x, y. An optical system is said to be linear, if

$$a\,\mathcal{L}_{2D}\left\{f\left(x,y\right)\right\} + b\,\mathcal{L}_{2D}\left\{g\left(x,y\right)\right\} = \mathcal{L}_{2D}\left\{af\left(x,y\right) + bg\left(x,y\right)\right\} \quad . \tag{2.33}$$

The great advantage of a linear system is that its output can be expressed as a sum of its responses to infinitesimal small point sources. This response is called the *point-spread function* (PSF) h:

$$h\left(x_1,y_1;x_2,y_2\right) = \mathcal{L}_{2D}\left\{\delta\left(x_2-x_1,y_2-y_1\right)\right\} \tag{2.34}$$

Here, δ is the *Dirac* delta function

$$\delta\left(x\right) = \begin{cases} \infty, & x = 0 \\ 0, & x \neq 0 \end{cases} \tag{2.35}$$

and the multi-variable delta function is defined as a product thereof:

$$\delta\left(x,y\right) = \delta(x)\delta(y) \tag{2.36}$$

In essence, (2.34) evaluates the system operator output at position (x_2, y_2) in the output plane for an input at position (x_1, y_1) in the input plane. Now, the system output g_2 can be calculated from the input g_1 using the PSF:

$$g_2(x_2,y_2) = \iint_{-\infty}^{\infty} g_1(x_1,y_1)h(x_1,y_1;x_2,y_2)\;dx_1dy_1 \tag{2.37}$$

A linear system is therefore completely characterized by its PSF. That it why a great deal of time is spent optimizing it as an experimentalist and analyzing it as a theorist.

If the PSF of an optical system only depends on the distances between the input point and the output point, $(x_2 - x_1)$ and $(y_2 - y_1)$, the system is called *spatially*

invariant. Equation (2.37) then becomes

$$g_2(x_2, y_2) = \iint_{-\infty}^{\infty} g_1(x_1, y_1) h(x_1 - x_2, y_2 - y_1)\, dx_1 dy_1 \tag{2.38}$$

which can be immediately recognized as 2-dimensional convolution of the input field g_1 with the PSF h. We notice that if

$$g_2 = g_1 \star h \ , \tag{2.39}$$

where $\star$ denotes the convolution operator, then the convolution theorem tells us that

$$G_2(k_x, k_y) = G_1(k_x, k_y) H(k_x, k_y) \ , \tag{2.40}$$

where G_1, G_2, H are the Fourier transforms of g_1, g_2, h. As already highlighted, the path of calculating G_2 with the convolution theorem and then doing an inverse transform to get g_2 is often much faster carried out. That is why H is of equal importance as h and is also called the *Optical Transfer Function* (OTF).

One can interpret the PSF as a function that tells us how a point source is imaged onto a target plane, while the OTF tells us to what extend certain spatial frequencies are transmitted by the system.

2.3.3. Scalar Diffraction Theory

Starting from the most rigorous macroscopic treatment of light and its propagation, namely the *Maxwell Equations*, we know that light is an electromagnetic wave with coupled electric and magnetic field that travels through space. Far-field optics usually deals with optical wave propagation through linear, isotropic and homogeneous media in the absence of free charge and currents, such as air or the glass of a lens with constant refractive index. Here, the electric field $\vec{E}$ and the magnetic field $\vec{B}$ of a monochromatic wave form a triad with the propagation direction. Furthermore, each of their vectorial components must satisfy the time-independent *Helmholtz Equation*:

$$\left(\Delta + k^2\right) U\left(\vec{r}\right) = 0 \tag{2.41}$$

Here, $\Delta = \nabla^2 = \frac{\partial^2}{\partial x^2} + \frac{\partial^2}{\partial y^2} + \frac{\partial^2}{\partial z^2}$ is the *Laplacian Operator* and $k = \frac{2\pi n\nu}{c} = \frac{2\pi}{\lambda}$ with $\lambda = \frac{c}{n\nu}$ being the wavelength in medium. In summary, with the above conditions to the medium of propagation, we can go from a full vectorial treatment of the Maxwell Equations to much easier scalar treatment of the individual independent vector components.

In the context of this work, there are several interesting simple solutions to the time-independent Helmholtz Equation. These are the planar, spherical and Gaussian-beam waves. I will briefly introduce them in the following. To get the time-dependent solution, one can immediately multiply with $e^{-i\omega t}$.

A planar wave originating at $\vec{r}_0$ can be described by

$$U_P(\vec{r}) = Ae^{i\vec{k}(\vec{r}-\vec{r}_0)} \ , \tag{2.42}$$

where A is the amplitude and $\vec{k}$ is the wave vector pointing in the direction of propagation. For a spherical wave we similarly get

$$U_S(\vec{r}) = \frac{A}{R(\vec{r}-\vec{r}_0)} e^{i\vec{k}R(\vec{r}-\vec{r}_0)} \tag{2.43}$$

where $R(\vec{r}-\vec{r}_0) = |\vec{r}-\vec{r}_0|$ is the wavefront radius of curvature. The last wave I would like to present is the Gaussian beam. It is quite important in laser optics and fluorescence microscopy, since it resembles the TEM_{00} output of a laser. It has a Gaussian amplitude profile and a spherical wavefront, that is approximated by the paraxial approximation:

$$U_G(\vec{r}) = \frac{A}{q(z)} \exp\left(ik\frac{x^2+y^2}{2q(z)}\right) \tag{2.44}$$

With

$$\frac{1}{q} = \frac{1}{R(z)} + \frac{i\lambda}{\pi w^2(z)} \tag{2.45}$$

$$w^2(z) = w_0^2\left[1 + \left(\frac{\lambda z}{\pi w_0^2}\right)^2\right] \tag{2.46}$$

$$R(z) = z\left[1 + \left(\frac{\pi w_0^2}{\lambda z}\right)^2\right] \ . \tag{2.47}$$

Here, $q(z)$ is called the complex beam parameter and $w(z)$ signifies the $1/e$ beam radius at position z with $w(0) = w_0$. I will expand on the properties of Gaussian beams in chapter 2.5.1, where I will discuss its applicability to light-sheets.

2.3.4. Angular Spectrum Representation

In most cases, the optical source is not just a simple planar or spherical wave. Instead, we want to be able to calculate the resulting field in an observation plane $U_O(x, y)$ depending on the known field in the source plane $U_S(x, y)$. The planes are parallel and separated by a distance Δz (cf. Figure 2.12). Suppose the function U_S has the Fourier transform A at $z = 0$:

$$A(k_x, k_y, 0) = \frac{1}{2\pi} \iint_{-\infty}^{\infty} U_S(x, y, 0)\, e^{-i(xk_x + yk_y)}\, dxdy \tag{2.48}$$

Then, according to chapter 2.3.1, we can write U_S as the inverse transform of its spectrum:

$$U_S(x, y, 0) = \frac{1}{2\pi} \iint_{-\infty}^{\infty} A(k_x, k_y, 0)\, e^{i(k_x x + k_y y)}\, dk_x dk_y \tag{2.49}$$

Similarly, the Fourier transform of the field in the observation plane reads

$$A(k_x, k_y, z) = \frac{1}{2\pi} \iint_{-\infty}^{\infty} U_O(x, y, z)\, e^{-i(xk_x + yk_y)}\, dxdy \quad . \tag{2.50}$$

Substituting this into the Helmholtz equation (2.41) and defining

$$k_z = \sqrt{k^2 - k_x^2 - k_y^2} \tag{2.51}$$

we get

$$A(k_x, k_y, z) = A(k_x, k_y, 0)\, e^{\pm i k_z z} \quad . \tag{2.52}$$

This means that the *angular spectrum* in the observation plane can be found by propagating the angular spectrum of the source plane along z:

$$U(x,y,z) = \frac{1}{2\pi} \iint_{-\infty}^{\infty} A(x,y,0)\, e^{\pm ik_z z} e^{i(k_x x + k_y y)}\, dk_x dk_y \tag{2.53}$$

The factor $\exp(ik_z z)$ is also called the propagator in reciprocal space. The $\pm$ sign indicates that we have to superimpose the two available solutions propagating in positive and negative z direction. Now thinking back to chapter 2.3.2, we can also identify it as the transfer function of optical wave propagation:

$$H(k_x, k_y) = \exp\left[\pm iz\sqrt{k^2 - k_x^2 - k_y^2}\right] \tag{2.54}$$

In equation (2.51) we notice that for $k_x^2 + k_y^2 > k^2$, k_z becomes complex. This situation corresponds to *evanescent waves*, that are damped exponentially. One application of this effect is the illumination of thin sections of a sample in total internal reflection (TIRF) microscopy (cf. chapter 2.5). Another one is near-field microscopy, which takes advantage of the higher spatial frequencies contained in the evanescent field. However, within the scope of this work, far-field applications are considered, so we can disregard the evanescent case. For the far-field case, the propagator acts like a linear spatial filter with cutoff frequency $k_x^2 + k_y^2 < k^2$.

2.3.5. Paraxial Approximation and Fourier Transformation Property of Lenses

Integrating the Fourier integrals presented in the previous chapter is not an easy problem since analytical solutions only exist for a handful of input fields. So making certain approximations for specific applications comes to mind. Similar to the treatment on geometrical optics (cf. chapter 2.2), we can apply approximations to the angular spectrum representation in the paraxial case, for which we can expand

$$k_z = k\sqrt{1 - \frac{\left(k_x^2 - k_y^2\right)}{k^2}} \approx k - \frac{k_x^2 + k_y^2}{2k} \tag{2.55}$$

by a Taylor series. In particular, this approximation is accurate for waves that travel at an angle γ to the z axis and

$$\frac{\gamma^4 \Delta z}{4\lambda} \ll 1 \ . \tag{2.56}$$

Going back to real space, we can express $U(x, y, z)$ as a convolution using the convolution theorem:

$$U\left(x, y, z\right) = U(x_0, y_0, 0) \star h_z\left(x - x_0, y - y_0\right) \tag{2.57}$$

Where h_z is the Fourier transform of $H\left(k_x, k_y\right)$ in the paraxial case[3]:

$$\begin{aligned} h_z\left(x, y\right) &= \mathcal{F}\left\{H\left(k_x, k_y\right)\right\} = \mathcal{F}\left\{\exp\left[iz\left(k - \frac{k_x^2 + k_y^2}{2k}\right)\right]\right\} \\ &= e^{ikz}\mathcal{F}\left\{\exp\left[-iz\frac{k_x^2 + k_y^2}{2k}\right]\right\} = \frac{k}{2z\pi i}e^{ikz}e^{\frac{ik}{2z}\left(x^2+y^2\right)} \end{aligned}$$

With this convolution, we effectively arrive at the *Fresnel diffraction integral*

$$U\left(x, y, z\right) = \frac{ke^{ikz}}{2z\pi i}\iint_{-\infty}^{\infty} U(x_0, y_0, 0)\exp\left[i\frac{k}{2z}\left(\left(x - x_0\right)^2 + \left(y - y_0\right)^2\right)\right] dx_0 dy_0 \tag{2.58}$$

that can also be expressed as a Fourier transform by pulling out the quadratic phase factor $\exp\left[\frac{ik}{2z}\left(x^2 + y^2\right)\right]$ from the integral:

$$U\left(x, y, z\right) = \frac{ke^{ikz}}{2z\pi i}e^{i\frac{k}{2z}\left(x^2+y^2\right)}\iint_{-\infty}^{\infty} U\left(x_0, y_0, 0\right)\ e^{i\frac{k}{2z}\left(x_0^2+y_0^2\right)}\, e^{-i\frac{k}{z}\left(x_0 x + y_0 y\right)}\ dx_0 dy_0 \tag{2.59}$$

We can appreciate that in the paraxial case, the propagation between two planes manifests as a spherical wave propagating along z, where the phase and amplitude is governed by the integral. The integral can be recognized as a Fourier transform

[3] Using the identity $\mathcal{F}\left\{\exp\left[-i\pi\left(\frac{k_x^2}{a^2} + \frac{k_y^2}{b^2}\right)\right]\right\} = \frac{|ab|}{i}\exp\left[i\pi\left(a^2x^2 + b^2y^2\right)\right]$ found in [Goo17]

of the source plane field multiplied by a *quadratic phase factor.*

For a thin lens with focal length f, it can be shown that the phase shift applied to a plane wave impinging at coordinates (x,y) on the lens is

$$t_L(x,y) = \exp\left[-i\frac{k}{2f}\left(x^2+y^2\right)\right] \tag{2.60}$$

in paraxial approximation.

Let us now investigate the case where we put a known optical field U_S (an object) at a distance d to a lens and observe the field at the focal plane on the other side of the lens. For the purpose of this examination, let's imagine a transparent slide, illuminated by a homogeneous plane wave as our object. First, the field will propagate in free space for a distance d until it arrives at the lens. Using equation (2.52) we get

$$A_L(k_x,k_y) = A_S(k_x,k_y)\exp\left[-i\frac{d}{2k}\left(k_x^2+k_y^2\right)\right] \tag{2.61}$$

for the angular spectrum at the lens, where I have dropped the constant phase delay from equation (2.55), because we are ultimately interested in the intensity distribution. Now for the field U_L impinging on the lens, the field right after the lens will be

$$U_L'(x,y) = U_L(x,y)\; t_L(x,y) \quad . \tag{2.62}$$

Propagating to the BFP after the lens at $z = f$ using equation (2.59) yields

$$U_{\mathrm{BFP}}(u,v) = \frac{k}{2f\pi i}e^{i\frac{k}{2f}\left(u^2+v^2\right)}\iint_{-\infty}^{\infty} U_L'(x,y,0)\; e^{i\frac{k}{2f}\left(x^2+y^2\right)}\, e^{-i\frac{k}{f}(xu+yv)}\; dx_0 dy_0 \tag{2.63}$$

again without the preceding constant phase shift. Now substituting U_L' from equation (2.62), the quadratic phase term cancels out quite nicely and we are left with a simple Fourier transform with coordinates scaled by k/f that is preceded by a

quadratic phase factor:

$$\begin{aligned} U_{\mathrm{BFP}}(u,v) &= \frac{k}{2f\pi i} e^{i\frac{k}{2f}(u^2+v^2)} \iint_{-\infty}^{\infty} U_L(x,y,0)\; e^{-i\frac{k}{f}(xu+yv)}\; dxdy \\ &= \frac{k}{fi} e^{i\frac{k}{2f}(u^2+v^2)} A_L\left(\frac{ku}{f}, \frac{kv}{f}\right) \\ &\overset{(2.61)}{=} \frac{k \exp\left[i\frac{k}{2f}\left(1-\frac{d}{f}\right)(u^2+v^2)\right]}{if} A_S\left(\frac{ku}{f}, \frac{kv}{f}\right) \end{aligned}$$

This equation is quite remarkable, since it relates the field in the focal plane of a lens directly to the *Fourier transform* of the input field. If the input is placed against the lens with $d = 0$, we get the *Fraunhofer diffraction pattern* at the BFP. Usually, one measures the intensity of the pattern on a detector, which would amount to

$$I(u,v) = |U_{\mathrm{BFP}}|^2 = \frac{A^2k^2}{f^2}\left|A_S\left(\frac{ku}{f}, \frac{kv}{f}\right)\right|^2 \quad . \tag{2.64}$$

If the input is placed in the front focal plane of the lens with $d = f$, the quadratic phase factor vanishes and we are even left with a perfect Fourier transform of the optical field.

The Fourier transforming property of lenses has many applications. A simple one would be a 4f-system (cf. chapter 2.2.3), where two lenses are arranged such that their focal planes coincide. In the shared focal plane, the Fourier transform of the input (placed in the FFP of the first lens) appears and can be manipulated, while the result is then visible in the BFP of the second lens.

2.3.6. The Diffraction Barrier in Microscopy

Suppose we have a microscope that is diffraction-limited, meaning that all occurring aberrations in the system are of lesser magnitude than the diffraction happening in the system. In this case, the far-field image of a point source is of the form

$$I(r) = I_0\left(\frac{2J_1(\pi r)}{\pi r}\right)^2 \quad . \tag{2.65}$$

Here, J_1 is the *Bessel function* of first kind and first order and r the radial coordinate in the image plane. The resulting image is called *Airy disk* and is displayed in Fig-

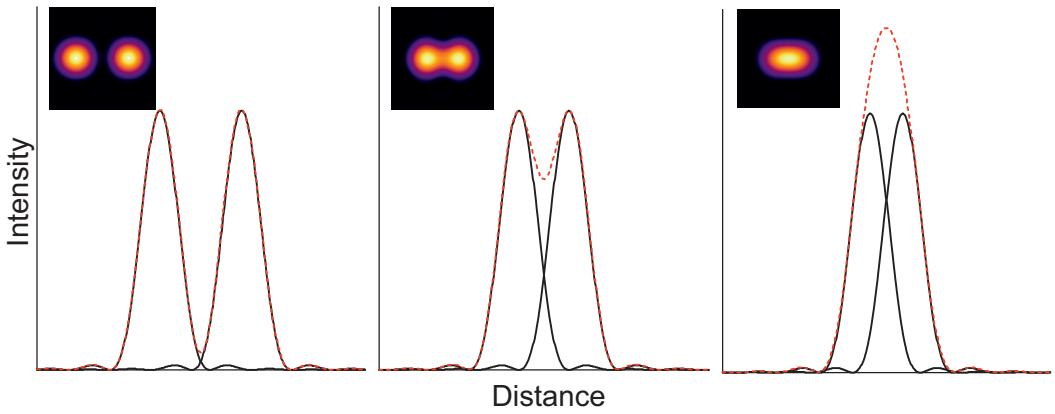

Figure 2.13.: Simulated diffraction-limited image of two point sources at different distances. Shown are the cross-sections of the intensity of the individual Airy disks (black lines), the resulting superimposed intensity (red dashed line) and the resulting 2D image (inset). (Left) At $d > d_{\text{Rayleigh}}$ the two spots are clearly resolvable. (Center) At $d = d_{\text{Rayleigh}}$ are just barely resolvable and at $d < d_{\text{Rayleigh}}$ the two sources are not resolvable (right).

ure 2.13 for two point sources at different distances to each other. In 1896, *Rayleigh* deduced a criterion, upon which two point emitters can be resolved in the far-field image [Ray96]. For fluorescence microscopy, we can consider the non-coherent case of emission, where the intensity of the two point sources is superimposed in the image plane. Hence, two point emitters are said to be resolvable, when the maximum of one Airy disk coincides with the first minimum of the other Airy disk (center panel). The distance between the emitters is then

$$d_{\text{Rayleigh}} = \frac{0.61\lambda}{\text{NA}} \quad . \tag{2.66}$$

This minimum distance is called the *Rayleigh criterion*. Here, $\text{NA} = n \sin\alpha$ is the *numerical aperture* of the microscope objective, with n being the refractive index between the objective and the sample and α being the opening angle of the objective. If the two point sources are closer than d_{Rayleigh}, there is no way to tell the underlying structure in the object plane.

From the Rayleigh criterion we can immediately appreciate, that the lateral resolution of a conventional microscope that uses visible light tops out at $\approx 200\,\text{nm}$, if we use UV light at around 400 nm and consider the refractive index of glass is

≈ 1.5 [HM17]. This resolution was experimentally reached decades ago for optical wavelengths and was since termed *Diffraction Limit* while today it is more often called *Diffraction Barrier*, because it can be "broken" with new techniques as we will see in the following.

2.4. Breaking the Diffraction Barrier – Super-Resolution Microscopy

The last two decades have seen the advent of various super-resolution techniques that are able to produce resolutions beyond the diffraction limit. Initially driven by the advance of technology, many have become a valuable tool for biological and medical questions and are commercially available. Ultimately, the Nobel Prize in chemistry 2014 was dedicated to *Betzig*, *Hell* and *Moerner* for their major contributions to the field of super-resolution fluorescence microscopy [Nob19]. The current super-resolution techniques can be divided into four categories, which I will explain in the following. A sound and very recent review of all these techniques and their connection to diffraction-limited approaches can be found in [Sch+19] and a broad overview in [Bir17].

The first and most recent technique is *Expansion Microscopy* [CTB15; Cha+17]. Although not an optical method, it still allows for imaging structures well beyond the diffraction limit with fluorescence microscopy. In short, the biological structure of interest is labeled with fluorescent dyes that are linked into a hydrogel at the same time. After digesting the biological structure enzymatically, the gel only contains the dye molecules at positions representing the structure. Now, the gel can be expanded isotropically by a factor of 4x to 20x, by adding water to it and wait for it to swell. Subsequently, it can be imaged on a conventional microscope. Of course, expanding the sample can also be combined with optical super-resolution techniques to gain even higher resolution [Gam+19]. Ultimately, the resolution achievable is limited by the linker length between target structure and dye molecule and the isotropic expansion of the gel. Naturally, this approach is not compatible to imaging living specimen.

The second technique I would like to mention is *Stimulated Emission Depletion* (STED) microscopy [HW94; Kla+00]. This approach is based on a confocal laser-

scanning microscope (LSM). After a focused excitation pulse, the excited focal region is immediately illuminated with a second red-shifted, donut-shaped light pulse. This facilitates stimulated emission in the outer parts of the excitation PSF, effectively shrinking the volume of fluorescent dyes to sub-diffractive regions. Generally, very high laser powers are needed for this approach, limiting the choice of dyes to very stable ones. As with all confocal imaging methods, acquisition times scale with the imaged area in STED. All in all, a spatial resolution of 30-80 nm can be reached in expert laboratories, whereas commercial setups are limited to 60-120 nm [Sch+19].

The third class of super-resolution imaging techniques is called *Structured Illumination Microscopy* (SIM). In traditional SIM, this involves creating a periodic interference pattern to illuminate the sample, effectively shifting higher-order spatial frequencies into the frequency passband that is accessible by the detection objective [Gus00; HC99]. The interference pattern is shifted and rotated at various angles to fully sample the extended frequency space, while an image is taken at each setting (Figure 2.14a). Shifting the frequencies back to their origin in k space is done in post processing. Another approach is also based on a confocal microscope. Instead of detecting the fluorescence on a single-pixel detector after filtering with a pinhole, the fluorescence is detected on an array detector (e.g. a camera or matrix of photomultiplier tubes). Then, the detected intensity is reassigned according to its known distance from the excitation PSF. This reassignment can be done optically [Luc+13; Yor+13] or computationally [ME10]. The best obtainable resolution is fundamentally limited to half the Rayleigh criterion for linear excitation schemes, yielding 100-130 nm laterally and 300-400 nm axially [HH17]. SIM can be used with most fluorescent dyes and fluorescent proteins. Together with its ease of use, live-cell compatibility and commercial availability, it is widely used in biology and can achieve temporal resolution up to 188 Hz [Hua+18].

Finally, I would like to draw your attention to the last class of super-resolution techniques, namely *Single Molecule Localization Microscopy* (SMLM). This class is a little more diverse than the others, but all SMLM techniques have in common that they generate a pointillistic image from detected single molecule localization events recorded on a wide-field microscope. Here, a localization event or *localization* means determining the centroid position of an individual dye molecule by imaging it isolated from the rest of the dye molecules present in the sample. As a general

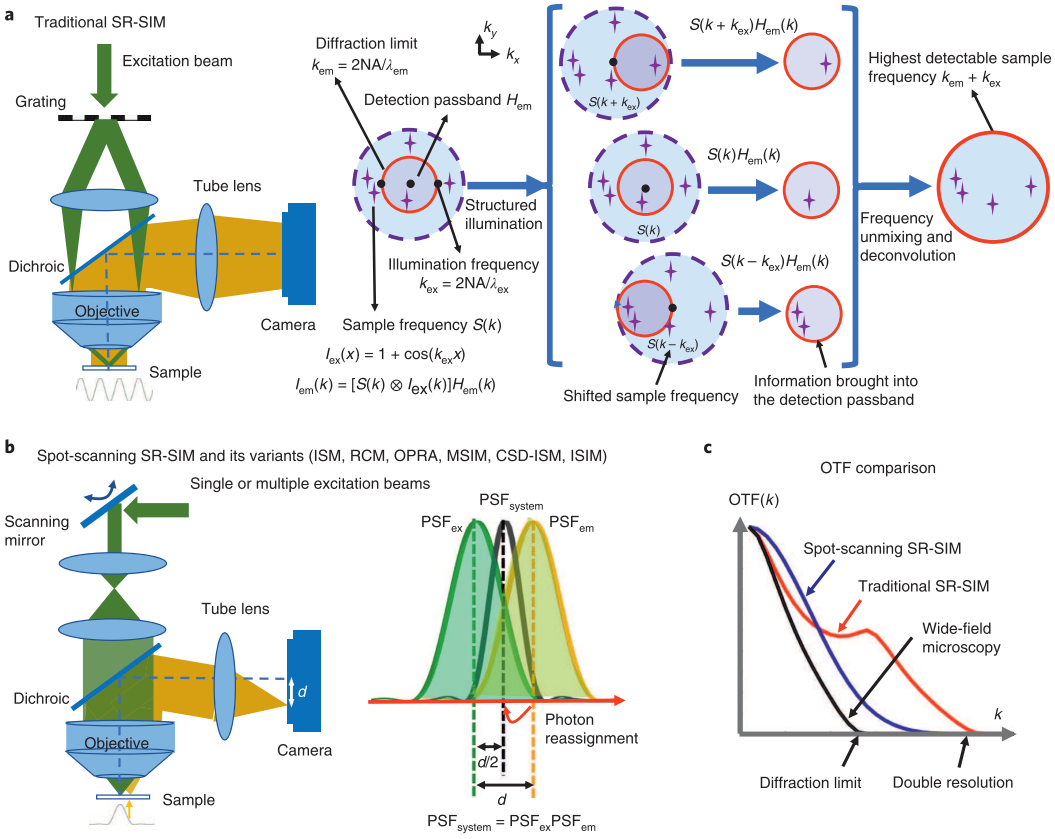

Figure 2.14.: Overview of SIM techniques. (a) In traditional SIM, the spatial frequencies in the sample are shifted to the detection passband by illuminating the sample with a periodic intensity pattern. Sampling the whole extended frequency space is done by rotating and shifting the pattern. (b) In spot-scanning approaches, the fluorescence emission is collected by an array detector. The collected fluorescence is reassigned based on the known distance to the excitation. (c) OTF comparison of traditional and spot-scanning SIM. Reproduced from [WS18] with permission.

concept, this was described in 1995 [Bet95]. First successful attempts were made by separating molecules based on their spectral properties or lifetimes, allowing for imaging one molecule per diffraction-limited area (DLA) on an otherwise more densely labeled structure [van+98; Hei+02]. Unfortunately, none of these strategies yields nearly enough discrete parameters to separate molecules in a typical fluorescently labeled biological structure. Nonetheless, the general concept of determining the centroid position ("*localizing*") of a molecule and the foundation for the algorithmic implementation were laid. A few years later in 2005, the separation of individual molecules in time was experimentally demonstrated with nanometer precision [Lid+05]. Here, the authors used intrinsically blinking semiconductor quantum dots to get only one quantum dot per DLA. The ratio of quantum dots residing in a non-fluorescent state was still not high enough to resolve a biological structure, but in the same year it was shown that organic fluorophores can exhibit precisely controllable photo-switching properties [BBZ05; Hei+05]. Not long after, the *stochastic optical reconstruction microscopy* (STORM) [RBZ06], the simplified *direct stochastic optical reconstruction microscopy* (*d*STORM) [Hei+08; Hei+09] and *photoactivated localization microscopy* (PALM) [Bet+06; HGM06] were introduced, finally demonstrating nanometer precision on biological structures experimentally. In recent years, SMLM techniques have evolved into a widely applied technique in biological research. Besides producing images with resolutions of 20 nm laterally and 50 nm axially [Sch+19], the fact that these data actually represent *statistical data* about the underlying fluorophore distribution is more and more exploited to gain quantitative data about biological processes [Sau13; NOG17].

2.4.1. Localizing Single Molecules with Nanometer Precision

The list of SMLM techniques mentioned in the previous paragraph is of course non-exhaustive. The main difference between them can be attributed to the specific ways to generate time-separated subsets of fluorescent molecules from the entirety of the sample. For an overview of those differences and how they evolved, I recommend the review [KPS14] written by my colleagues. In the following, I will explain the peculiarities of *d*STORM in more detail, as it is the method that was used for this thesis. Nevertheless, the theory of single molecule fitting and processing is largely agnostic of the particular method used for generating separated single molecule

emissions.

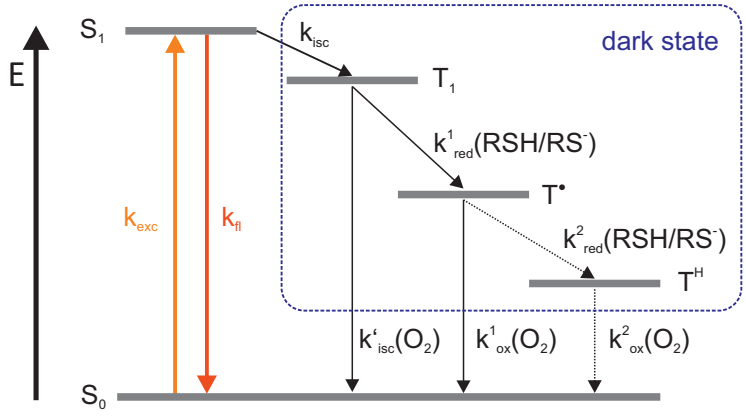

Figure 2.15.: Photoswitching Jablonksi diagram of a typical dye suitable for *d*STORM with conversion rates k. Upon excitation with the absorption wavelength, the dye will most likely emit a red shifted fluorescence photon. With a fine rate k_{isc} it will however cross over into the triplet state T_1. From there it can be further reduced to the radical anion $T^{\bullet}$ and leuco form T^H by reacting with thiolate. The triplet states are commonly called dark state, as they do not fluoresce. Rather, recovery of the ground state occurs by reacting with free oxygen. For clarity, only electronic states are depicted.

*d*STORM makes use of the photoswitching behavior of organic dyes. Some of them (for example Cy5 and Alexa 647®) exhibit very stable non-fluorescent *dark states* in reducing thiol environment with lifetimes of up to several seconds [van+11]. Moreover and in contrast to other techniques like PALM, a dye molecule can actively be recovered from the dark state by illuminating with a second laser, usually at 405 nm. This makes controlled *reversible photoswitching* possible, e.g. the stochastic switching of the same molecule between bright and dark states and subsequently localizing it several times before it finally bleaches [Hei+09]. Figure 2.15 depicts a typical Jablonski diagram of a photoswitching dye used for *d*STORM. Upon excitation the dye at its absorption wavelength, it can either fluoresce or undergo intersystem crossing to the triplet state T_1. From there, it can react with thiolate that is present in the medium to form the radical anion $T^{\bullet}$ with rate k^1_{red}. This state is quite stable (usually several seconds) and, for some dyes, accepts another electron to produce the fully reduced leuco form T^H with rate K^2_{red} that has even longer lifetime than $T^{\bullet}$. The mentioned triplet states are referred to as the

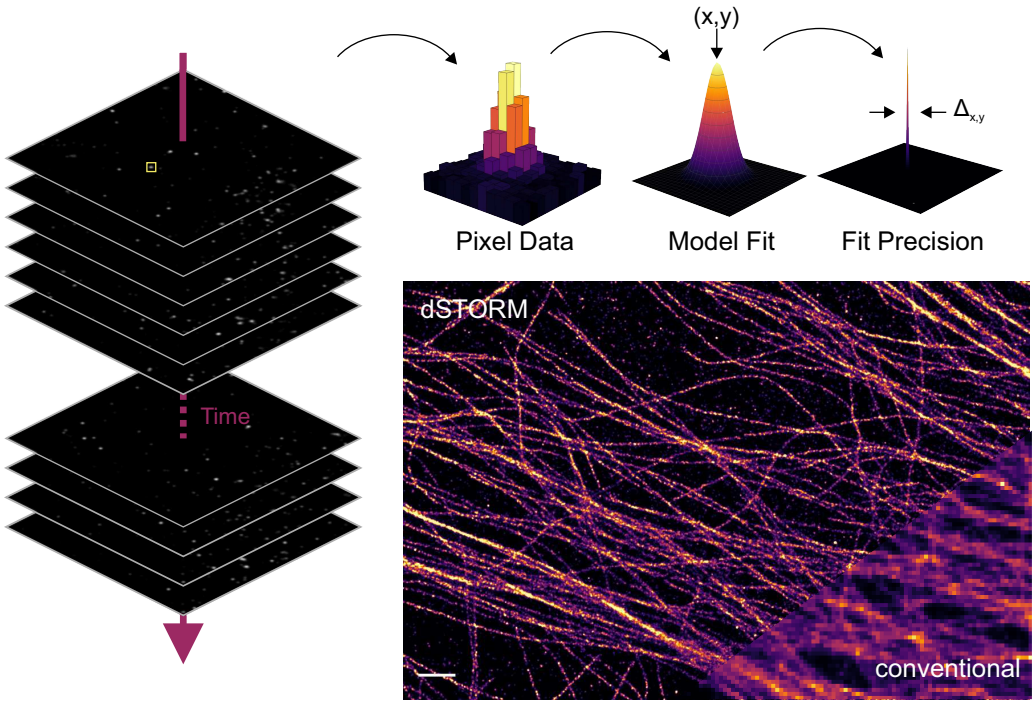

Figure 2.16.: *d*STORM single molecule localization process. A series of images with separated, stochastically emitting molecules is collected. Each candidate molecule is fit by a 2D Gaussian function to determine its position with sub-diffraction precision. The collected emitter positions are then reconstructed into a super-resolved image. Scalebar 2 µm.

dark state of the molecule. Each of the triplet states has a pathway back to the ground state that depends on the interaction of the dye with free oxygen in the medium. In essence, this enables us to precisely control the conversion rates to long-lived dark states by adjusting the thiol concentration in the medium, while we can control the rate of recovery to the actively fluorescing ground state by adjusting the oxygen concentration. This ensures that only a small, statistically chosen fraction of dye molecules is actively fluorescing at any point in time, making it possible to observe them through a microscope on a camera's pixel array.

While generating and observing single molecule diffraction patterns is vital to *d*STORM, finding the centroid position with high precision is of equal importance. This is done in post processing, after recording many (usually 10^4 to 10^6) frames of stochastically blinking fluorophores (Figure 2.16). As described in chapter 2.3.6,

the PSF is ideally in the form of an Airy disk. In reality, aberrations can be introduced by the system and the sample itself (i.e. refractive index mismatch between sample and objective immersion). Furthermore, the PSF is discretized by the camera pixels. The photons themselves are Poisson distributed in every pixel, owing to the particle nature of light, while the camera adds additional noise during read-out, which can be pixel-specific (for CMOS cameras). This can lead to deviations from the ideal Airy disk that cannot be neglected [Mor+10].

The most common procedure to find the centroid position of a molecule is to fit a model function to its emission pattern on the camera. The obvious way would be to use a theoretically derived PSF that incorporates all known parameters of the imaging system, like the *Richardson-Wolf* [RW59] or the more complex *Gibson-Lanni* [GL92] PSF models and fit them directly to the isolated emission patterns. However, this process has been proven to be computationally very expensive, while not providing better results than other approaches [SS14]. In practice, other approximations to the PSF deliver high precision, since they rely on less parameters than a full theoretically calculated PSF [Wol+12]. For most algorithms, the model function used is a simple 2D Gaussian function:

$$I\left(x,y\right)=\frac{I_0}{2\pi\left(\sigma_x^2+\sigma_y^2\right)}\exp\left[-a\left(\frac{\left(x-x_0\right)^2}{\sigma_x^2}+\frac{\left(y-y_0\right)^2}{\sigma_y^2}\right)\right]+\frac{b}{a^2} \tag{2.67}$$

Here, I_0 denotes the intensity of the emitter in the analyzed frame, a is a scaling factor, $\sigma_{x,y}$ are respective PSF widths in x and y and b is the mean local background per pixel area a^2 in the fitting region. Finally (x_0, y_0) are the coordinates of the emission center. As this intensity distribution is not derived theoretically one might wonder, if it is appropriate to use a Gaussian function for single molecule fitting. Nonetheless, this has been shown for typical experimental conditions [SR10], allowing for much faster computations speeds that can even approach real-time localization reconstruction on conventional computer hardware [Wol+10].

The precision of the coordinates obtained from single molecule fitting directly depend on the brightness of the fluorophore in a given frame, the background levels surrounding it and hence the signal-to-noise ratio (SNR). The localization

uncertainty (i.e the precision) of x_0 and y_0 can be calculated to

$$\Delta r = \sqrt{\frac{\sigma + a^2/12}{N}} \left(\frac{16}{9} + 4\tau \right) \tag{2.68}$$

$$\tau = \frac{2\pi b \left(\sigma^2 + a^2/12\right)}{N a^2} \ . \tag{2.69}$$

Here, τ is roughly equal to the background intensity b/a^2 divided by the peak intensity [Mor+10; RS14; TLW02]. From this equation we can reason that both bright emitting dyes, but also low background and therefore high SNR are crucial for accurate localizations. For 2D structures, background levels will be dictated by the camera background and a few scattered photons, but for thicker 3D samples, new strategies must be found to localize single molecules with high SNR by restricting background levels.

The last step that remains to produce a super-resolved image is to accumulate all localizations from a given sample and render them as an image. Usually, this is done by choosing a supersampled pixel size (e.g. 10 nm) and then assigning a pixel intensity to each pixel derived from the number of localizations found in that pixel weighted with the intensity of each localization. Usually, the pictures are color-coded to allow the view to perceive a greater dynamic range. This already allows great insight into biological structures. On the other hand, the time-encoded list of localizations together with their fit parameters (often referred to as "localization table") can be of all but equal value for further quantitative analysis [Sau13; NOG17].

The field of single molecule localization algorithms is far from settled. Recently it could be shown that while the position estimate by a Gaussian fit is very accurate, the intensity found by it can be systematically inaccurate. More specifically, the apparent intensity found by a Gaussian fit depends on the position of the emitter in z with respect to the focal plane of the objective [FSv16]. Another recent development is the introduction of scientific Complementary Metal-Oxide-Semiconductor (sCMOS) cameras to the field of SMLM. The main difference to the most commonly used Electron Multiplying Charge-Coupled Device (EMCCD) cameras is, that each pixel on a sCMOS camera has its individual amplifier circuit for read-out. This enables much faster read-out rates, while introducing pixel-specific characteristics, namely noise, gain and background levels. However, it can be shown that sCMOS

outperform EMCCD cameras, if only the constant background level is corrected before single molecule localization is carried out [Lin+17]. The comparable low price of sCMOS cameras has enabled new experimental multi-camera designs [Bab18]. Finally, with the advancement to various 3D localization techniques, new challenges presented itself to fitting algorithms, prompting an ongoing debate and a challenge for the best localization algorithm [HS16; Sag+18]. So far, there is no solution that satisfies all imaging conditions. Nevertheless, using experimentally acquired PSFs instead of theoretical models to fit the SMLM data is one development that is very promising, since it incorporates all possible aberrations into the fit function and allows arbitrary PSFs [Ari+18; Li+17].

2.4.2. Charting the Third Dimension

Standard SMLM images are actually a projection of a three-dimensional section of the sample onto a 2D image. This is because in a diffraction-limited system, the PSF will expand ("defocus") symmetrically around the focal plane. This is immediately evident when looking at the ray diagram of a microscope (Figure 2.9) in paraxial approximation. The axial extend of the 3D section can be controlled be carefully filtering the PSF width [Pal+15]. However, since the defocusing behavior is symmetric, only the absolute distance from the focal plane can be estimated by measuring the PSF diameter, not the direction. The projection of three-dimensional features of the sample to 2D can lead to misinterpretations and bad image quality. Ultimately, to gain a deeper insight into the sample, 3D imaging is often required. Over the last couple of years, different techniques have emerged that break the axial symmetry of the PSF and allow to encode its precise z position. In the following, I will give a brief overview of the different classes of techniques with special emphasis of astigmatism, since this method was used in this thesis. For an overview on these techniques I recommend the review by *Diezmann, Shechtman* and *Moerner* [DSM17]. Remarkably, recent advancements have also been made to exploit the system-inherent aberrations to estimate axial single molecule positions without modifying the system a priori [FSv16; Li+17].

Multiplane and Interferometric Methods

Interferometric approaches employ two opposed parfocal objectives that nearly cover the whole solid angle for fluorescence light collection. The light is then brought to interference with a special 3-way beam splitter onto four cameras. This enables a single photon to interfere with itself coherently, precisely modulating the interference pattern imaged on the four cameras. The relative intensity of the four images from a single dye can be evaluated to estimate the z position with precisions below 5 nm [Sht+09; Kan+10]. This technique is termed iPALM or 4Pi-SMS. It is arguably the experimentally most complex technique and limited to an axial range of $\sim \lambda_{em}/2$ [Mid+08].

Biplane approaches however, are much more easy to implement. Here, an emitter is simply imaged on two separate image planes by placing a 50:50 beam splitter in the detection path, while applying a slight offset between the image planes. The two images are then recorded by two separate cameras or on separate areas on the same camera [Pra+04; Jue+08]. Hence, a dye molecule that is in focus on one camera will by defocused on the second camera. By evaluating the PSF diameter on both cameras, the z position of the molecule can be extracted. An advantage of this technique is that the common Gaussian fitting can still be used with existing SMLM software.

Near-Field Coupling

Recently, methods that exploit near-field coupling have gained more popularity. One way to use near-field coupling for z resolution is a technique called supercritical angle fluorescence (SAF) microscopy [RV04; DMR14; Bou+15]. Here, the fact that with a refractive index mismatch between sample and cover slip, fluorescence light will not propagate into the glass at angles greater than the critical angle ($\approx 61°$ for a water/glass interface). However, if the emitter is close enough to the interface, the light couples evanescently into the glass at greater angles (i.e. supercritical). This light can be collected with high NA objectives. By employing a biplane detection and selectively filtering the supercritical light in a plane corresponding to the BFP of the objective in one path, one can effectively determine the amount of evanescent coupling, which is highly dependent on the distance from the cover slip. One advantage of this technique is that it provides an absolute measure of the distance

from the cover slip, while other methods usually only can provide relative measures. A disadvantage would be that it is limited to an axial range of $\approx \lambda_{\mathrm{em}}$ above the cover slip.

PSF Shaping

The methods belonging to the class of PSF shaping are arguably the most widely used ones. They all have in common, that additional optics are placed in the detection beam path to break the axial symmetry of the PSF by applying phase shifts to the propagating light.

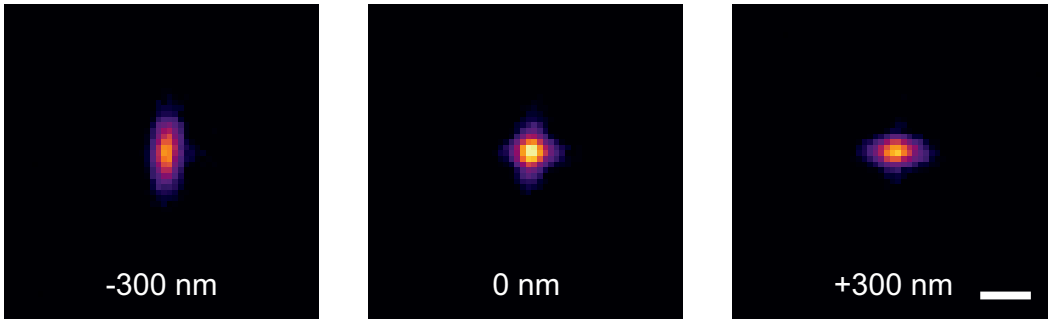

Figure 2.17.: Astigmatic defocusing of a 100 nm fluorescent bead in the LLSM. The vertical and horizontal elongation of the PSF above and below the circle of least confusion ($z = 0$) is clearly visible. Indicated heights are measured along the detection objective axis. Scalebar 1 µm.

In its simplest manifestation, a weak cylindrical lens is introduced into the beam path, usually in front of the camera. This produces a mild astigmatism in the image, that elongates the PSF vertically or horizontally, depending on the z position of the emitter. This technique was initially used in single particle tracking [KV94; HMS07] and was adapted to SMLM soon after its invention [Hua+08a; Hua+08b]. Usually, a higher order polynomial was fitted to the PSF widths $\sigma_x(z)$ and $\sigma_y(z)$ with respect to z. Nonetheless, this does not model all systems sufficiently well and has the disadvantage that a bad fit to a certain point of the curve will have a global impact. To this end, fitting of the defocusing curve with a cubic B-spline was introduced, departing from a physical model of defocusing behavior and instead modeling and interpolating the defocusing function as it is [Pro+14]. As a convention, the position at the circle of least confusion (i.e. $\sigma_x = \sigma_y$) is usually chosen as the zero point

for calibration. An advantage of the astigmatic PSF is its small size, allowing relatively high emitter densities to be resolved by fit algorithms. This advantage and the fact that its implementation and data evaluation are rather easy ultimately made astigmatism the 3D localization method of choice for my thesis.

In theory very similar, but experimentally a bit more complex is the introduction of a phase shift by a Spatial Light Modulator (SLM) [She+14], deformable mirror [Ize+12] or a lithographically etched dielectric phase mask [Gah+13] that is introduced into a plane conjugate to the BFP of the objective. Using a computer-controllable device such as a SLM or deformable mirror allows for examining the effects of different phase shift patterns and quickly change between them. A number of different phase patterns have been established for different use cases. These have a wide range of behavior regarding size of the PSF, usable z range and attainable resolution and can even be made wavelength-specific [She+16]. However, the size of these PSF is considerably larger, demanding much sparser fluorophore blinking to prevent overlaps and therefore artifacts during fitting. At the same time, the available photon budget from a single dye is spread over the larger PSF, demanding much brighter fluorophores. Furthermore, the computational complexity of fitting those PSF is also well beyond Gaussian fitting.

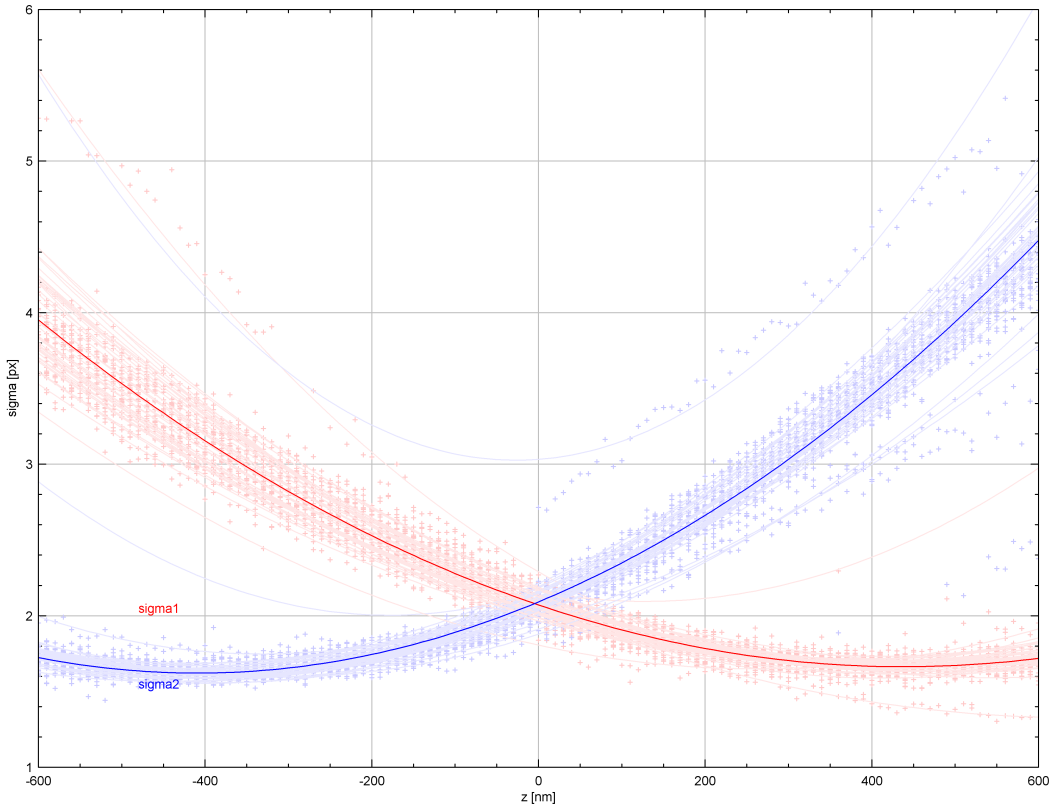

Figure 2.18.: Dependence of lateral PSF width on emitter z position for astigmatic imaging measured in the LLS. A ensemble of many fluorescent beads at different lateral and axial positions was imaged and fit with a 2D Gaussian using Thunderstorm [Ove+14]. Red and blue crosses depict the individual PSF widths in x and y, respectively. The solid line gives the ensemble average defocusing curve. Pixel size 103.8 nm.

2.5. Illumination Strategies for SMLM

Ideally, the illumination for SMLM experiments would be completely confined to the currently observable volume, i.e. the depth of field of the detection objective or even a thinner section. This would ensure an efficient excitation of the fluorescent dye with the available illumination photon budget and diminish adverse effects. I showed in equation (2.68), that the achievable localization precision directly depends on the signal to noise ratio. Moreover, for live-cell experiments, limiting the light exposure is absolutely vital to prevent photodamage and phototoxicity to biological structures [Wäl+15]. In addition, restricting the illumination to the detectable volume is also key to prevent premature bleaching of dyes before being able to observe them.

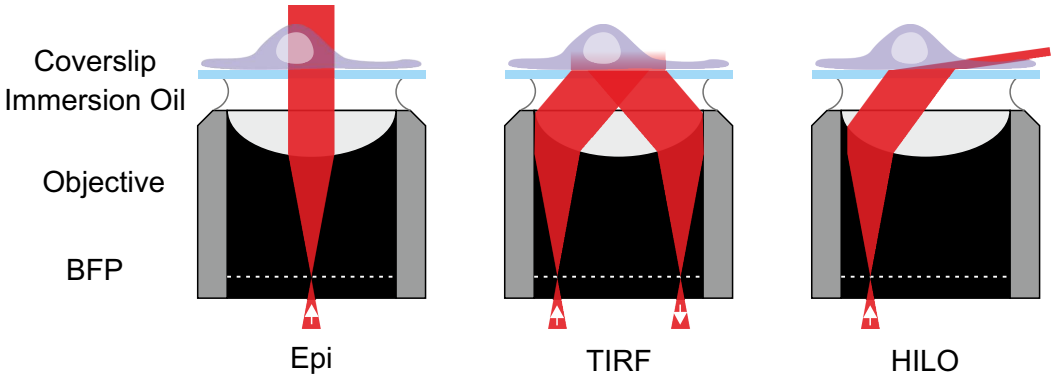

Figure 2.19.: Common illumination strategies for SMLM with refractive index mismatch between sample and cover slip. The illumination laser beam is focused on the BFP of the objective of a microscope. Focusing it on the center produces a parallel column of light (Epi). Focusing the laser off-center produces a highly inclined and optical laminated sheet for illumination (HILO), where the angle can be adjusted by the lateral position of the laser in the BFP. Focusing the laser further off-center will eventually cause total internal reflection (TIRF) at the cover slip/sample interface, leaving only an evanescent field in the sample.

Figure 2.19 shows the most common illumination strategies for SMLM when using conventional single-objective microscopes. The default illumination mode is *epi illumination*, where the sample is just illuminated with a parallel beam that is wider than the field of view (FOV). This illumination mode works for all objectives (dry, water immersion, oil immersion, dipping) and is therefore widely used in routine

microscopy as well. Nevertheless, huge proportions of the sample are illuminated, that are not in focus (i.e. imaged) at the same time. This causes unnecessary photodamage and phototoxicity while degrading image SNR at the same time. Even so, for some SMLM experiments, epi illumination is necessary [Hua+08a; KPS14]. Nonetheless, when doing SMLM in multiple z planes consecutively in epi illumination, premature bleaching of dyes can occur before they can be localized. This has to be kept in mind as it can potentially introduce artifacts to the image.

Focusing the excitation laser in the BFP close to the edge of the entrance pupil will produce a parallel beam at an angle to the cover slip that is greater than the critical angle for refraction according to Snell's law (2.5) with $\sin \alpha_1 = 1$:

$$\alpha_{\text{crit}} = \sin^{-1}\left(\frac{n_1}{n_2}\right) \tag{2.70}$$

Total internal reflection will occur (TIRF) at the glass/sample interface and only an evanescent field will protrude into the specimen volume, quickly decaying in intensity according to

$$I(z) = I_0 e^{-\frac{z}{\lambda z_0}} \tag{2.71}$$

where typically $z_0 \approx 0.2$, but slightly depending on the ratio of refractive index between sample and glass [Axe01]. This illumination is very popular in SMLM, since it effectively eliminates background fluorescence for a specimen very close to the cover slip. Surely, samples further away from the cover slip than $\sim \lambda/2$ cannot be observed with TIRF illumination. Moreover, TIRF does occur when the refractive index of the specimen is smaller than that of the objective immersion, making it only available for oil immersion objectives in combination samples of smaller refractive index.

Moving the laser focus from the edge of the BFP slightly back towards the center will create a *highly inclined and laminated optical sheet* (HILO) [TIS08]. The angle of the HILO illumination can be adjusted to a certain extend by laterally moving the laser focus in the BFP of the objective. Typically, the illumination sheet is between 5 µm and 12 µm thick, depending on the desired FOV. This technique also has the potential to reduce the illuminated volume when compared to epi illumination and allows for accessing deeper parts of the sample, while TIRF is restricted to the cell

plasma membrane and its immediate surrounding. Nonetheless, the thickness of the sheet is much greater than the dept of field of a typical high NA objective used for SMLM ($\approx 1\,\mu m$).

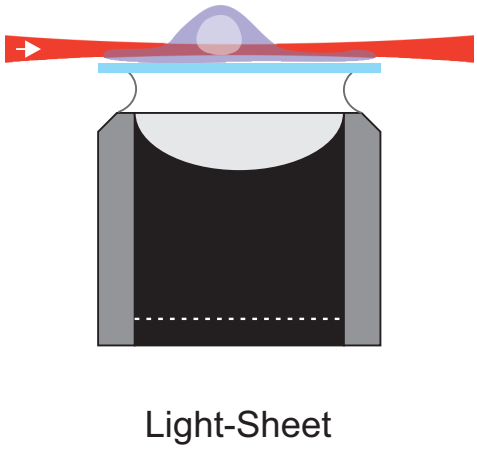

Figure 2.20.: Concept of light-sheet illumination. A thin sheet is formed perpendicular to the detection objective, extending orthogonal to the paper plane. By carefully forming the sheet, it can be specifically tailored to the needs of the imaging task at hand and steered to the plane of interest.

In summary, the introduction of TIRF and HILO to the field of single molecule localization microscopy already helped its advancement a great deal by providing superior SNR compared to epi illumination for single molecule localization. Nonetheless, TIRF is restricted to a thin section at the cover slip, while HILO still illuminates a volume that is much greater than the depth of field. At this point, light-sheet illumination comes in (Figure 2.20). Actually being an old idea, dating back to 1902 [SZ02], it has gained great popularity in fluorescence microscopy recently [HS09]. However, early implementations to fluorescence microscopy focused on imaging large specimen with low magnification (i.e. whole organism) or with large FOV and low magnification [VBS93; Fuc+02]. More recently, light-sheet illumination was used to image deep inside the specimen with better SNR and to effectively improve the z resolution of the low-magnification objective with the light-sheet in living organisms [Hui+04]. However, for SMLM applications, light-sheet illumination has to fulfill quite different requirements. Here, it is mainly used to restrict the illumination completely to the detectable volume, thereby improving

SNR and eliminating premature photobleaching outside of the detection volume. This finally enables SMLM imaging in big volumes (i.e. whole cells) without the adverse effects of epi illumination. However, despite being a very powerful technique, SMLM in combination with light-sheet illumination is only available to a few groups worldwide and requires custom-building a microscope with sophisticated illumination optics [PH17].

In the remainder of this chapter, I will highlight the application of Gaussian and Bessel beams for SMLM light-sheet illumination. Finally, I will introduce the concept of optical lattices that is necessary for producing lattice light-sheets. For a more in-depth look into the history of light-sheet and its various flavors, I refer the reader to great reviews found in [Ola+18; San11; PH17; HS09].

2.5.1. Light-Sheets with Gaussian and Bessel Beams

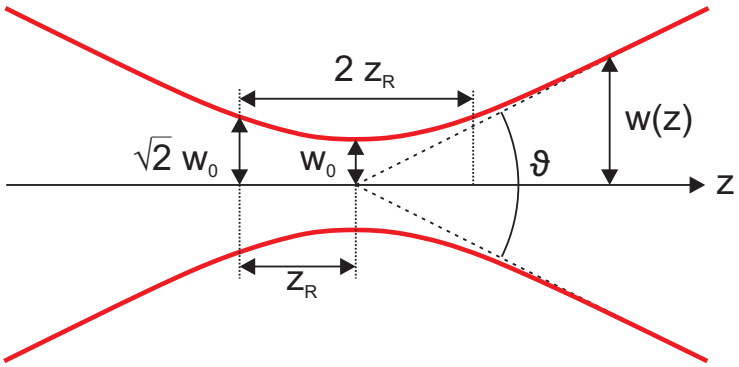

Figure 2.21.: Beam waist of a focused Gaussian beam. For any Gaussian beam, the minimum beam waist w_0 is directly related to the Rayleigh distance z_R and the divergence angel ϑ, resulting in boundary conditions for the use as a light-sheet.

The simplest implementation that comes to mind when thinking about creating a light-sheet for fluorescence microscopy, is to just construct a second beam path orthogonal to the detection objective and focus a laser beam to a thin sheet. On the one hand, this can be done with a cylindrical lens that will focus a widened beam to a stripe [Hui+04; Pit+13]. On the other hand, one can also focus the laser to a small spot and then scan this focused beam rapidly in the object plane of the detection microscope [Kel+08].

Usually, lasers with TEM_{00} Gaussian profile are used, which will lead to an intensity distribution that remains Gaussian in x and y when focused by a lens (Figure 2.21). When focused by a cylindrical lens, this results in a non-homogeneous illumination of the object plane, which is alleviated by the latter approach. We know from chapter 2.3.3 that the width of the beam scales with

$$w^2(z) = w_0^2 \left[1 + \left(\frac{\lambda z}{\pi w_0^2}\right)^2\right] \quad . \tag{2.46 revisited}$$

Moreover, the distance from the waist at which its intensity drops to half is defined as Rayleigh distance z_R according to

$$z_R = \frac{\pi w_0^2}{\lambda} \quad . \tag{2.72}$$

So for $z \gg z_R$ we can approximate

$$w(z) \approx \frac{z w_0}{z_R} \tag{2.73}$$

and consequently approximate the angle of divergence as well by

$$\vartheta \approx \frac{2w(z)}{z} = \frac{2w_0}{z_R} = \frac{2\lambda}{\pi w_0} \quad . \tag{2.74}$$

Now we can draw some clues from these equations. For instance, let us consider we want to have a Gaussian light-sheet that has a Rayleigh length corresponding to the field of view of our detection microscope, for instance $2z_R = 30\,\mu m$. Then at a laser wavelength of 640 nm, we will get a beam diameter of $2w_0 = 3.5\,\mu m$ at the waist, which is about three times the depth of field of a high NA detection objective. Consequently, a Gaussian beam will either illuminate significant out-of focus proportions of the sample, or the FOV of the microscope has to be sacrificed.

To address specific shortcomings of the Gaussian light-sheet and optimize specific parameters for the imaging challenge at hand, many different light-sheet implementations have been developed [Ola+18; GPM18]. One that particularly stands out and is of major importance to this thesis is the use of *non-diffracting beams*. Imagine an electrical field comprised of a set of plane waves, where all wave vectors $\vec{k}_n$ lie on the surface of a cone that points in the z direction, so $\vec{k}_n \cdot \hat{e}_z = k \cos\vartheta$ for all

n, where ϑ is the half-angle of the cone. For the propagating field in free space it follows that

$$\vec{E}(\vec{r},t) = \sum_{n=1}^{N} \vec{E}_n \exp\left[i\left(\vec{k}_n \cdot \vec{r} - \omega t\right)\right] \tag{2.75}$$

$$= \exp\left[i\left(kz\cos\vartheta - \omega t\right)\right] \sum_{n=1}^{N} \vec{E}_n \exp\left[i\left(k_{x,n}x + k_{y,n}y\right)\right]$$

$$= \vec{E}(x,y)e^{i(kz\cos\vartheta - \omega t)} \ . \tag{2.76}$$

This means that the electric field propagates along z without changing its spatial distribution in the lateral xy plane, hence the name non-diffracting [Dur87; DJE87]. The condition that the wave vectors lie on a single cone is equivalent to the constraint that the light entering an objective lens is restricted to points on an infinitesimal thin ring on the BFP. One popular non-diffracting beam is produced by filling a infinitesimal thin ring in the BFP with a continuum of wave vectors. In scalar approximation, the field is then

$$E(\vec{r},t) = A\exp\left[i\left(kz\cos\vartheta - \omega t\right)\right] \int_0^{2\pi} \exp\left[ik\sin\vartheta\left(x\cos\varphi + y\sin\varphi\right)\right]\, d\varphi \tag{2.77}$$

where I have expressed the wave vector in spherical coordinates according to $\vec{k} = k\left(\sin\vartheta\cos\varphi\hat{e}_x + \sin\vartheta\sin\varphi\hat{e}_y + \cos\vartheta\hat{e}_z\right)$. If we also express $\vec{r} = \varrho\cos\xi\hat{e}_x + \varrho\sin\xi\hat{e}_y + z\hat{e}_z$, $\varrho = \sqrt{x^2+y^2}$ in cylindrical coordinates, (2.77) transforms to

$$E\left(\vec{r},t\right) = A\exp\left[i\left(kz\cos\vartheta - \omega t\right)\right] \int_0^{2\pi} \exp\left[ik\varrho\sin\vartheta\left(\cos\xi\cos\varphi + \sin\xi\sin\varphi\right)\right]\, d\varphi \tag{2.78}$$

where we can use the trigonometric identity $\cos\xi\cos\varphi + \sin\xi\sin\varphi = \cos\left(\varphi - \xi\right)$ to get:

$$E\left(\vec{r},t\right) = A\exp\left[i\left(kz\cos\vartheta - \omega t\right)\right] \int_0^{2\pi} \exp\left[ik\varrho\sin\vartheta\cos\left(\varphi - \xi\right)\right]\, d\varphi \tag{2.79}$$

Here we can identify the integral representation of the Bessel kind and order zero, $J_0(\alpha) = {}^1\!/_{2\pi} \int_0^{2\pi} \exp(i\alpha \cos\beta)\, d\beta$, to finally arrive at

$$E(\vec{r}, t) = E(\varrho, z, t) = \frac{A}{2\pi} J_0(k\varrho \sin\vartheta) \exp\left[i\left(kz\cos\vartheta - \omega t\right)\right] \ . \tag{2.80}$$

In other words, when illuminating the BFP objective with a infinitesimal thin ring of plane waves, this results in a circular symmetric amplitude distribution following $J_0(k\varrho \sin\vartheta)$ in any xy plane, since the beam is propagating without diffraction along the z axis. This type of beam is called *Bessel beam* [DME88]. The lateral dimensions of the beam scales inversely with the numerical aperture of the excitation objective since $\mathrm{NA} = n \sin\vartheta$ and linearly with the excitation wavelength.

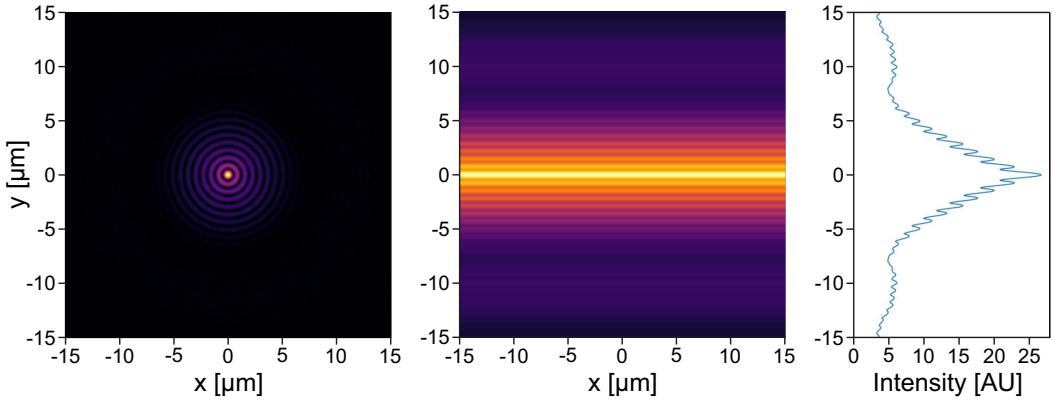

Figure 2.22.: Simulated Bessel beam for a finite, annular illumination in the BFP. (Left) Simulated xy intensity distribution for for a beam propagating in z with $\lambda = 647$nm. (Center) Resulting intensity when scanning the intensity in the x direction to create a light-sheet. (Right) Cross-section of the scanned light-sheet showing the contribution of side lobes to the overall width of the scanned light-sheet.

The properties of Bessel beams are of course very intriguing for the application in light-sheet microscopy, which was pioneered by *Fahrbach et al.* [FR10; FSR10; FR12] and *Planchon et al.* [Pla+11]. Here, the authors demonstrated the Bessel beam's capabilities experimentally and could also show a "self-reconstructing" property of the Bessel beam. This means that the propagating beam quickly reconstructs the shadow of a small, absorbing object that is placed in the beam. This is specifically useful for light-sheet illumination, since Gaussian light-sheets can produce artifacts if strongly absorptive particles are present in the sample. On the other

hand, each lobe of a Bessel beam contains approximately the same amount of energy as the central spot [DME88]. Due to this, albeit achieving better performance than epi illumination, substantial out-of-focus excitation leads to sub-par image quality with scanned Bessel beam light-sheets (Figure 2.22).

In reality, achieving an infinitely small ring in the BFP of the objective is impossible and would lead to zero power transmission. Instead, an annulus with finite thickness is produced, resulting in a Bessel-Gauss beam. Here, the radial intensity distribution is enveloped by a Gaussian function, attenuating outer rings of the Bessel function. For a constant excitation NA, the thinner the annulus, the more Bessel-like the beam will be, the more energy will exist in its side lobes and the longer its axial extend. On the other hand, the wider the annulus is chosen, the more Gaussian the beam will become, the smaller the energy contained in side lobes and the shorter the axial extend [Gao+14]. Hence, the annulus width is an important parameter and should be chosen to produce a beam with a length just long enough to cover the FOV.

2.5.2. Optical Lattices and Bessel Beam Arrays

In a key paper in 1994, the connection between non-diffracting beams and crystallography was made, using the formalism of solid state physics to describe the non-diffracting field [PCG94]. Originally, this generalized formalism was intended for multi-objective illumination that is used in 2D and 3D optical traps. Over a decade later, *Betzig* showed the potential applicability to microscopy by examining optical lattices that can be created with one objective and satisfy the condition for non-diffracting beams (2.76) [Bet05b; Bet05a]. It wasn't until 2004, that the first experimental realization was achieved [Che+14].

In the following, I will review the theory behind optical lattices and finally compare it to the beam generation of using an array of Bessel beams.

Optical Lattices and Bound Optical Lattices

Let us consider the electric field $\vec{E}(x, y)$ in equation (2.76) as a function that is periodic in two dimensions:

$$\vec{E}(x, y) = \vec{E}(\vec{r} + m_1\vec{a} + m_2\vec{b}) \tag{2.81}$$

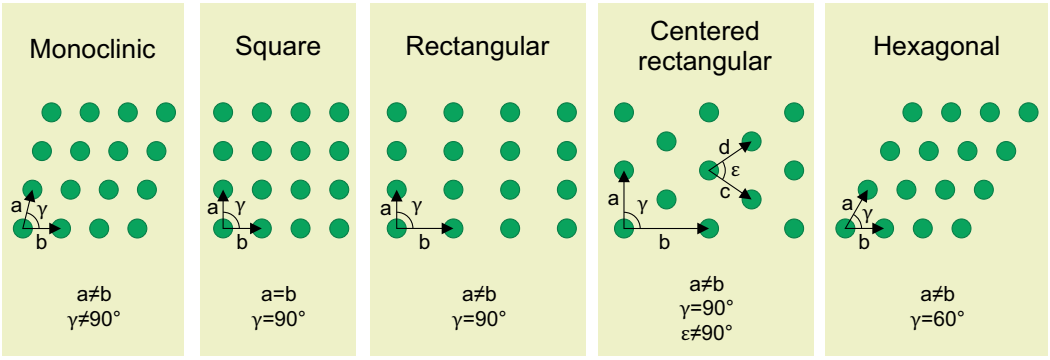

Figure 2.23.: The five 2D Bravais lattices. The lattices are defined by the length of their primitive vectors a, b and the angle γ between them.

where $\vec{a}, \vec{b}$ are two-dimensional *primitive vectors* and m_1, m_2 can be any integers, hence the 2D periodic lattice pattern is fully defined. In two dimensions, there only exist 5 unique lattices, termed the *Bravais lattices* (Figure 2.23). For a non-diffracting light beam to have the cross sectional symmetry of one of the Bravais lattices, it must be comprised of at least three wave vectors $\vec{k}_n$ that lie on the surface of the same cone [PCG94]. Such a beam is then called *optical lattice* [PCG94; Che+14].

From equation (2.75), we note that the spatial dependence of the electric field is separable from the polarizations $\vec{E}_n$ of the plane waves creating it. Therefore, the symmetry and periodicity of the lattice only depends on the $\vec{k}_n$, while the pattern of the electric field repeating in each unit cell depends on the $\vec{k}_n$ and $\vec{E}_n$ [PCG94]. To achieve a desired Bravais lattice, multiple pairs of primitive vectors can be found. For each pair there is a corresponding wave vector set $\left\{\vec{k}_1, \vec{k}_2, \vec{k}_3\right\}$ that produces the desired optical lattice upon superposition. However, the period of the lattice scaled to the wavelength is limited to a series of discrete values defined by the lattice parameters. Due to the diffraction limit, there is a smallest period for every three wave vector set composing one of the Bravais lattices [Bet05b]. This set is called the *fundamental* lattice, while larger periods are termed *sparse* lattices.

Every Bravais lattice has a group of symmetry operations that transform it onto itself. Applying these symmetry operations to the wave vector set $\left\{\vec{k}_1, \vec{k}_2, \vec{k}_3\right\}$ will therefore not change the symmetry and periodicity of the lattice. However, the

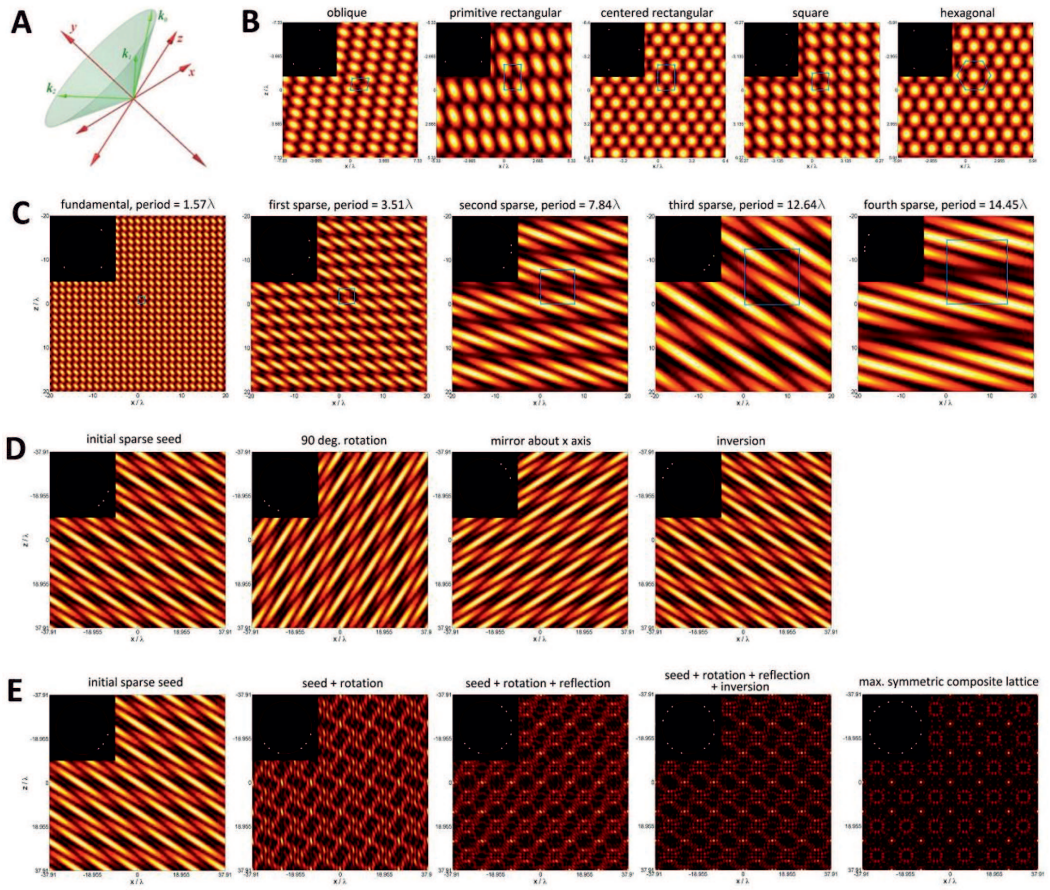

Figure 2.24.: Synthesis of optical lattices. (A) The wave vectors comprising the lattice lie on a cone. Note that this lattice will propagate along y. (B) The five fundamental Bravais lattices. (C) Square lattice with different periods have the same symmetry, but different intensity distributions. (D) Applying the three available symmetry operations to a sparse square lattice. (E) Stepwise combination of the four lattices of (D) yields the maximally symmetric sparse square lattice with confined excitation spots. Insets show corresponding wave vectors in the BFP. From [Che+14], reprinted with permission from AAAS.

electric field in each unit cell will also be transformed by the symmetry operation. Combining wave vector sets that are derived from a given set by all available symmetry operations of the lattice will result in a *composite* lattice comprised of more than three wave vectors. Because the wave vectors converge from the broadest azimuthal angle possible for a given Bravais lattice, the 2D spatial frequency content of the electric field will be maximized and the resulting lattice is called *maximally symmetric composite lattice* [Bet05b].

If the input polarizations $\vec{E}_n$ are maximally projected onto the desired polarization $\vec{E}$, constructive interference will lead to a highly confined intensity maximum at one point in the unit cell, while partial destructive interference will provide a low background otherwise. The contrast of the maximum directly depends on the number of wave vectors that comprise the optical lattice. Since hexagonal and square lattices have the greatest symmetry in 2D, their maximally symmetric composite optical lattice will provide the tightest excitation confinement in the form of multifocal arrays [Bet05a].

Now that we have discussed the theory of optical lattices, we can take a step back and look at their applicability to light-sheet microscopy. So far, we are able to synthesize an electrical field with highly confined intensity maximums filling the xy plane according to a Bravais lattice and propagating diffraction-free along z. Nonetheless, for a light-sheet, we need confinement in one direction perpendicular to the propagation direction and for experimental realization, we will need to illuminate a finite area of the BFP and not a set of infinitesimal small points, which the set of $\vec{k}_n$ correspond to. Let us consider the detection objective axis is y, so we want to confine the optical lattice in this direction, while keeping the high spatial frequency content in the x direction. The solution is similar to the Bessel beam case: We will broaden the ring on which the $\vec{k}_n$ reside in the BFP to a finite annulus. To keep the high spatial frequency content in x, we will only spread the energy of the $\vec{k}_n$ in stripes along y with maximum extend defined by the annulus diameter. Effectively, this results in a *bound lattice* [Bet05a] where we trade a finite energy throughput for reduced modulation along y. Fortunately, both of which were our goals. By extending the stripes in y, the resulting lattice can effectively bound to an envelope that spans less one lattice period or less in y, while keeping high modulation in x, finally creating an attractive pattern for light-sheet microscopy.

Similar to the Bessel beam, the resulting lattice will not be strictly non-diffracting

anymore. As the annulus width and the ideal lattice parameters are to some point empirically found, I will provide more detail in experimental chapter 3.2, where the application of a bounding function to the 2D lattice is also shown.

Bessel Beam Arrays

Finally, I will review another physical picture to look at lattice light-sheet. Here, we start out with a linear array of coherent Bessel beams, propagating along z and centered on the x axis with distance d between them. Assuming identical phase of the individual beams and recalling that their side lobes alternate in phase, we will get constructive interference along the x axis at spacings

$$d_{\text{constr}} = \frac{i\lambda}{\text{NA}_{\text{min}}} \tag{2.82}$$

where $i \geq 1$ is an integer and NA_{min} is the minimum NA defined by the inner annulus diameter [Che+14]. Very similar to a highly bound optical lattice, this also results in a highly confined intensity distribution, since the side lobes of the individual Bessel beams interfere destructively away from the x axis.

Experimentally, a constructively interfering linear array of Bessel beams can deliver the same performance as a highly bound optical lattice and is in fact nearly identical to a bound square lattice [Che+14]. The detailed use cases of different lattices will be discussed later in experimental chapter 3.2 together with the overall experimental PSFs.

3 The Lattice Light-Sheet Microscope

In this chapter, I will outline the experimental realization of a lattice light-sheet microscope (LLSM) optimized for single molecule imaging with *d*STORM. In comparison to a conventional SMLM research microscope, the lattice light-sheet beam shaping adds major complexity to the optical setup, with the illumination optics comprising the majority of the optical system. Moreover, the microscope is designed with water-dipping illumination and detection objectives to allow for measurements of thick samples and living cells at 37 °C, if desired. This requires the optics to be mounted on a vertical breadboard to allow for the two objectives to dip into a horizontal sample bath.

I will begin this chapter by explaining the optical schematics of the system and detailing the function of several important parts. Following, I will highlight the theoretical simulation of lattice light-sheets to find an ideal light-sheet for *d*STORM and other imaging tasks. Then, I will showcase different acquisition modes of the system and detail the timing and synchronization constraints that are imposed on the system by different components. Processing and evaluating the vast amounts of data that can be generated by the LLSM is another challenge that I will describe here, along with a Python package that I developed to help solving it. Finally, I will detail various sample preparation techniques that I used throughout this thesis.

3.1. Experimental Realization: Optics of the LLSM

The optical schematic of the lattice light-sheet microscope (LLSM) is shown in Figure 3.1 and detailed parts lists can be found in Table A.1 and Table A.2 in the appendix. Several renderings of the optomechanical realization of the microscope and the laser combiner can also be found in the appendix. The original de-

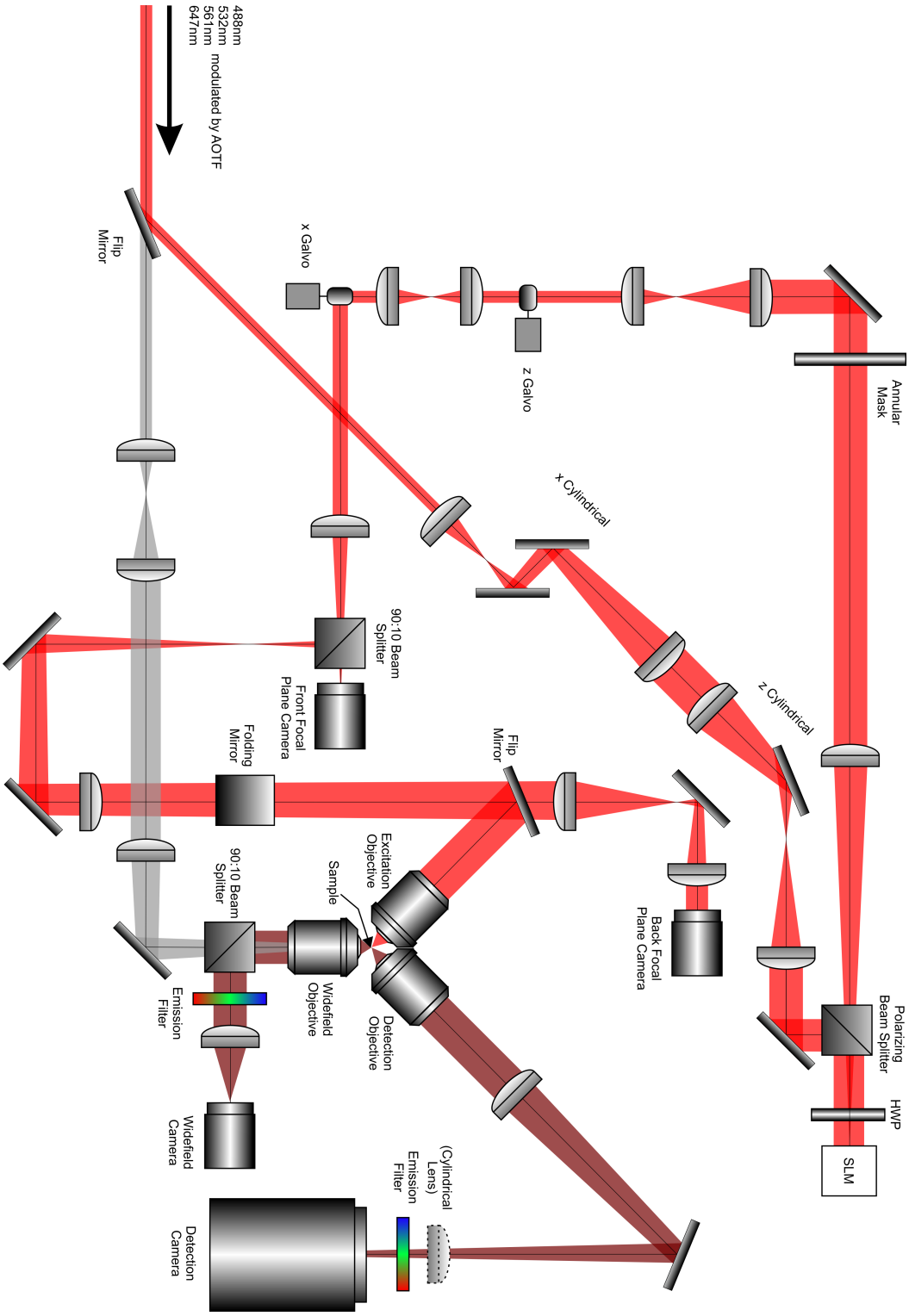
488nm
532nm
561nm
647nm
modulated by AOTF
Flip Mirror
x Galvo
z Galvo
Annular Mask
x Cylindrical
z Cylindrical
90:10 Beam Splitter
Front Focal Plane Camera
Folding Mirror
Flip Mirror
Back Focal Plane Camera
Excitation Objective
Sample
90:10 Beam Splitter
Widefield Objective
Detection Objective
Emission Filter
Widefield Camera
(Cylindrical Lens)
Emission Filter
Detection Camera
Polarizing Beam Splitter
HWP
SLM

Figure 3.1 (previous page): Optical schematic of the LLSM beam path. The combined beam of the four lasers (red) arrives at the microscope and is expanded in x and shrunk in z by two sets of cylindrical lenses to illuminate a thin stripe on the SLM. The diffraction pattern of the SLM is imaged on the annular mask, which filters unwanted diffraction orders and restricts the illumination to an annulus. The annulus is imaged onto the x and z scanning galvonometric mirrors by to sets of releay lenses. From there, it is imaged by two relay lenses onto the BFP of the excitation objective. Fluorecent light from the sample (maroon) is collected by the detection objective and imaged onto the main camera. It is also possible to illumintate the sample from down below in epi configuration (grey). In the beam path, there are two diagnostic cameras at planes conjugate to the BFP and FFP. Not to scale. For clarity, not all mirrors are shown.

sign was presented in [Che+14; Leg+16] and is partially protected by two patents [Bet16; BW18] that were licensed by the University of Würzburg under a research license agreement, upon which the Department of Biotechnology and Biophysics was provided with additional information by the authors, regarding the design and operation of a LLSM. However, to benefit from technology advancements and to optimize the system for *d*STORM, several modifications to the system were made. This includes different lasers, a different spatial light modulator (SLM), different piezo actuators and a different main camera. In the following, I will describe the optical path in more detail.

Four vertically polarized lasers (488 nm, 300 mW optically pumped semiconductor laser; 532 nm, 500 mW diode pumped solid state laser; 561 nm, 500 mW diode pumped solid state laser; 647 nm, 2000 mW fiber laser) are filtered with clean-up filters and individually expanded to an $1/e^2$ diameter of 2.5 mm by a Keplerian telescope. The lasers are mounted such that their polarization is perpendicular to the optical table. Subsequently, the beams are combined onto one axis with LaserMUX long-pass dichroids and the polarization is rotated by a half wave plate (HWP) to match the input polarization of a acousto optical tunable filter (AOTF). With the AOTF, individual laser lines are triggered and a transmission percentage is chosen, while the individual lasers are running continuously at constant power. For a rendering of the laser combiner module, see Figure A.3 in the appendix.

The output beam from the AOTF then enters the main LLSM system as schematically depicted in Figure 3.1. A first flip mirror enables choosing between a rudi-

mentary epi illumination (grey) for quickly finding the sample and the main lattice light-sheet beam path (red).

In the epi illumination beam path, the beam is widened by another Keplerian telescope and focused to the BFP of the epi objective (Olympus 40x/0.8), resulting in a parallel light column illuminating the sample through a window in the sample chamber. Fluorescent light (dark red) is collected and focused on a camera, after separating it from the illumination light with a 90:10 beam splitter. For a rendering of the sample chamber together with the sample holder and the three objectives, see Figure A.2 in the appendix.

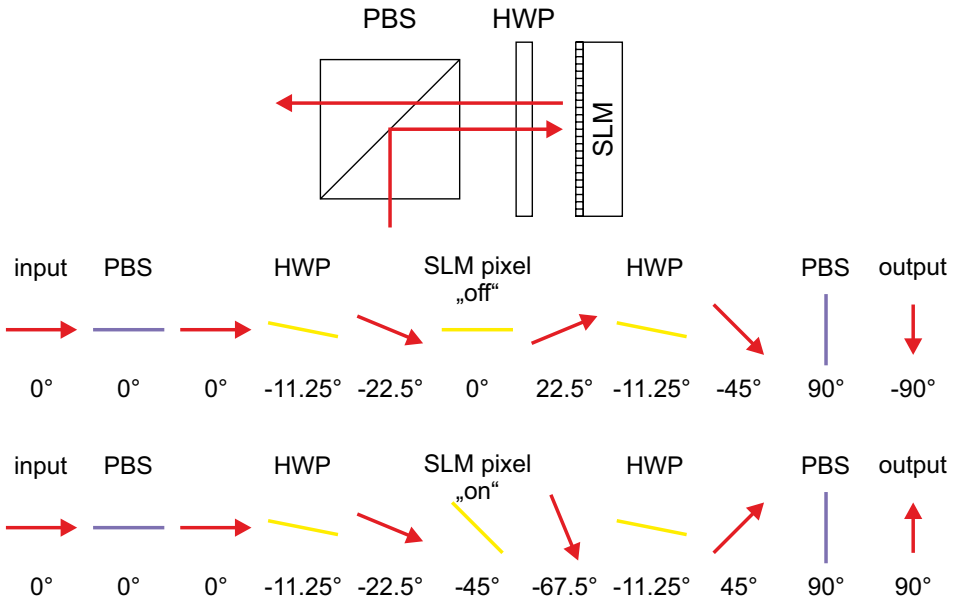

Figure 3.2.: Beam shaping using a reflective phase-only SLM. Shown are the optical schematics of the relevant parts and the electrical field for a beam that comes in, is reflected by the SLM and then transmitted through the polarizing beam splitter. The two cases for an active and inactive SLM pixel are indicated, where the SLM acts as a HWP with 0° or −45°, respectively.

Continuing on the main light-sheet illumination path, the input beam is widened in x and shrunk in z to illuminate a thin strip on the reflective, binary phase-only spatial light modulator (SLM). Here, the coordinate system I am referring to is depicted in Figure 3.3. The SLM consists of 2048 x 1536 pixels, each acting as a switchable half wave plate where the fast axis rotates by 45° between on and

off pixels. Together with the half wave plate and the polarizing beam splitter, it forms a pattern generation unit that outputs exactly opposite polarizations for on and off pixels of the SLM. Nevertheless, half of the intensity is lost in the process (Figure 3.2). The Fraunhofer diffraction pattern of the SLM is then imaged onto a etched mask, containing annuli of different diameter and width. By selecting a specific annulus, the maximum length of the beam and its confinement in z are chosen (cf. chapter 2.5.1).

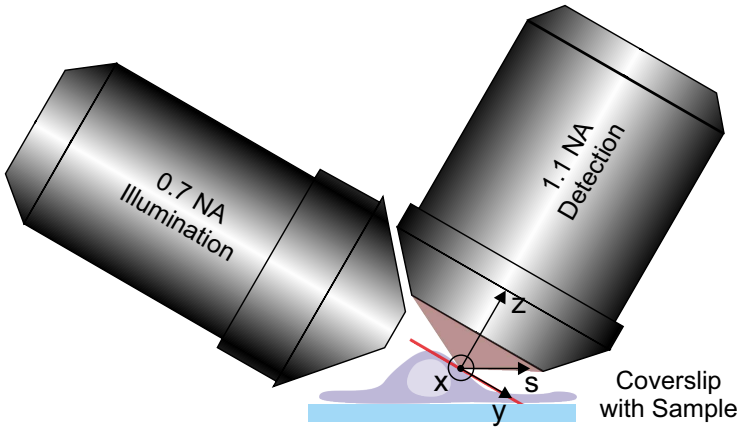

Figure 3.3.: Coordinate system of the LLSM. The lattice light-sheet (red) propagates along y and is confined in z, while it expands in x and is also dithered in x. The orthogonally mounted detection objective collects fluorescent light (maroon) along the z axis and can also be scanned in this direction, while its image plane is coinciding with the light-sheet. In sample scanning mode, the sample is scanned horizontally along s, while light-sheet and detection objective are stationary in z.

For conventional fluorescence light-sheet microscopy, the second set of cylindrical lenses, contracting the beam in z, doesn't have to be used. This greatly alleviates optical alignment tolerances, since the illumination is then much wider than the pattern displayed on the SLM. However, this also decreases power throughput dramatically. For this reason, the second set of cylindrical lenses has to be used for SMLM applications, since high power throughput is absolutely crucial in this case. With the annulus, the 0^{th} and higher orders of diffraction from the SLM are also filtered from the illumination beam. The intensity distribution emerging from the annulus is then demagnified and imaged onto the first galvanometric scanning mirror that scans in z and relayed to the second scanning mirror that scans in

x. With another magnifying 4f-system, the annulus image is finally relayed to the BFP of the water-dipping illumination objective. In the Fourier plane of the latter 4f-system, an inspection camera is placed and 10 % of the light is uncoupled to it to observe the FFP intensity distribution. Furthermore, a flip mirror just before the illumination objective and two relay lenses allow for imaging the BFP intensity distribution. The illumination objective is optimized for a maximum possible illumination NA in conjunction with the off-the-shelf detection objective. Since the two scanning mirrors are conjugate to the BFP of the objective, they will allow for a lateral displacement of the beam in the x and z direction in the FFP. The calibrated overall magnification from the SLM to its filtered image at the FFP is 166.5, yielding a pixel size of 50.7 nm of the SLM in sample space.

The fluorescence light generated by the light-sheet illumination is collected by an orthogonally mounted high-NA water-dipping objective (Nikon 25x/1.1) whose focal plane is coincident with the light-sheet illumination. The light passes through a quad-band dichroid and matched detection filter and is then focused on a sCMOS camera (Hamamatsu Orca Flash 4.0 v3) by a 500 mm tube lens. The detection filters allow for either using 532 nm or 561 nm excitation together with the two other available laser lines. Additionally, there is a single-color detection filter available (cf. Table A.1). The calibrated magnification of the detection system is 62.6x, yielding a camera pixel size of 103.8 nm in sample space.

To realize the system, approximately 100 custom-designed parts had to be machined, most of them at the machine shop of the Department of Biotechnology and Biophysics. Tight tolerances make daily alignment necessary, for which the system has over 100 micrometer screws. For instance, the coincidence of the light-sheet with the detection focal plane is crucial for image quality, but is subject to drift and typically needs to be adjusted to an offset better than 300 nm.

3.2. Simulating Optical Lattices

Although the goal of this thesis is to combine *d*STORM with lattice light-sheet microscopy, performing "conventional" LLSM was also part of this thesis. To this end, I simulated various non-diffracting light-sheets to assess their performance for these tasks. The simulation of the optical lattice approach was done with a Matlab script provided by the authors of [Che+14; Leg+16], while I wrote a Python script

for the linear array of Bessel beams approach. Recently, a simulation tool for various light-sheets has also been published [AAM18]. In the following, I will show two common lattice light-sheets exemplary.

Figure 3.4 shows the process of creating a 2D bound optical lattice, optimized for almost isotropic resolution in conventional LLSM. We start out with the electrical field of an ideal 2D optical hexagonal lattice (real part shown in first panel). The best parameters of the initial lattice are found empirically [Che+14], but usually start out from an "educated guess" based on our knowledge from chapter 2.5.2. Here, we use a fundamental lattice with one primitive vector parallel to the x axis and the condition, that the plane waves constituting the optical lattice should lie on a cone corresponding to our chosen illumination NA, $\mathrm{NA}_{\mathrm{center}} = 0.46$. The real part of the electric field is depicted in the first panel. The second panel (top row, center) shows the bound lattice after applying a Gaussian bounding function of width a to it:

$$E_{\mathrm{bound}}(x, z) = \exp\left(-\frac{2z^2}{a^2}\right) \mathrm{Re}\left\{E_{\mathrm{ideal}}\right\} \tag{3.1}$$

Then, we have to convert this pattern to binary, since the SLM is only capable of intruducing binary phase shifts. This is done by choosing a threshold value to separate between two states, e.g. the "on" and "off" pixels of the SLM. Like the bounding function width, this directly influences the confinement of the light-sheet in z. Here, I have chosen $\varepsilon = 0.15$, such that the output polarization of the SLM will be

$$\varphi_{\mathrm{SLM}}(x, z) = \pi H\left[|E_{\mathrm{bound}}(x, z)| - \varepsilon\right] \tag{3.2}$$

where H is the Heaviside step function. This is plotted in the top right panel.

Theoretically, we could already apply this pattern to the SLM and use it to

Figure 3.4 (following page): Simulated process of generating a fundamental hexagonal, maximally symmetric composite bound lattice. This light-sheet is optimized for almost isotropic resolution in conventional LLSM, but will excite out-of-focus portions of the sample. For details see text.

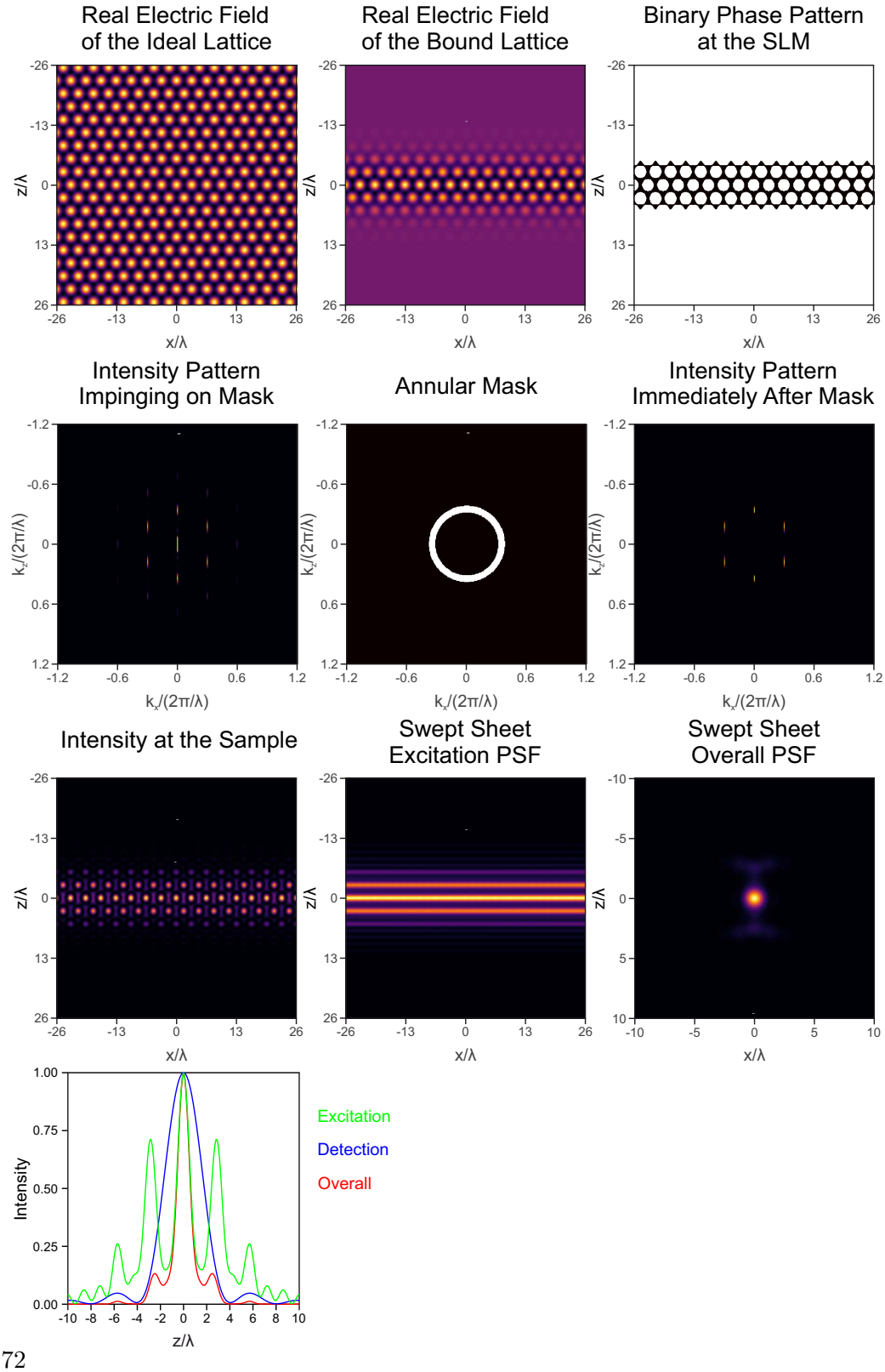
Real Electric Field of the Ideal Lattice
Real Electric Field of the Bound Lattice
Binary Phase Pattern at the SLM
Intensity Pattern Impinging on Mask
Annular Mask
Intensity Pattern Immediately After Mask
Intensity at the Sample
Swept Sheet Excitation PSF
Swept Sheet Overall PSF
z/λ
x/λ
k_z/(2π/λ)
k_x/(2π/λ)
Intensity
Excitation
Detection
Overall

generate a light-sheet right away. Here, I would like to show the simulated propagation through the system first. The SLM is situated in the FFP of a lens that has the annulus mask in its BFP. We know from Chapter 2.3.5, that we will get the Fourier transform of the electric field of the SLM at the annular mask. The intensity pattern impinging on the annular mask (4^{th} panel, 2^{nd} row, left) reads:

$$I_{\text{diff}}(k_x, k_z) = \left|\mathcal{F}\left\{\exp\left(i\varphi_{\text{SLM}}(x, z)\right)\right\}\right|^2 \tag{3.3}$$

Now, the field is filtered by an annulus (5^{th} and 6^{th} panel) that we chose to allow a minimum NA of 0.42 and a maximum NA of 0.50, giving a light-sheet of 15 µm non-diffracting beam length [Che+14]. The electric field at the BFP of the illumination objective will then be

$$E_{\text{BFP}}(k_x, k_z) = A(k_x, k_z)\,\mathcal{F}\left\{\exp\left(i\varphi_{\text{SLM}}(x, z)\right)\right\} \tag{3.4}$$

where

$$A(k_x, k_z) = H\left[\tau/2 - \left|\sqrt{k_x^2 + k_z^2} - \text{NA}_{\text{center}}\right|\right] \tag{3.5}$$

is the annulus filter function with width τ and central radius $\text{NA}_{\text{center}}$. Finally, the cross-sectional intensity of the light-sheet will again be the Fourier transform of the previous equation and is also called the excitation PSF:

$$\text{PSF}_{\text{exc}}(x, z) = \left|\mathcal{F}\left\{A(k_x, k_z)\ \left|\mathcal{F}\left\{\exp\left(i\varphi_{\text{SLM}}(x, z)\right)\right\}\right|\right\}\right|^2 \tag{3.6}$$

The excitation PSF is depicted in the 7^{th} panel. By integrating the intensity along x, a dithering of the light-sheet can be simulated (8^{th} panel).

By multiplying the excitation PSF with a simulated detection PSF, we get the overall system PSF, depicted in the 9^{th} panel (bottom right). The last panel shows the cross-section of excitation, detection and overall PSF and lets us appreciate the benefits of a fundamental hexagonal lattice for LLSM. The advantage of this lattice is, that the side lobes of the excitation are pushed further out in z and thereby are diminished by the detection PSF. This leaves only a very thin overall PSF that can give almost isotropic resolution in conventional LLSM. However, it is not suitable for SMLM or light-sensitive samples, since the excitation PSF contributes substantially

to out-of focus illumination. Moreover, the overall PSF is very sensible to an offset between light-sheet and detection PSF, demanding very precise alignment.

Without dithering the light-sheet, a highly structured illumination is created with the hexagonal lattice. In principle, this can be used to do structured illumination microscopy (SIM) [Che+14]. Even so, the beam propagates without diffraction along y, introducing no structured illumination in this direction. Therefore, a resolution enhancement can only be reached in x and z, somewhat defeating its purpose compared to other sophisticated 3D SIM implementations.

The second way to generate a lattice light-sheet is by constructing a coherent array of Bessel-Gauss beams, as discussed in Chapter 3.2 and depicted in Figure 3.5. We start out with a singe Bessel-Gauss beam that is generated by illuminating an annulus of finite width ($\mathrm{NA}_{\mathrm{min}} = 0.42$, $\mathrm{NA}_{\mathrm{maxn}} = 0.50$ as in the previous example) in the BFP of the excitation objective (left panels). Calculating the Fourier transform will give us the electric field of the light-sheet

$$E_{\mathrm{exc}}(x, z) = \mathcal{F}\{A(kx, k_z)\} \tag{3.7}$$

which is depicted in the 2$^{\mathrm{nd}}$ column. Integrating its intensity along x will give us the final light-sheet excitation PSF (right panels, with cross section plotted).

To add two more beams at distance d to the center, we directly manipulate the angular spectrum in the BFP according to

$$A_{3\text{-beam}}(k_x, k_z) = A(k_x, k_z) + A(k_x, k_z)e^{ik_x d} + A(k_x, k_z)e^{-ik_x d} \tag{3.8}$$

which results in the fields depicted in the second row. At the minimum distance for constructive interference along the x axis (cf. equation (2.82)), we get a tightly packed pattern of Bessel beam maxima along the x axis, while the beams interfere destructively in the z direction, resulting in a very thin light-sheet that is confined to the detection depth of field. This light-sheet can also be generated starting from a fundamental bound square lattice and following the first approach, hence I will use the term “square lattice” interchangeably.

Since this lattice light-sheet is very well confined to the detection depth of field, it is optimal for single molecule localization microscopy. It will deliver virtually all the excitation power to the volume of the sample that can be localized at the

same time, fulfilling the conditions that I theoretically outlined in Chapter 2.5. Experimental realizations of different optical lattices will be shown in Chapter 4.1.

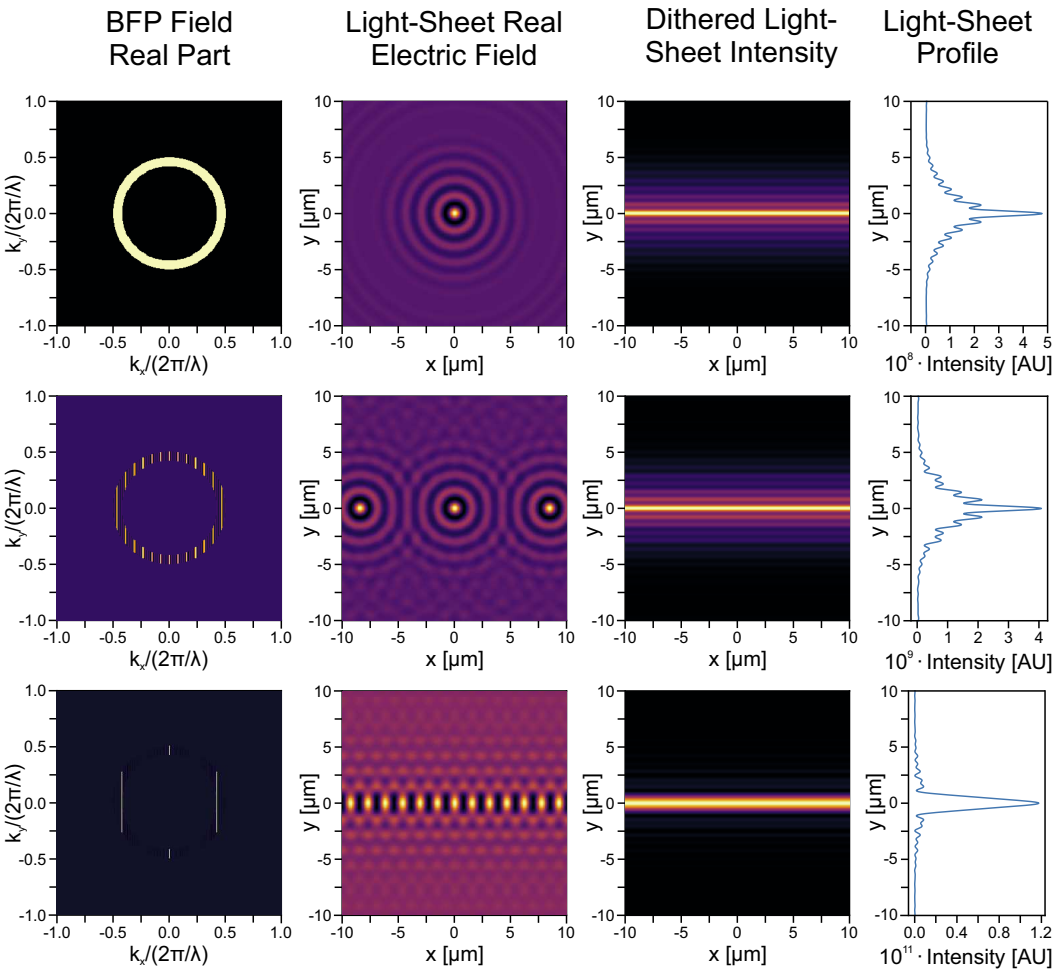

Figure 3.5.: Generation of a lattice light-sheet using a linear array of Bessel beams. The distance between the beam centers are infinite (top row), 8.4 µm (middle row), $d_{\text{constr,min}} = 1.54$ µm (bottom row).

3.3. Acquisition Modes and Data Processing Pipelines

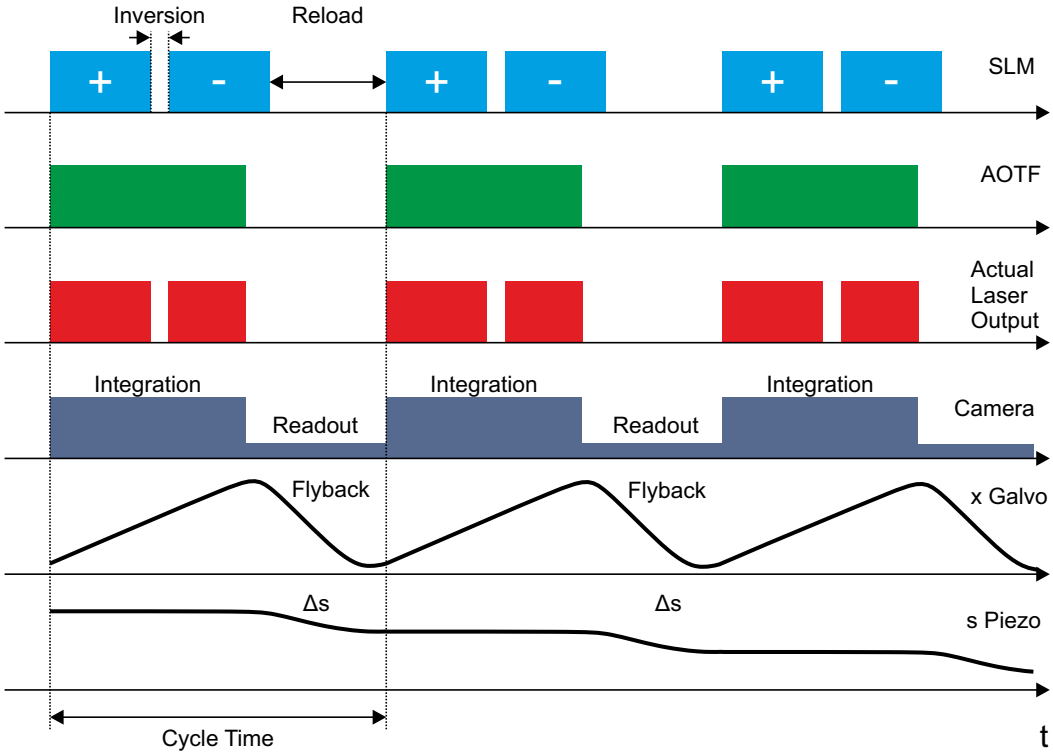

Figure 3.6.: Timing schematics of the LLSM components in single-color image acquisition with a dithered light-sheet in s-stack mode. For details, see text. Time axis is not to scale.

Before I go into detail about different acquisition modes for high-speed LLSM and lattice light-sheet illuminated *d*STORM, I need to introduce the basic boundary conditions that the synchronization of the different components of the LLSM requires (Figure 3.6).

The first component to consider is the SLM and the constraints it imposes on the timing. As a ferroelectric SLM, it has to balance the charge accumulation in its pixels over time, which means that each imaging cycle consists of displaying the desired pattern, inverting it, displaying the inverted pattern for the same time (which will produce the same intensity distribution at the sample) and finally reloading the whole cycle. The inversion time of the SLM is 56.6 µs and the reload time

is 276.16 µs. The overall cycle time of the SLM can only be programmed to be multiples of 5 ms.

The second component is the AOTF. The AOTF will be programmed to output the desired percentage of laser power and will then be triggered via TTL signal. The overall trigger pulse width matches the camera integration time. However, the SLM is directly connected to the blanking trigger of the AOTF and will briefly blank it during its inversion.

The camera is running in synchronous readout trigger mode. This means that it will integrate indefinitely, until it receives a trigger pulse. Then it will begin readout with rolling shutter and start the next integration immediately. The readout time can be calculated from the image height and is typically in the order of 1 ms. To eliminate potential rolling shutter artifacts, the laser is shut off until all pixels have been read out. One has to keep in mind that the first frame of each image stack will naturally have accumulated excess noise, since the camera had been integrating for a longer time.

The x galvanometric mirror has to dither the light-sheet for each exposure. Its analog control voltage is generated by the computer's FPGA card and stepped down a factor of 10 by a scaling amplifier for even better precision. The galvo will start accelerating before the illumination is switched on to ensure it scans at constant velocity during the camera integration time. After that, it will quickly fly back to the original position during camera readout. The portions of the cycle time that are reserved for acceleration and flyback can be set in the control software and are one key parameter for optimizing the LLSM timing.

Finally, between each frame, the sample piezo has to be moved to a new position and settle there. This is also controlled via analog voltage from the FPGA card. Since the sample holder is rather light, the settle time of the piezo is in the order of 1 ms, matching the time of the camera readout. It is also possible to scan the detection objective with a piezo and move the light-sheet in with its z galvo simultaneously. However, since the detection objective is much heavier than the sample holder, settling at a new position is much slower. Therefore, objective scanning is only used for calibration and PSF acquisition purposes in this thesis.

The main timing parameter that has to be chosen in the control software for each measurement is the *integration time* of the camera. However, to ensure an optimal duty cycle, the *cycle time* needs to be slightly below a multiple of 5 ms to allow the

SLM to immediately start the next cycle after camera readout. To further optimize the duty cycle, acceleration and flyback times of the x galvo can be tweaked, but a linear motion within the camera integration window has to be ensured.

3.3.1. High-Speed Multi-Color Lattice Light-Sheet Microscopy

One of the big strengths of LLSM is its high *spatiotemporal* resolution. Meaning that it is able to collect fluorescence from a whole sample volume at very high speeds, while outputting fairly high resolution. The speed is mostly attributed to its fast sample scanning mode allowing to image a whole volume multiple times per second. Because the SNR of light-sheet illuminated images is often very good, the deconvolution techniques work quite well on them, yielding good resolution.

For multi-color imaging, the SLM has to display different patterns for each wavelength of illumination. Therefore, the SLM is preloaded with a repetitive sequence of images and then used as a master clock for synchronizing the other components. This ensures having the right pattern displayed for the specific wavelength that is currently imaged.

A typical workflow for multi-color high-speed LLSM would then be:

- Take an overview image and determine imaging parameters, such as desired volume size in x, y (camera coordinates) and s (distance of sample scanning), laser powers for sufficient SNR, desired time resolution.
- Decide on which light-sheet to use. Hexagonal maximally symmetric fundamental lattice for best z resolution, or Bessel beam array (square lattice) for least out-of-focus sample illumination and improved alignment stability?
- Apply settings and start recording on a fast SSD drive.
- Use deskewing and deconvolution software such as LLSpy with an experimentally acquired PSF from fluorescent beads to deconvolve the image and register color channels.

Of course, there are always trade-offs to be made. Here, the most important one is to balance the illumination power and the desired cycle time and hence imaging speed. Too much illumination power will prematurely bleach the sample or even cause photodamage, while too less will render the SNR insufficient for

deconvolution. This requires a priori knowledge about the speed of the dynamics that are to be imaged, which might be gained in several test runs.

3.3.2. Lattice Light-Sheet Illumination for *d*STORM

The requirements of *d*STORM on lattice light-sheet illumination are quiet different than those for conventional fluorescence imaging. For efficient photoswitching, we need suitable illumination intensities in the range of 1-50 $\mathrm{kW/cm^2}$ [van+11]. Furthermore, we need to continuously step through the image volume to efficiently drive the majority of molecules to the dark state and image only a small subset of molecules at any time. At the same time, at least 20'000 frame have to be recorded per diffraction limited volume (e.g. thickness of $\sim$ 1 µm) to yield a well reconstructed structure [van+11]. This often requires acquiring up to several million frames in total and overall acquisition times of several hours for one super-resolved volume.

While acquiring, we want to maximize the duty cycle of the camera, e.g. maximize the integration time with respect to the overall cycle time. In contrast to multi-color acquisitions, all components are triggered with the FGPA card as master. This ensures the fastest possible triggering. Furthermore, the acceleration and flyback times of the x galvo can be tweaked, while the camera integration time is set to the highest possible value to still archive a cycle time of multiples of 5 ms. This way, the integration time can be expanded to 18.7 ms for a 20 ms cycle time when recording a 256x512 $\mathrm{px^2}$ field of view on the camera. Here, one has to keep in mind that the downtime of 1.3 ms does not depend on the integration time. Therefore, a cycle time of 10 ms would have an integration time of 8.7 ms and as such a worse camera duty cycle.

Finally a typical *d*STORM data acquisition on the LLSM would include:

- Take an overview image of the desired volume and determine its volume dimensions.
- Set up a 3D stack along the s axis that covers this volume at $\Delta s = 40\,\mathrm{nm}$ steps using a dithered linear Bessel beam array for illumination.
- Run this stack in a loop and acquire images to a fast SSD with enough free space.

- Transfer the SSD to another computer to start processing, while the next measurement can be started.

3.3.3. Evaluating Volumetric SMLM Data

After data acquisition, possibly being in the terabyte range for a single cell, the challenge remains to adequately and timely process these data. I would like to give an overview of the data processing pipeline I developed to approach this task (Figure 3.7).

The first task after acquiring the data is to localize single emitters and save their metadata in a readily processable format. To this end, I used Thunderstorm to 3D-localize single molecules with a 2D Gaussian function and a least-squares estimator or a phasor based approach [Mar+17] to get a fast result, when time was critical. Generally, I used SMAP to fit a model-free experimental PSF with a maximum-likelihood estimator, after removing the pixel specific sCMOS offset. SMAP has been shown to perform very well compared to other localization algorithms [Sag+18] and runs reasonably fast on the GPU. By using a maximum-likelihood estimator that explicitly accounts for camera noise, the theoretical minimum localization precision can be reached [Smi+10; DSM17]. Either way, this first step is the computationally most expensive, but leaves us with only the table of localizations that is much smaller (typically in the single GB range) and can then be further processed.

The next step after localization is the deskewing of the data. Due to the fact that the sample is scanned horizontally along s (cf. Figure 3.3), but the detection plane is oriented oblique at an angle of $\alpha = 29.7°$ to the sx plane, the volumetric data appear skewed. More precisely, for every step of the sample Δs, we get an apparent shift of

$$\Delta x_{\text{cam}} = \Delta s \, \cos\alpha$$
$$\Delta z_{\text{cam}} = \Delta s \, \sin\alpha$$

where the x axis of the final camera image is aligned along the y axis of the LLSM system. To deskew the data, the known offsets in x and z can be subtracted from the 3D coordinates of the localization file.

After deskewing, common filter operations of SMLM data can be applied. This

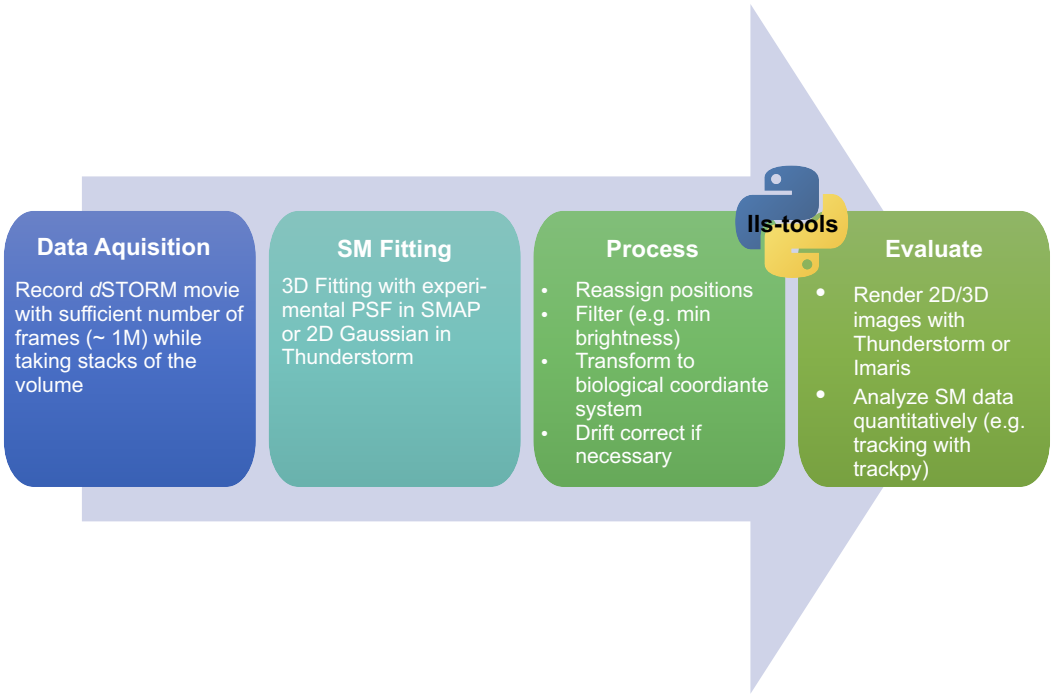

Figure 3.7.: Data processing pipeline for SMLM imaging on a lattice light-sheet microscope. After data acquisition and single molecule fitting, some of the key challenges still lie ahead. Processing and evaluating the SMLM data requires choosing adequate tools carefully to be able to process the data in a timely manner. For this purpose, I have developed a Python package to deal with this challenge.

can include applying a minimum intensity threshold to filter out dim events, that cannot be localized precisely or setting a maximum threshold to filter out events that are significantly brighter than a single fluorophore emission. Additionally, the data can be rotated to the "biological coordinate system", meaning that the cover slip forms the xy plane in the image volume. Finally, if sample drift was affecting the measurement, this can be corrected by using a drift correction implementation such as the one in Thunderstorm. Here, a cross-correlation between super-resolved images of subsets of localizations is calculated to measure the sample drift. The interpolated sample drift is then subtracted from the coordinates of each localization.

Finally, the data can be evaluated. On the one hand, this can be done qualitatively by rendering images and animations of the super-resolved structure with

Imaris or Thunderstorm. Often, this already helps answering a specific biological question a great deal. On the other hand, SMLM is unique among the super-resolution techniques with respect to its molecular statistical data that can further be exploited. In this thesis, single molecule tracking was carried out with localization data by further processing it with trackpy.

3.4. lls-tools, a Python package for LLSM data evaluation

As outlined in the previous chapter, there already exist many well-established software solutions for isolated steps of LLSM data evaluation. However, as each works on their own, they do not share a common data format or interface. Moreover, each of the hundreds to couple thousands of s stacks of localization images will result in individual localization files, making an automated processing indispensable. I tried to remedy these issues by developing a Python software package "lls-tools" that builds an interface between different established software solutions and is capable of fast batch processing. Thereby, the data evaluation process is sped up, without using too many resources to rewrite proven software solutions into the new software package. I made the software available to other users within our department via a Github repository.

The core of lls-tools is organizing the localization data into a Pandas DataFrame that allows for quick import and export to different formats used by third-party software, but also very fast computation on the data itself. Supported localization data formats include Thunderstorm, rapidSTORM, DAOSTORM, SMAP and ZOLA-3D, effectively building a bridge between these programs. That way it is possible to take advantage of the strengths of each software, e.g. fitting with SMAP, but using the Thunderstorm drift correction feature.

Specifically for LLSM localization data, lls-tools has functions to deskew the data and rotate it to the cover slip coordinates system. Furthermore, it can render 2D histograms of the data and extract statistical parameters and histograms of the individual localization properties. Filtering the data based on the localization parameters is also possible.

Finally, I also implemented a module that performs single molecule tracking. The

localization file serves as an input, allowing to use the superior localization precision of SMAP or other optimized algorithms. Then, the individual localizations are linked into particle tracks using trackpy, which implements the popular tracking algorithm developed by *Crocker* and *Grier* [CG96] in Python. Eventually, the mean square displacement of the particles can be calculated and plotted.

3.5. Third-Party Software

In the context of this thesis, the following third-party software was also used or tested for experimental calibration, alignment and data evaluation.

Lattice Light-Sheet Control Software This software is written in Labview by the authors of [Che+14; Leg+16] and facilitates the control of the LLSM. I modified its configuration to adapt to various new components on my LLSM implementation, including different piezos, a different SLM and a different main camera.

Lattice Light-Sheet Simulation Matlab Script The authors of [Che+14; Leg+16] provided a Matlab script to simulate the propagation of an optical lattice through the LLSM. This script was used to generate Figure 3.4.

LLSpy LLSpy [Lam18] is a Python software package that facilitates routine data processing tasks in conventional lattice light-sheet fluorescence microscopy, such as deskewing, deconvolution with a Richardson-Lucy implementation on the GPU, producing maximum intensity projections of the volumetric data, channel registration of multi-color data and compressing raw data.

FIJI FIJI [Sch+12] is based on ImageJ and is an open-source software collection for scientific image analysis, processing, scripting and simulation. It is the primary image processing software used throughout this thesis.

Thunderstorm Thunderstorm [Ove+14] is a single molecule localization plugin for FIJI, supporting various fitting models and estimators. I wrote several scripts to batch-process LLS localization data with to get a first overview of the results.

rapidSTORM rapidSTORM [Wol+12] is a very fast single molecule localization software written in C by Steve Wolter.

SMAP SMAP [Rie19] is a Matlab package distributed by the authors of [Li+17] that implements their 3D arbitrary PSF fitting with cSplines of single molecule data with a maximum-likelihood estimator, running on the GPU.

ZOLA-3D ZOLA-3D [Ari+18] is another 3D fitting algorithm that uses Zernicke coefficients to model the pupil field and runs as FIJI plugin on the GPU, albeit more tailored for more sophisticated PSF engineering approaches.

DAOSTORM / storm-analysis storm-analysis [Bab19] is a Python implementation of various fitting algorithms, including DAOSTORM [HUK11; BSZ12].

Trackpy Trackpy [All+16] is an open-source Python package used for single molecule tracking, implementing the popular algorithm by *Crocker* and *Grier* [CG96].

Imaris 8.4.1 Imaris is a 3D volume rendering software intended for microscopy data by Bitplane Inc.

HOKAWO 2.10 HOKAWO is the camera control software supplied by the manufacturer that was used to control the camera for calibration purposes and set its internal options that are not controlled via the LLSM Labview control software, such as water cooling.

Laser Control Softwares To control the four lasers of the LLSM, the software supplied by their manufacturers was used, namely "GUI-VFL V4.0.1" by MPB, "Remote App Laser Control V1.2" by Laser Quantum and "Sapphire Connection V1.0.1" by Coherent.

SLM Control Software During debugging and alignment, the SLM was directly controlled with the supplied software "MetroCon V3.2".

Corel Draw 2017 Software used to generate figures and drawings.

Origin 2018b Plotting and data analysis software used for creating plots and evaluation of data.

3.6. Sample Preparation

In this chapter, I will detail different sample preparation protocols that were used throughout this thesis.

3.6.1. Samples for Calibration and Performance Assessment

To calibrate various aspects of the LLSM, calibration samples are necessary. In general, it is very important to work with the exact same medium that will later be used for imaging, since the alignment of the light-sheet in the sample chamber is very sensitive to changes in refractive index of the medium.

The first calibration sample is a diluted solution of fluorescent dye, using the medium that is later used for imaging. A concentration of 0.1 nM is usually sufficient to view the light-sheet in the sample and align it to the focal plane of the detection objective.

Secondly, 100 nm TetraSpeck^{TM} fluorescent beads (T7279, Thermo Fisher) were extensively used for calibration and experimental PSF acquisition. Containing four different fluorophores in the visible spectrum, they can be used to acquire PSFs with all laser lines of the system. Briefly, to prepare cover slips with fluorescent beads, first clean the cover slips by incubating them in 1 M KOH for 20 min and washing them three times with millipore water. They can be stored in 100 % EtOH p.a.. Dilute the beads 1:1000 from the stock solution in phosphate buffered saline (PBS). Place individual, cleaned cover slips in a petri dish and apply 15 µL drops of the dilution to each of them. Incubate for 30 min and wash with millipore water.

3.6.2. Biological Samples

The sample shown in chapter 4.2 was stained as follows. First, HEK292T cells plated on 5 mm cover slips were fixed at 37 °C. To do this, they were washed with prewarmed PBS once and subsequently incubated with the fixation buffer 1, consisting of 0.3 % glutaraldehyde and 0.25 % Triton-X100 in cytoskeleton buffer, for 1-2 min. Cytoskeleton buffer consists of 10 mM MES at pH 6.1, 150 mM NaCl, 5 mM EGTA, 5mM glucose and 5 mM $MgCl_2$. Following, further fixation was employed by incubation with fixation buffer 2, consisting of 2 % glutaraldehyde in cytoskeleton buffer. Now, the sample was washed with PBS for 10 min and

subsequently incubated with 0.1 % $NaBH_4$ in PBS to reduce background. Before the staining process, the sample was again washed with PBS three times and incubated with 3 % BSA and 0.5 % Triton-X100 in PBS for 10 min to permeabilize and block it. Then, the primary mouse anti-β-tubulin antibody (Sigma Aldrich, diluted by 1:200 in 3 % BSA in PBS) was incubated for 1 h at 1:200 concentration in 3 % BSA in PBS. After washing six times with PBS, the secondary antibody was applied. Here, a goat anti-mouse IgG with Alexa Fluor 647 (Thermo Fisher) was incubated for 1 h. After another washing step (six times with PBS), the sample was incubated with 1 M SYTO 16 (Thermo Fisher) for 30 min in PBS to stain the nucleus. Following a washing step (three times with PBS), postfixation with 3 % formaldehyde was applied for 10 min. The sample was then washed with PBS three times and stored in 500 nM phalloidin-Atto-565 (Atto-Tec) in PBS over night to stain the actin skeleton. Before imaging, the sample was washed with PBS once.

For live-cell data presented in chapter 4.3, COS-7 cells were labeled with ER Tracker Red (E34250, Thermo Fisher) according to the manual of the dye, specifically the section for live cell labeling of adherent cells, and imaged immediately thereafter.

The sample presented in chapter 4.5.1 was labeled as described above for the sample presented in chapter 4.2, but without the SYTO 16 and phalloidin staining. The sample was then washed with PBS three times and stored in PBS until imaging.

For single molecule imaging with *d*STORM, "switching buffer" was prepared as follows. For 8.0 ml final volume, 6.84 ml PBS were mixed with 320 µl glucose (10 % w/v in PBS) and 800 µl β-mercaptoethylamine (1 M in PBS; prepared from M6500, Sigma). The pH was adjusted to 7.4 with ∼22 µl KOH 5 M. Finally, 40 µl glucose oxidase was added (10 U/ml in PBS; prepared from G2133, Sigma).

4 Lattice Light-Sheet Illumination as Key Enabler in Super-Resolution Microscopy

In this chapter, I present the results from different experiments that I conducted after building and calibrating the lattice light-sheet microscope. I will start out with determining the system characteristics by measuring its detection, excitation and overall PSF with different lattice light-sheets for illumination. By applying the system's potential to biological samples, I will then demonstrate the strengths of the system. In conventional fluorescence detection, these are especially the ability to acquire multi-color images from samples labeled with multiple dyes, the superior spatiotemporal resolution when it comes to observing fast dynamics in whole cells and the ability to image specimen for extended periods of time due to the system's low phototoxicity owed to its efficient excitation.

The main benefit and the ultimate purpose of this work however is to combine lattice light-sheet illumination with single molecule detection using *d*STORM. These data will be presented subsequently, showing 2D and 3D detection of single molecules. By using 3D detection and sample scanning, I was able to acquire single molecule localization data of the neural cell adhesion molecule (NCAM) on whole cells, pushing the limits of the understanding of its distribution. Then, I will also show single particle tracking data of the same receptor on living cells acquired with the LLSM, shedding light on its dynamics and interplay with the actin skeleton of the cell.

Some of the data shown here is currently in preparation for two manuscripts that are going to be submitted soon.

4.1. Light-Sheets for Conventional and Super-Resolution Microscopy

In the following, I am going to present different lattice light-sheets that I generated and used for further experiments. At the same time, I will show the impact of the excitation PSF of the dithered light-sheets on the overall PSF, making certain lattice light-sheets ideal for specific imaging needs. For all light-sheets, an annulus corresponding to a minimum NA of 0.42 and a maximum NA of 0.50 was used, as this generates a light-sheet of 15 µm usable length. This is best suited for single-layer cells, as were studied later on.

It should be pointed out that I have used the "Fire" lookup-table built into FIJI to colorize intensities in the images in this section, which perceptually amplifies weak signals to better show faint details of the PSFs. For the rest of this work, I used the perceptually uniform "Inferno" lookup-table as I did in the previous chapters.

Before analyzing different lattice light-sheets, we need to know the detection PSF of the LLSM system. To this end, I prepared 100 nm fluorescent Tetraspeck beads on a cover slip as described previously and illuminated them with a dithered light-sheet at 647 nm that was fixed in its z position. Then, I took a z stack by scanning the detection objective, resulting in the detection PSF, which is the same as for epi illumination. The resulting lateral (xy) and axial (yz) PSFs are shown in Figure 4.1 together with their cross-sectional profiles. A Gaussian fits well to the data and yields a full-width-half-maximum (FWHM) diameter of (417.1 ± 3.0) nm laterally and (1350 ± 15) nm axially for the 25x NA 1.10 detection objective together with the 500 mm tube lens.

At this point I have to mention that the system PSF in general can vary considerably, since the optics of the LLSM need to be aligned every day. Furthermore, even a slight change in refractive index of the medium has an impact on the position of the focal planes of both excitation and detection objectives, as well as on their optical performance, which makes correcting image aberrations necessary for each change in refractive index. Because of this, the PSFs shown here, measured in PBS at room temperature on the same day, can only be an example of typical system performance with these parameters after correction.

The spectrum of the red dye contained in the Tetraspeck beads is not disclosed by

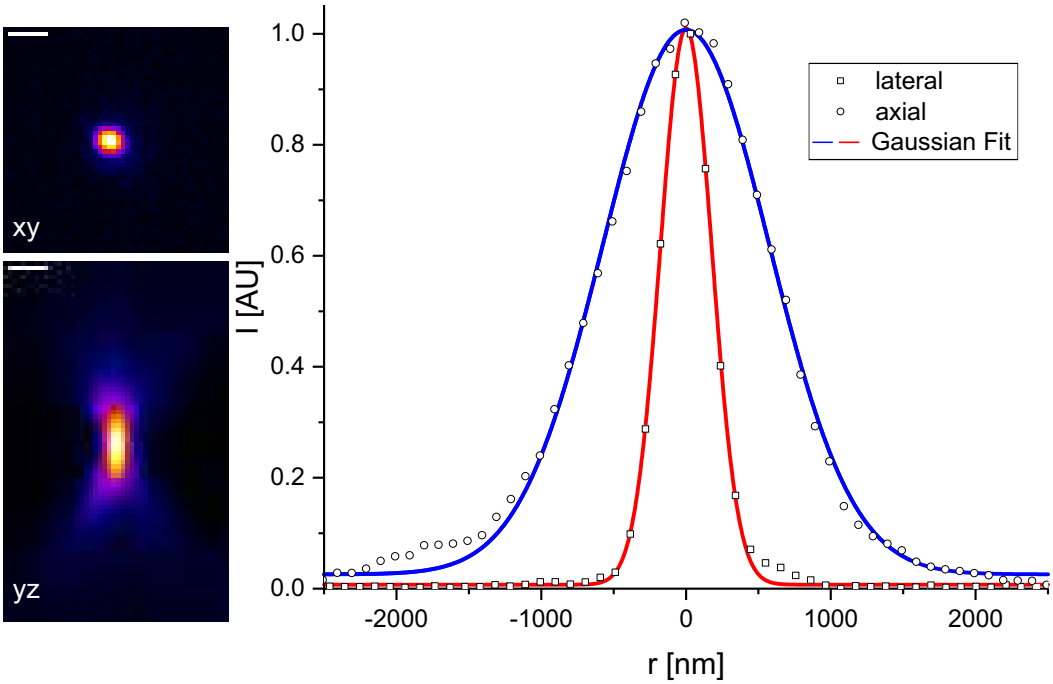

Figure 4.1.: Detection PSF of the LLSM system. To record this PSF, a 100 nm bead was illuminated with a dithered linear Bessel array light-sheet that was held fixed at the bead's z position, while the detection objective was scanned in z. Fitting the PSF with a Gaussian results in a FWHM of (417.1 ± 3.0) nm lateral and (1350 ± 15) nm axial with an illumination wavelength of 647 nm. Scalebars 1 µm.

the manufacturer, but assuming an emission wavelength of 660 nm, the theoretical lateral FWHM would be 366 nm according to the Gibson & Lanni PSF model [Kir+13]. Given the fact that the detection objective has a 2.0 mm working distance and we are using a standard achromatic lens instead of the specifically designed Nikon tube lens, this deviation of 14 % is quite reasonable and can be attributed to residual aberrations.

The first lattice light-sheet I would like to experimentally present here is the maximally symmetric fundamental hexagonal lattice, created with 647 nm light. In the top left of Figure 4.2, the light-sheet's excitation PSF is depicted. This was recorded by placing a fluorescent Tetraspeck Bead in the image plane of the detection objective and then stepping the lattice light-sheet in x and z with the galvo mirrors. The intensity of the bead minus the background is recorded and

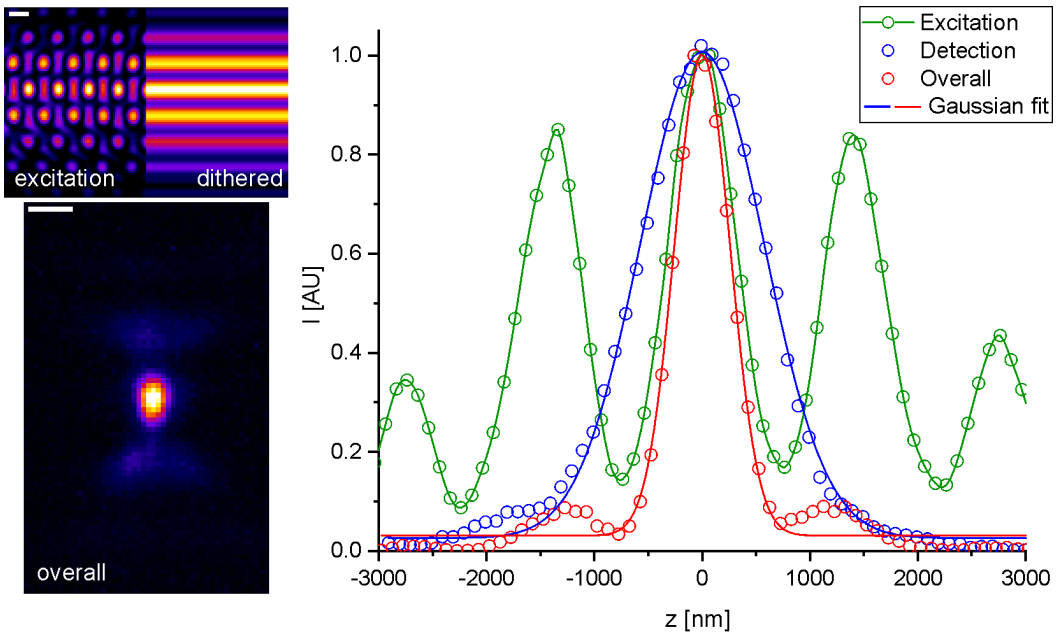

Figure 4.2.: Excitation and overall PSF for the hexagonal maximally symmetric fundamental lattice light-sheet at 647 nm excitation wavelength. The dithered light-sheet's axial profile is shown in green with lines to guide the eye. The overall PSF's axial profile is shown in red with a Gaussian fit resulting in a FWHM of (605 ± 12) nm, substantially improving z resolution. The blue curve shows the detection PSF from Figure 4.1. Scalebars 1 µm.

plotted as an image with horizontal axis x and vertical axis z. The excitation PSF nicely shows the hexagonal symmetry of confined excitation maxima as simulated in chapter 3.2.

Dithering the light-sheet in the x direction computationally by integrating the image along x gives the depicted dithered excitation PSF. The axial profiles along z of the dithered excitation and the detection PSF are shown in the diagram on the right in green and blue, respectively. The resulting overall PSF is measured by taking an image stack along z, with the ditherd lattice light-sheet following the focal plane of the detection objective. This results in the overall axial PSF depicted on the lower left. The profile is shown in red, with the axial FWHM now reduced to (605 ± 12) nm, the axial resolution is improved by more than a factor of 2, compared to the detection PSF alone, with the excellent sectioning capabilities of

the hexagonal lattice light-sheet. As can be seen from the profiles, the side lobes of the hexagonal lattice light-sheet have enough distance to the central excitation maximum to be diminished by the detection PSF, leaving only faint side lobes in the overall PSF.

However, from the axial profile in Figure 4.2, we can also appreciate that a slight misalignment between the detection focal plane and the light-sheet will quickly pull one of the side lobes of the excitation PSF in the detection PSF envelope, which would lead to a dramatically altered overall PSF. Especially when using deconvolution algorithms after a measurement, this can produce image artifacts. Thus, very good alignment is especially crucial when using the hexagonal lattice light-sheet. Moreover, it has to be noted that significant portions of the sample are illuminated that do not contribute to the image. This can be of special concern when trying to reduce photo-bleaching and phototoxic effects on living samples.

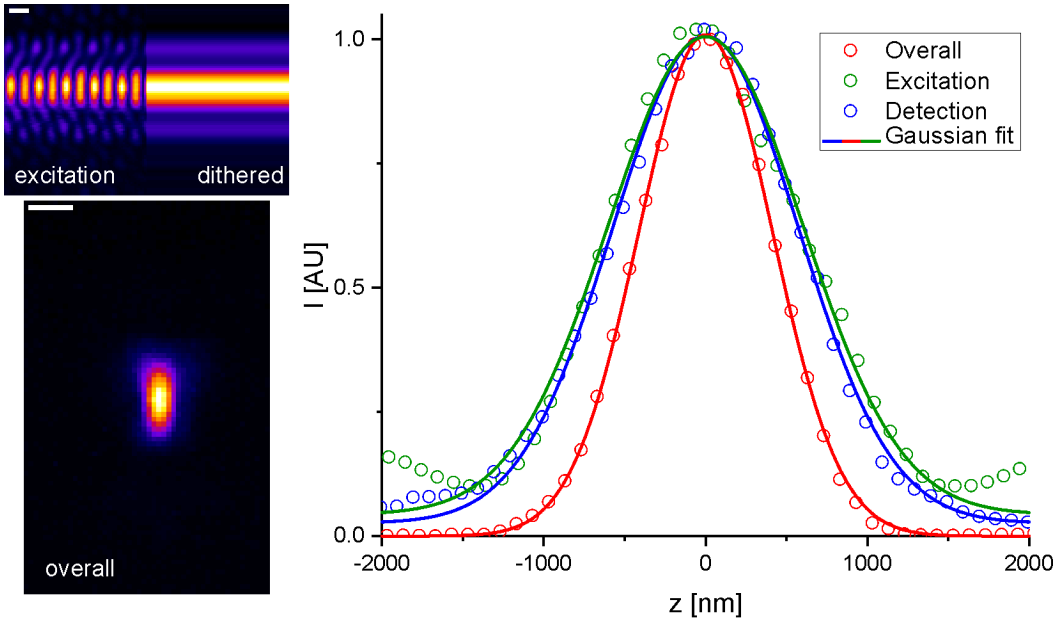

Figure 4.3.: Excitation and overall PSF for the linear Bessel array at minimal constructive interference spacing with 647 nm excitation wavelength. The profile of the dithered light-sheet is shown in green and the overall PSF's profile is shown in red. Blue denotes the detection PSF. All profiles have been fit with individual Gaussian functions, yielding an illumination FWHM of (1415 ± 31) nm and an overall PSF FWHM of (974.4 ± 5.5) nm. Scalebars 1 µm.

Secondly and most importantly, I would like to present the 647 nm linear Bessel beam array lattice light-sheet (Figure 4.3) with a spacing of 1.54 µm between individual beams, corresponding to the distance for constructive interference between beam side lobes along the x axis (cf. chapter 3.2). This square lattice light-sheet produces a dithered cross-section that is almost identical to the detection PSF, yielding an excitation FWHM of (1415 ± 31) nm with considerably diminished side lobes. The overall PSF has a FWHM of (974.4 ± 5.5) nm.

This nicely demonstrates the multiplication of excitation and detection PSF experimentally. In this case it is two Gaussian functions with approximately the same width being multiplied. Here, the result is another Gaussian function with a width reduced by $1/\sqrt{2}$ as expected.

More importantly, the confinement of the excitation light to the detection PSF was one of the goals of using lattice light-sheet microscopy in combination with *d*STORM in the first place. Only this guarantees that no molecules will be bleached prematurely before they are localized. Moreover, the illumination FWHM of roughly 1.4 µm is equal to the capture range of the astigmatic PSF shaping used for 3D localization. Other than that, this lattice light-sheet also greatly reduces phototoxic effects, since the overall illumination power needed to archive a specific SNR is greatly reduced by the fact that most of the illumination power is directed to the detection PSF with this light-sheet. These are the reasons why the square lattice light-sheet was used for all subsequent measurements presented here.

As an example of how the light-sheet scales with wavelength, Figure 4.4 shows the linear Bessel beam array for illumination with 488 nm, while the system was optimized and aligned for 647 nm excitation. Here, individual Bessel beams are spaced at 1.16 µm distance for constructive interference along x, owing to the shorter wavelength. The FWHM of the dithered lattice light-sheet is (967 ± 32) nm, scaling linearly with λ within the error margins. However, the detection PSF has an axial FWHM of (1600 ± 29) nm, being greater than the PSF for 647 nm excitation due to chromatic aberration. Nonetheless, the overall PSF is reduced to (723.9 ± 5.3) nm in z by the light-sheet.

This shows the fact that some chromatic aberration remains in the system, although all lenses used are achromatic. I could correct the chromatic aberration in the beam-shaping path further by tweaking the divergence of the 488 nm laser at its beam expander, resulting in a light-sheet thickness directly scaling with λ.

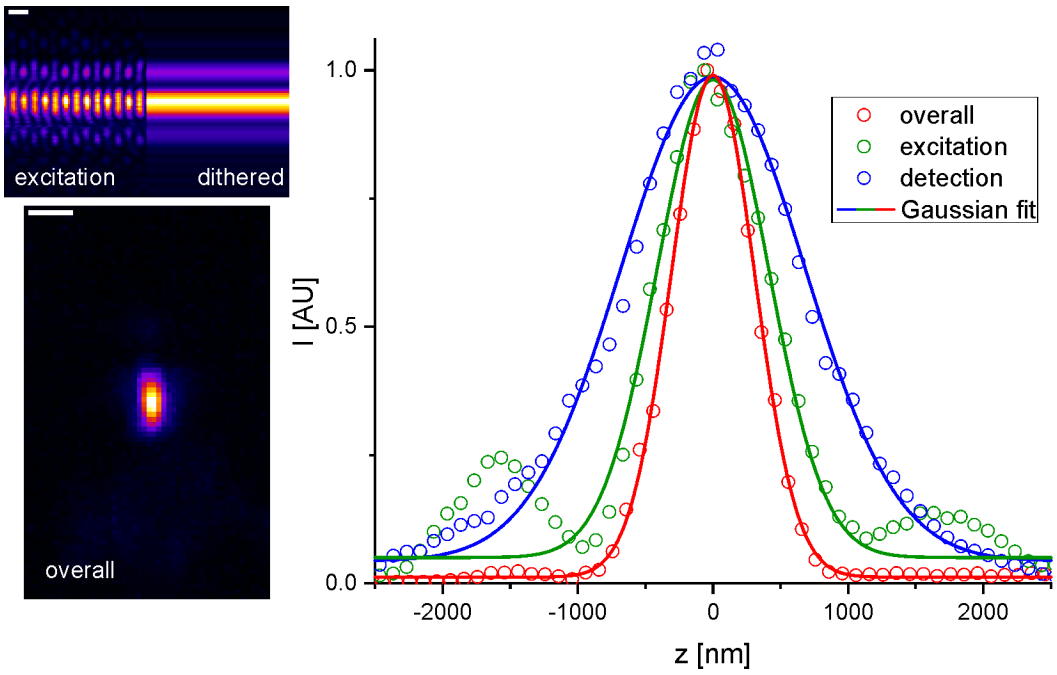

Figure 4.4.: Excitation and overall PSF for illumination with 488 nm and a linear Bessel array with minimal constructive interference spacing. Here, the LLSM was still optimized for the 647 nm channel, yielding a somewhat broader detection FWHM of (1600 ± 29) nm at 488 nm excitation (blue). The light-sheet itself has a width of (967 ± 32) nm (green), yielding an overall PSF FWHM of (723.9 ± 5.3) nm (red). Scalebars 1 µm.

However in the detection path, the remaining chromatic aberration cannot be corrected further, resulting in a disproportionate widening of the detection PSF. On the other hand, it also shows that specific alignment and calibration for a given wavelength can substantially improve system performance, but will lead to trade-offs for imaging at other wavelengths.

Another critical factor when thinking about SMLM measurements using a light-sheet is the power density that is available at the sample. To estimate this, I tracked the power loss at 647 nm through the system (Figure 4.5). Normalizing the power after the LaserMUX filters and before the AOTF to 100 %, we can follow the power loss through the system. First, the transmission through the AOTF in its "off" state is only 91 %, possibly due to back reflection. It will then output 87 % into its first diffraction order in its "on" state that is coupled into the LLSM. Further

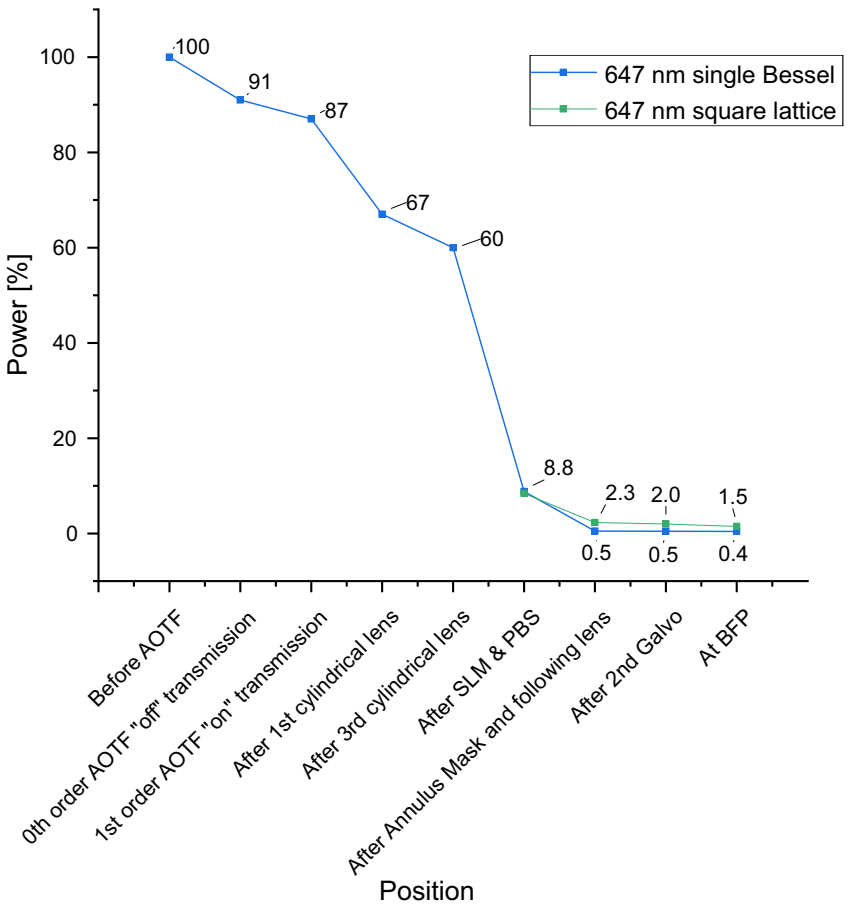

Figure 4.5.: Power loss along the beam path of the LLSM, tracked from shortly after the laser to the BFP of the illumination objective. For details see text.

back reflections on lenses and a slight overfilling of the first cylindrical lens further diminishes the power to 60 % before the SLM. After the SLM and the polarizing beam splitter, the power drops to 8.8 %, making it the single biggest power loss. This has several reasons. First, the maximum theoretical power throughput of the SLM and PBS is half of its input power (cf. chapter 3.1). And secondly, the pattern displayed on the SLM has to be overfilled by the beam to allow for alignment tolerances and a homogeneous illumination. Following the SLM, another great portion of the power is filtered out by the annulus mask. The mask will eliminate the 0^{th} and higher order diffraction patterns and will only let the 1^{st}

diffraction order pass. It is also evident, that the power transmission of one single Bessel beam is much worse than that of a square lattice. This is because the SLM is illuminated with a stripe, tailored to the square lattice pattern. Therefore, much less energy can be diffracted into the first diffraction order by the single Bessel beam pattern. After the annulus mask, only slight losses occur due to back reflections at the optics. Finally we get an overall transmission to the BFP of the excitation objective of 1.5 % for the square lattice and 0.4 % for the single Bessel beam.

To estimate the average intensity at the sample for the square lattice at maximum laser power, we consider its beam length of 15 µm as determined by the annulus width and consider a typical lateral width of 50 µm. The intensity can then be estimated to be

$$I = \frac{2000\ W \cdot 1.5\ \%}{15\,\mu\text{m} \cdot 50\,\mu\text{m}} = 4.0\,\frac{\text{kW}}{\text{cm}^2}\ . \tag{4.1}$$

This figure as well as the overall power loss is well in agreement with [Che+14]. The overall transmission is even improved by 15 %. However, the transmission of the overall system greatly depends on precise alignment, especially of the SLM diffraction pattern on the annulus mask. Therefore, the transmission can vary and has to be measured constantly.

4.2. 3-Color Volumetric Microscopy

One of the first measurements after building and calibrating the lattice light-sheet microscope concerned simultaneously imaging three different structures in a fixed biological sample. To do this, HEK293T cells were stained with SYTO 16 for the nucleus, Phalloidin-Atto-565 for the actin cytoskeleton and β-tubulin-Alexa-647 for the microtubules according to chapter 3.6.2.

To image these three dyes and discern them, the volume of 87.2 x 51.2 x 6.2 µm^3 was acquired in sample scan mode[1] and the excitation lasers were switched on consecutively in each plane, with the corresponding pattern displayed on the SLM (Figure 4.6). For theses dyes, the laser lines at 488 nm, 561 nm and 647 nm were used with a dithered maximally symmetric fundamental square lattice individually

[1] The dimensions stated are along the cover slip plane and perpendicular to the cover slip. See also x'/y'/z' axes in Figure 4.10.

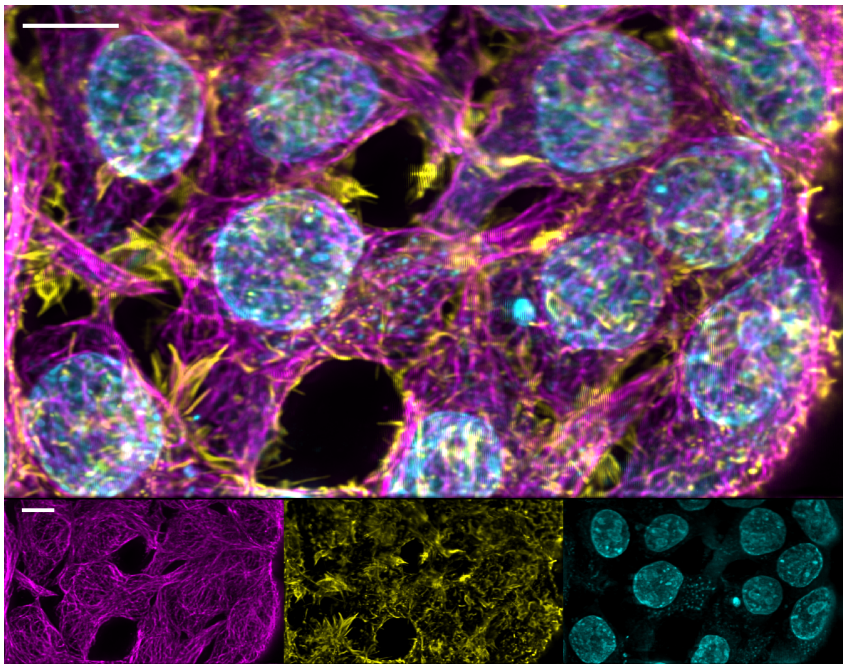

Figure 4.6.: Three color volumetric microscopy. HEK293T cells are stained with Syto16 (cyan), Phalloidin-Atto565 (yellow) and β-tubulin-Alexa647 (magenta), showing the nucleus, actin cytoskeleton and microtubules of the cells, respectively. A volume of 87.2 x 51.2 x 6.2 µm^3 was recorded with the three dyes selectively excited at 488 nm, 561 nm and 647 nm. The image shows the MIP of the whole deconvolved volume, with individual channels below. Scalebars 10 µm.

tailored to the wavelengths. Acquiring the volume took 60 s, with a cycle time of 25 ms per laser line per slice. A total of 801 slices in steps of 100 nm along s were collected.

In the LLSM, only a quad-band stop notch fluorescence filter is used in front of the main camera. Therefore, virtually any wavelength except for the excitation laser wavelengths will reach the camera and selective imaging of different fluorophores is only possible by separating them by their absorption spectra at the available laser lines. In this case, this worked quite well, as can be seen from the bottom row of Figure 4.6, showing virtually no cross-talk between the channels.

However, for dyes with a very broad absorption spectrum, such as for example BODIPY or some fluorescent proteins, a co-staining with other dyes is almost impossible to discern with the given set of fluorescence filters. Detecting dyes with

overlapping absorptions spectra would indeed require a second camera, separated by a dichroic beam splitter from the main camera. This would allow separating dyes based on their *emission spectra* instead. On other microscopes with a single camera, this is sometimes done by switching detection filters with an actuator between camera exposures. Nonetheless, this would hinder the acquisition speed of the LLSM dramatically. To this end, I have already prepared the detection path for a second camera and designed the required parts to mount it for future experiments. In the current state, careful consideration of appropriate dyes is important to avoid cross-talk between them.

4.3. Speed and Resolution: Live Cell ER Dynamics

As a good example for the great spatiotemporal resolution of the LLSM, I have imaged living COS-7 cells that I labeled with ER-Tracker Red (Thermo Fisher). The dye stains for the endoplasmic reticulum (ER) of the cell, an organelle consisting of a highly dynamic series of interconnected tubular and sheet-like structures, with tubule diameter between 60 nm and 100 nm [SVR06]. Its biological function spans from protein synthesis to hormone production and detoxification.

For imaging, the sample was submerged in the sample chamber filled with Hank's Balanced Salt Solution (HBSS) with calcium and magnesium that was kept at 37 °C by the heating system of the LLSM. The cellular volume of 50 x 80 x 10 µm^3 (x'/y'/z', cf. Figure 4.10) consisting of 201 slices in s direction was imaged at 1.0 s per volume in sample scanning mode with a dithered maximally symmetric fundamental square lattice light-sheet. Archiving this speed demanded a cycle time of 5 ms, leaving 4.25 ms for camera integration per cycle after tweaking the acquisition parameters. However, 5 mW input laser power at 561 nm were enough to get a fluorescence signal with decent SNR from the BODIPY TR dye used by ER-Tracker Red.

In fact, the SNR was sufficient to deconvolve the raw data (Figure 4.7 B) with an experimental PSF that was acquired beforehand under the same conditions. The deconvolved data (Figure 4.7 C) have much improved contrast compared to the raw data, without introducing deconvolution artifacts. All panels show maximum intensity projections (MIP) of the 3D volume that was acquired. Panels A-C and E show the projection along z into the xy plane, whereas side views projected along

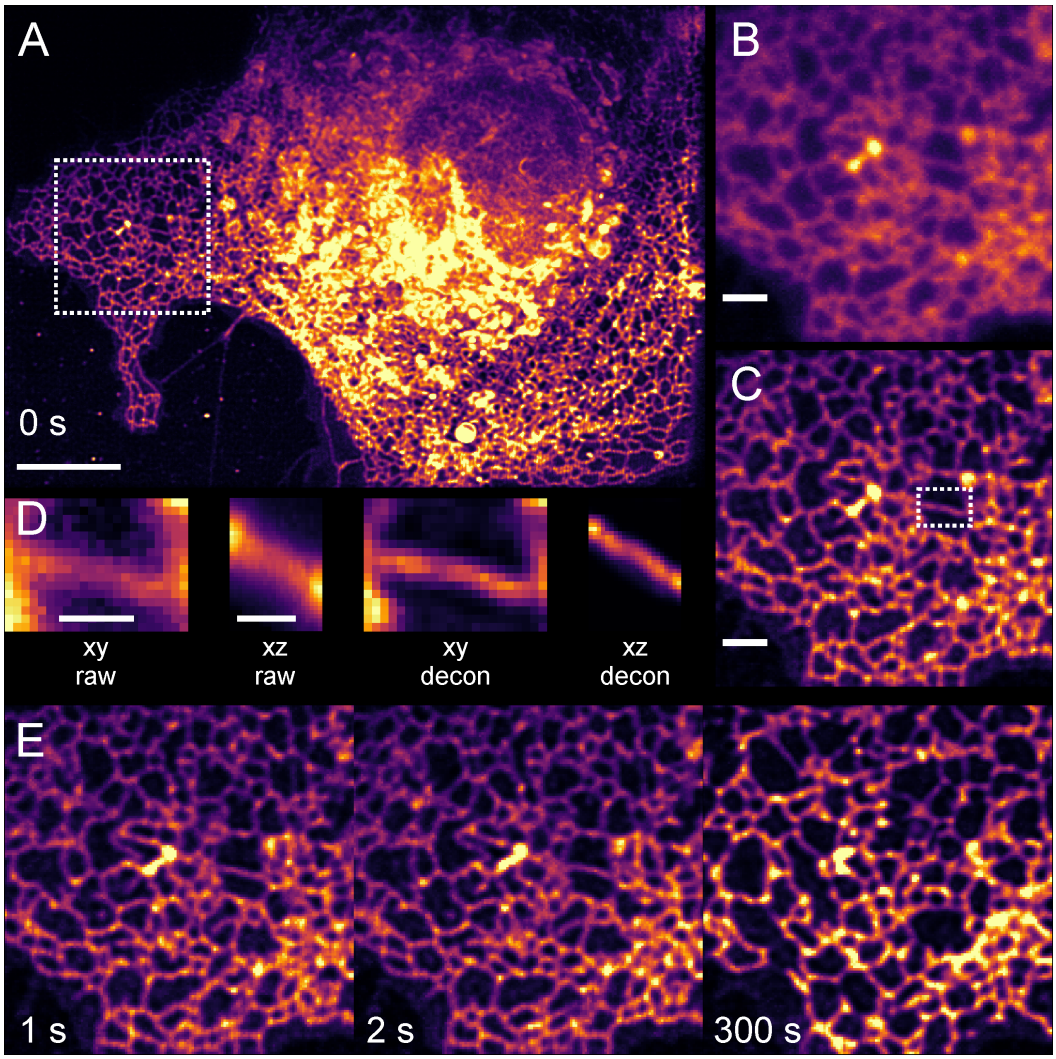

Figure 4.7.: A living COS-7 cell labeled with ER-Tracker Red, demonstrating the superior spatiotemporal resolution of the LLSM. (A) MIP of the whole deconvolved volume with a FOV of 80 x 50 μm^2 and an original height of the cell of 10 µm, demonstrating efficient labeling of the ER. (B) MIP of the raw data of the dashed box in (A). (C) MIP of the deconvolved data in the same region with an isolated tubule indicated (dashed). (D) Lateral and axial MIP of the isolated tubule of the raw data and deconvolved data. (E) Excerpts from the time series recorded, showing the fast dynamics of the ER. Scale bars 10 µm in (A), 2 µm in (B-C) and 1 µm in (D).

y into the xz plane are presented in D.

In panel D, isolating a single tubule allows for estimating the image resolution, since the tubule diameter is well below the diffraction limit. For the raw data, the cross-section of the tubule can be fitted by a Gaussian with a FWHM of (404 ± 28) nm in the xy plane and (1109 ± 55) nm in the xz plane, which is in agreement with the resolution we would expect from bead measurements. The same tubule profile measured in the deconvolved data yields a FWHM of (280 ± 14) nm in the xy plane and (506 ± 19) nm in the xz plane. This demonstrates the great improvements that deconvolution can have on LLSM data, since deconvolution critically depends on good SNR to work properly without introducing artifacts.

In the bottom panel (Figure 4.7 E), excerpts from the time sequence that was recorded are shown at different points in time. Delicate movements of the tubules within 1 s are captured successfully while the whole cell was recorded for a total time of 300 s.

Of course, the acquisition time per volume directly scales with the volume size in s, since this dictates the number of slices that the volume is comprised of. For example when imaging smaller parts of a cell, the acquisition time can be brought down to 145 ms for a 53 x 13 x 4 μm^3 (x/y/s) volume (data not shown). This time resolution for volumetric data while benefiting from high resolution at the same time is very valuable to many biological questions involving dynamic processes.

4.4. Observing Living Cells for Extended Periods of Time

The efficiency of lattice light-sheet illumination when it comes to the ratio of the illuminated volume versus the detectable volume is outstanding. For this reason, LLSM is a valuable tool to observe living cells with minimal perturbation over extended periods of time. Moreover, using the 15 µm long dithered maximally symmetric fundamental square lattice light-sheet, the volume that can be recorded is essentially only limited by the width of the sheet and the travel range of the sample scanning piezo. For a mono-layer of cells, there is no need to expand the volume in z beyond the light-sheet length.

To demonstrate this, Figure 4.8 shows living HEK293T cells in a volume of

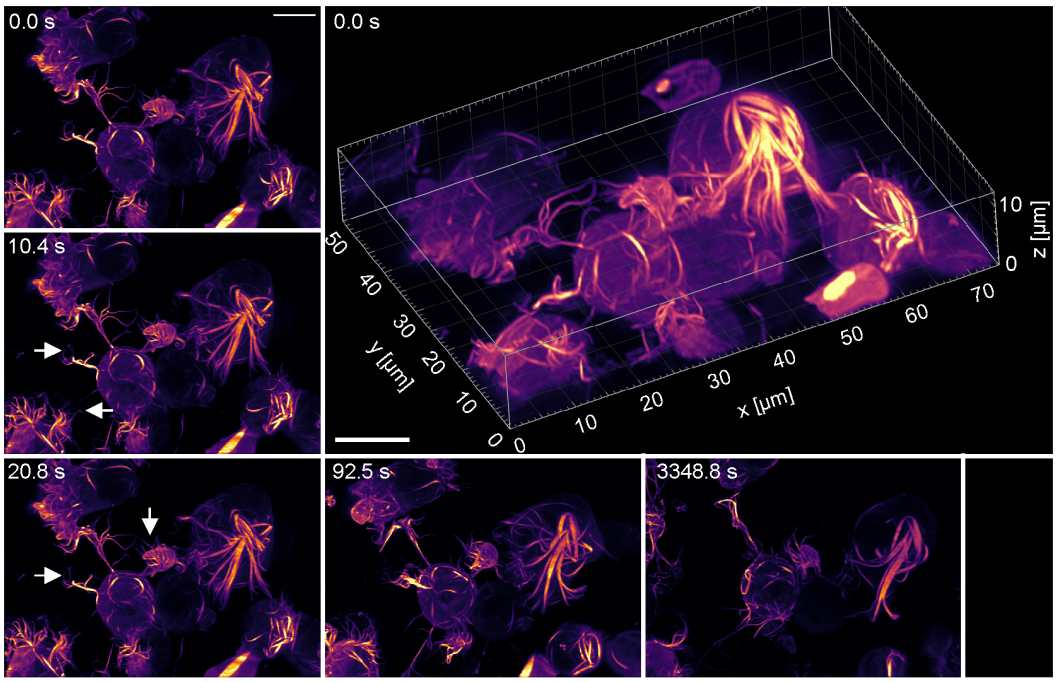

Figure 4.8.: Actin dynamics of HEK293T cells labeled with Lifeact-mScarlet and imaged on the LLSM. The volume was continuously imaged every 10.4 s for 56 min, showing no signs of reduced dynamics due to phototoxic effects. MIPs into the cover slip plane are shown at different points in time counter-clock-wise, with subtle changes in the actin dynamics highlighted by arrows. All MIPs are equally scaled to the same intensity. Scale bars 10 µm.

74.2 µm x 53.1 µm x 12.6 µm (x'/y'/z'), rotated to the cover slip plane and deconvolved with 20 iterations of the Richardson-Lucy algorithm implemented in LLSpy with a experimentally acquired PSF. The cells were provided and transfected with Lifeact-mScarlet by my colleague Jan Schlegel, leading to a very efficient expression of the fluorescent protein mScarlet at the actin cytoskeleton of the cells. As little as 2 mW input power at 561 nm to the LLSM was enough to get very strong signal at a camera integration time of 13.7 ms and a cycle time of 15 ms. For each volume, 361 slices at a distance of 250 nm were recorded in sample scanning mode, which equals 5.4 s acquisition time per volume. However, since the actin dynamics of the cells observed were not this fast, I added another 5 s break between acquiring each volume, leading to an overall repetition time of 10.4 s.

The cells shown in Figure 4.8 were imaged continuously at 37 °C for 3370 s (56.2 min). During this time, no signs of photodamage, such as a change in morphology or reduced actin dynamics, could be observed. Instead, subtle movements are visible at 10.4 s time steps (arrows). A slight fading of the fluorescence signal is visible after 3348.8 s, however the SNR in the image is still high enough to easily correct for the bleaching by using the histogram matching method implemented in FIJI for example (data not shown).

This demonstrates the great compatibility of the LLSM with living cells, especially for the efficient maximally symmetric fundamental square lattice, that avoids unnecessary phototoxic effects by only illuminating the detection volume.

4.5. *d*STORM in a Lattice Light-Sheet

In this section, I will show 2D and 3D single molecule data acquired on the LLSM with *d*STORM. Naturally, since acquiring single molecule localization data requires recording many images over extended periods of time, this is only really suited for chemically fixed samples. Here, *d*STORM is able to provide information approaching molecular resolution and use the localization data further to gain quantitative information. My main project here was the investigation of the spatial distribution and dynamics of the neural cell adhesion molecule (NCAM), also known as CD56.

The main challenge of doing *d*STORM in a lattice light-sheet microscope is that the photon budget is limited. That is because the maximum number of photons from a single fluorophore (assuming free rotation) that can be collected directly scales with the opening angle of the detection objective. Or more precisely, with the solid angle that is covered by it, $\Omega = 2\pi\,(1 - \cos\alpha)$, where α is the opening angle of the objective. The solid angle of the LLSM detection objective is 0.89π, whereas it is 1.60π for a typical stand-alone SMLM setup with an oil immersion objective (assuming $n = 1.52$ and NA $= 1.49$). This means a 44 % reduction in the photon counts one can expect, without taking the scattering and absorption in the medium along the 2.0 mm working distance of the objective into account. Hence, to get good single molecule localization data, making sure the system is perfectly aligned is crucial to prevent any further photon losses. Typically, this requires alignment and calibration before every measurement.

4.5.1. Stationary 2D *d*STORM

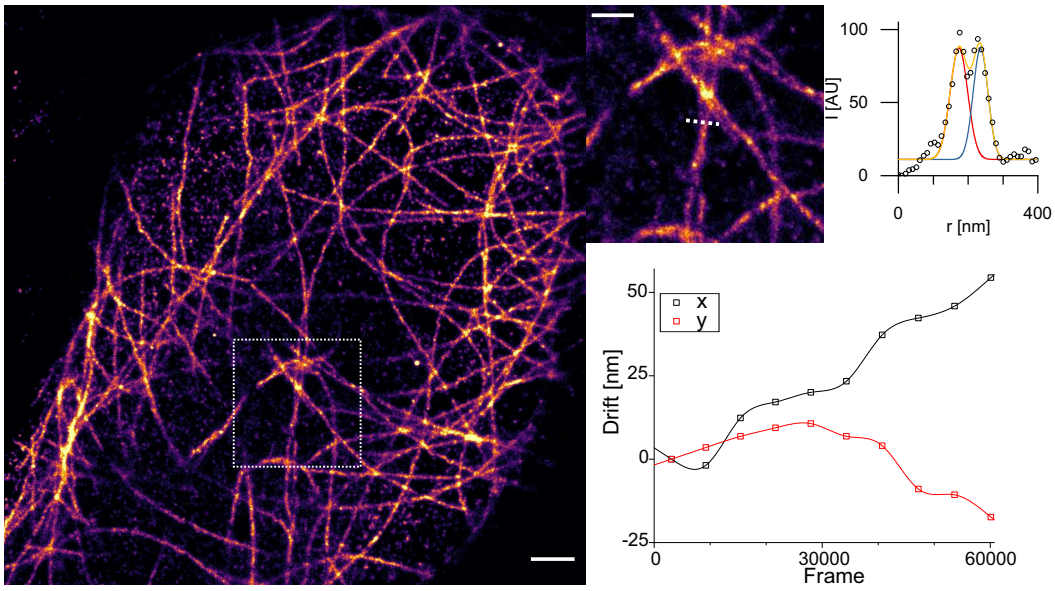

Figure 4.9.: 2D *d*STORM measurement of microtubules in a U2OS cell labeled with Alexa Fluor 647. The dashed region is shown magnified in the second image. (upper right) Along the dashed line, the profile was taken and fitted with two Gaussian functions. (lower right) The maximum drift that the sample experiences was below 52 nm. Scalebars 1 µm (left) and 500 nm (upper right).

A classic example that is often used for routine performance assessment of both the imaging system and labeling strategies is imaging the microtubule structure of cells. Here, HEK293T cells stained with Alexa Fluor 647 against microtubules (with primary and secondary antibody, see chapter 3.6.2 for details) were imaged. I measured them in the standard single molecule switching buffer (see chapter 3.6.2) at a cycle time of 10 ms and illumination with the dithered square lattice light-sheet at 3.3 kW/cm^2. For this measurement, the cylindrical lens was not incorporated into the detection beam path to allow for a 2D standard localization detection in a fixed plane of the specimen without any PSF engineering.

Figure 4.9 shows the reconstructed image from 60'000 recorded frames. The data was localized using SMAP, rotated, filtered and transformed to Thunderstorm format with lls-tools and finally drift-corrected and rendered with Thunderstorm. The sectioning by the light-sheet is quite apparent, with individual microtubules

fading in and out of the volume that is observed. Drawing a line profile over two entangled microtubules and fitting the profile with two Gaussian functions yields a diameter of (50.3 ± 5.4) nm and (59.2 ± 6.5) nm for the two tubules and a peak to peak distance of (62.0 ± 4.3) nm. This measure can well serve as an upper limit of the image resolution that can at least be reached with the system, as the distance between the tubules is well resolvable.

Figure 4.9 also shows the drift that occurred during the measurement and that was corrected for with the drift-correction algorithm implemented in Thunderstorm. Here, the localizations from subsets of 6000 frames are cross-correlated with each other to measure the sample drift (data points). Then, the drift between the data points is interpolated (solid lines). The sample drifted less than 52 nm for the entire measurement of 60'000 frames. This can be considered relatively stable and more importantly, easy to correct for with the Thunderstorm cross-correlation implementation.

The diameter of the microtubules matches well with the previously published data of 25 nm diameter [Coo00], if one takes the size of the antibodies used for staining into account which is approximately 10 nm per antibody [Ret13].

4.5.2. Volumetric 3D *d*STORM of Membrane Receptors

The neural cell adhesion molecule (NCAM), also known as CD56, is an important pathogen recognition receptor on human natural killer (NK) cells [Zie+17] and plays a key role in fundamental biological processes such as cell-cell adhesion, learning and memory.

To investigate the spatial distribution of the CD56 receptor on the plasma membrane, HEK293T cells were labeled with Alexa Fluor 647 primary antibodies and prepared on poly-D-lysine coated cover slips by Jan Schlegel. After calibrating the system for the refractive index of *d*STORM switching buffer, I imaged the total volume of 53.1 µm x 26.6 µm x 40.0 µm (x/y/s) which corresponds to a volume of 47.5 µm x 52.5 µm x 11.7 µm (x'/y'/z') after deskewing and rotating to the cover slip coordinate system, with the z axis orthogonal to the cover slip. The volume was imaged with continuously looping sample scanning stacks at a slice distance of 40 nm and an illumination intensity of 3.6 $\mathrm{kW/cm^2}$. Single molecules were continuously localized in 3D by using astigmatic PSF shaping in the detection path

and fitted with a spline-interpolated experimental PSF model that was acquired beforehand using SMAP.

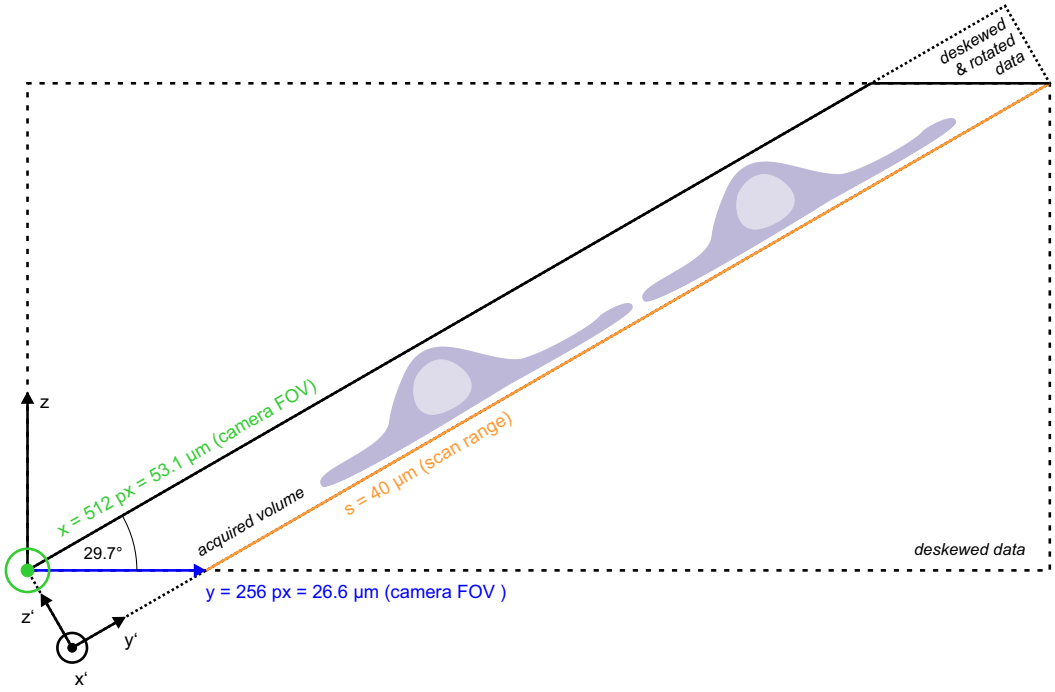

Figure 4.10.: Coordinate transformation of LLSM data, exemplary shown for the data in Figure 4.11. Since the original data (solid lines) is acquired by scanning along s at an oblique angle of 29.7° to the camera plane xy, the data has to be deskewed, resulting in a rectangular 3D image stack that is padded with empty pixels (dashed line). Rotating the data around the x axis results in an rectangular image stack along the x'/y'/z' coordinate system, with the cover slip conveniently in the x'y' plane (dotted line).

With a cycle time of 20 ms and a camera integration time of 18.7 ms, collecting 573 stacks with 1001 slices per stack took 3.2 hours. In the image data, 3.2×10^6 localizations were detected of which 0.7×10^6 were situated outside the 1.4 µm range illuminated by the dithered maximally symmetric fundamental square lattice light-sheet or filtered with a minimum photon threshold and discarded. The sample scanning motion was then accounted for and the volume was rotated to the cover slip plane with lls-tools. The reconstructed super-resolved volume is shown in Figure 4.11 (A) as a maximum intensity projection. Four cells are visible in the

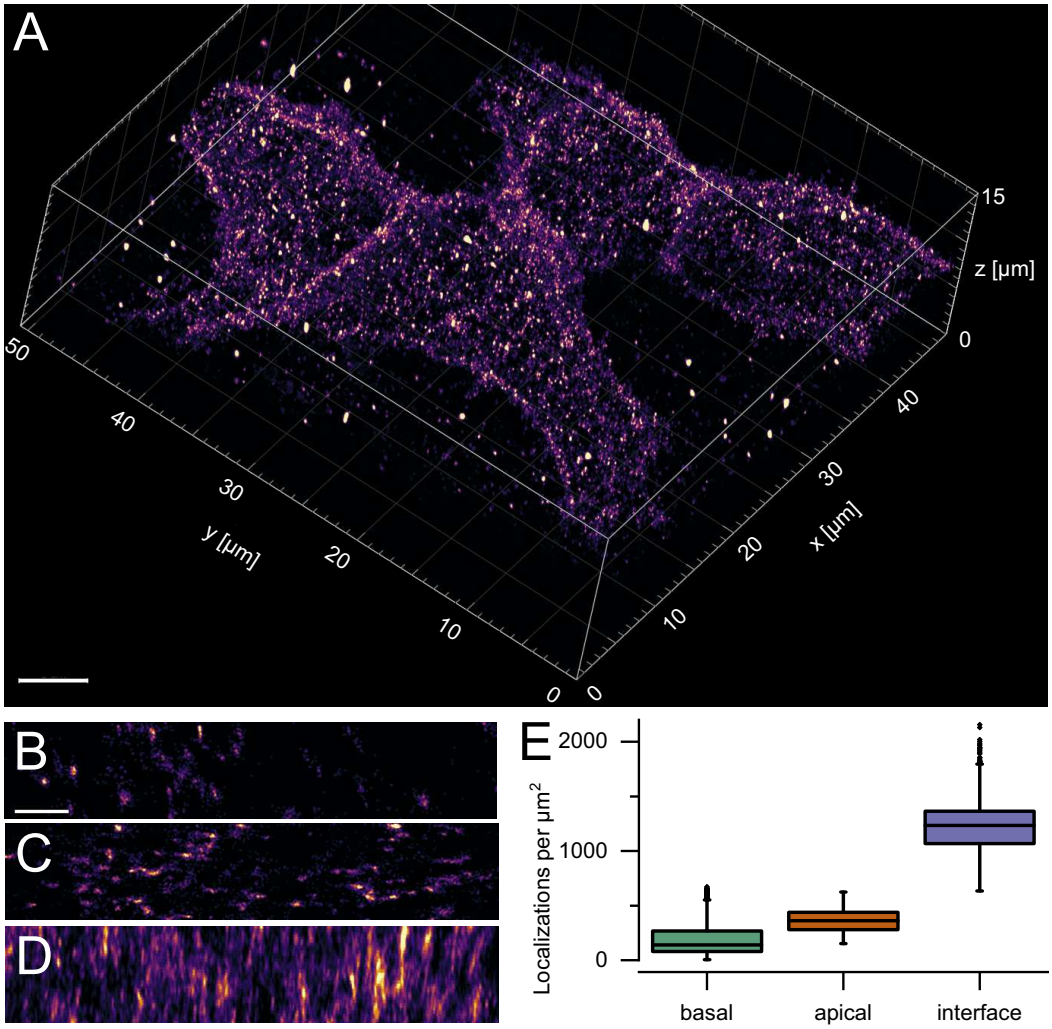

Figure 4.11.: 3D *d*STORM data of the CD56 receptor acquired with the LLSM. (A) MIP of the acquired volume, showing four cells with signal accumulation at the cell-to-cell interfaces. (B-C) Close-up projections of the apical and basal membranes parallel to the cover slip. (E) Close-up projection perpendicular to the cover slip plane of an interface membrane. (E) Quantitative analysis of the localization densities reveals significant differences between the basal, apical and interface membranes. Scale bars 5 µm (A), 1 µm (B-D).

volume and an accumulation of signal at cell-to-cell interfaces is already visible in the MIP.

To investigate the receptor density differences further, I calculated the density of localizations on the apical, basal and interface membranes with a sliding window analysis I implemented in FIJI. First, the localization data was projected to 2D, perpendicular to the respective membrane. Then, a square window with a width of 2 µm was used to calculate the density and subsequently moved in 200 nm steps to sample the whole region of interest. The resulting distribution is shown in (B) as box plots. This quantification yields densities of (139 ± 76) µm^{-2} for the basal, (361 ± 79) µm^{-2} for the apical and (1234 ± 146) µm^{-2} for the interface membrane (median ± MAD). Exemplary zoomed in views from the three investigated membrane sections are shown in (B-D).

Interestingly, the basal membrane exhibits significantly lower densities than the apical membrane, presumably due to antibody accessibility constraints at the cover slip. Strikingly, the density at the interface is more than twice as dense as the apical density, quantitatively showing the accumulation at the interface. Using the Mann-Whitney test to compare the apical density versus half the interface density results in a p value of < 0.001 for the null hypothesis of equal distributions.

To get an estimate of the localization precision of the overall image acquisition, I tracked single molecules within the data that were present for at least seven consecutive frames using the Kalman filter implementation in rapidSTORM. For all tracks, I calculated the deviation of the molecule's position from the mean position of the track with an algorithm I implemented in Python. The deviations of all such molecules are shown as histogram in Figure 4.12 (data points). Fitting these data with Gaussian distributions yields a standard deviation of 15.8 nm in x, 16.6 nm in y and 73.8 nm in z. Measuring the standard deviations along the rotated coordinate system perpendicular to the cover slip plane yields precisions of 14.2 nm in x', 20.1 nm in y' and 37.5 nm in z'. Here, the data was also rotated around y by 3.0° to compensate for the slightly tilted cover slip in the sample holder. A great benefit of this measure of localization error is that it includes all experimental conditions, such as sample scanning or residual aberrations. Therefore it can be considered more realistic than the often employed calculation of a theoretical localization precision solely based on the photon count of the emitters.

The significantly increased density of receptors at the cell-to-cell interface is un-

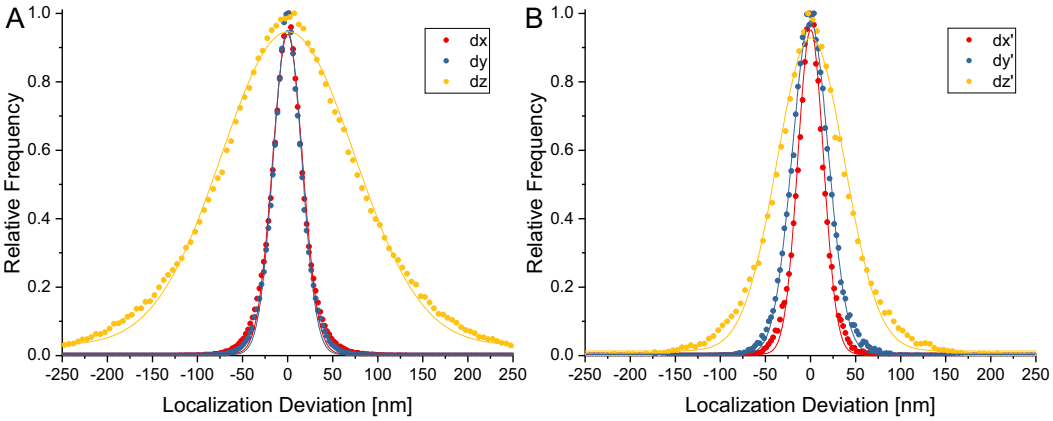

Figure 4.12.: Estimation of the localization precision for the dataset shown in Figure 4.11. Single molecule localizations were linked into tracks using the Kalman filter implemented in rapidSTORM. Subsequently, for molecules present in at least 7 consecutive frames, the deviation of the localizations from the mean coordinate of their track was calculated and is shown as histogram here (data points). The distributions are fit with Gaussian functions, yielding standard deviations of 15.8 nm in x, 16.6 nm in y and 73.8 nm in z for the original data coordiante system (A) and 20.1 nm in x', 14.2 nm in y' and 37.5 nm in z' for the data set after rotating around x into the cover slip plane.

derpinned by the fact that CD56 has been shown to form *cis*-dimers in the plasma membrane that subsequently can form *trans*-dimers with receptors on opposing membranes [Kul+11]. Starting from freely diffusing receptors, it is conceivable that receptors accumulate at cell-to-cell interfaces upon *trans*-dimerization, effectively trapping them there.

Lattice light-sheet illumination is indispensable for this *d*STORM experiment, because it allows to assess receptor densities on the whole plasma membrane without perturbing dyes that are not imaged at the same time. Previously, single molecule data in combination with lattice light-sheet illumination was captured using PAINT [Leg+16]. However, allowing the free dye to diffuse through the cell and bind to a target before it is bleached required very slow imaging, resulting in acquisition times of several days. Moreover, the continuously accumulating dye molecules resulted in a nonlinear swelling of the sample, making complex correction necessary.

4.6. Receptor Tracking in 3D

In addition to gaining insights into the density of CD56 on the plasma membrane of HEK293T cells, investigating its dynamics in living cells is sensible to complete the understanding of this important receptor. To this end, live HEK293T cells were labeled with primary SeTau-647 antibodies by Jan Schlegel and subsequently imaged at the LLSM in Fluorobrite (Thermo Fisher) buffer at 37 °C. The recently developed SeTau-647 dye was specifically used here since it has been reported to be very photostable, allowing long time traces of individual molecules [Tsu+18].

To trace individual receptor *cis*-dimers, I used a similar approach as for the localization data presented in chapter 4.5.2, but without sample scanning. Instead, I fixed the light-sheet in a plane intersecting the fluid-facing apical side of the plasma membrane. This enabled much higher frame rates for observing receptor dimers on the apical membrane, while the 3D astigmatic detection still allows to observe a volume thick enough to follow individual dimers along the curvature of the membrane.

For these experiments, the cycle time was set to 20 ms to capture fast dynamics, while still keeping the illumination intensity low at 0.11 kW/cm^2 with the dithered square lattice light-sheet. Single particles were then localized in 3D with SMAP as for the *d*STORM data. The resulting localization file was processed with lls-tools to link individual localizations into tracks and calculate the mean square displacement (MSD) of the molecules.

Figure 4.13 shows the dynamic data obtained from CD56 receptors on HEK293T cells in the presence of 170 µM actin inhibitor CK-666 (Sigma, #SML0006) in the imaging medium and 1 % DMSO as control. Four each buffer condition, seven different volumes at different positions were imaged. Panel (A) shows the tracks of CD56 dimers from one measurement exemplary, while panel (B) shows the 3D path of the same receptors. The MSD of all receptor dimers was calculated and plotted (C) and subsequently averaged for each measurement (ensemble average). The ensemble average can be fit with a power law:

$$\mathrm{MSD}(\tau) = \alpha\,\tau^n \tag{4.2}$$

Where α is the generalized diffusion constant and n is the anomalous diffusion

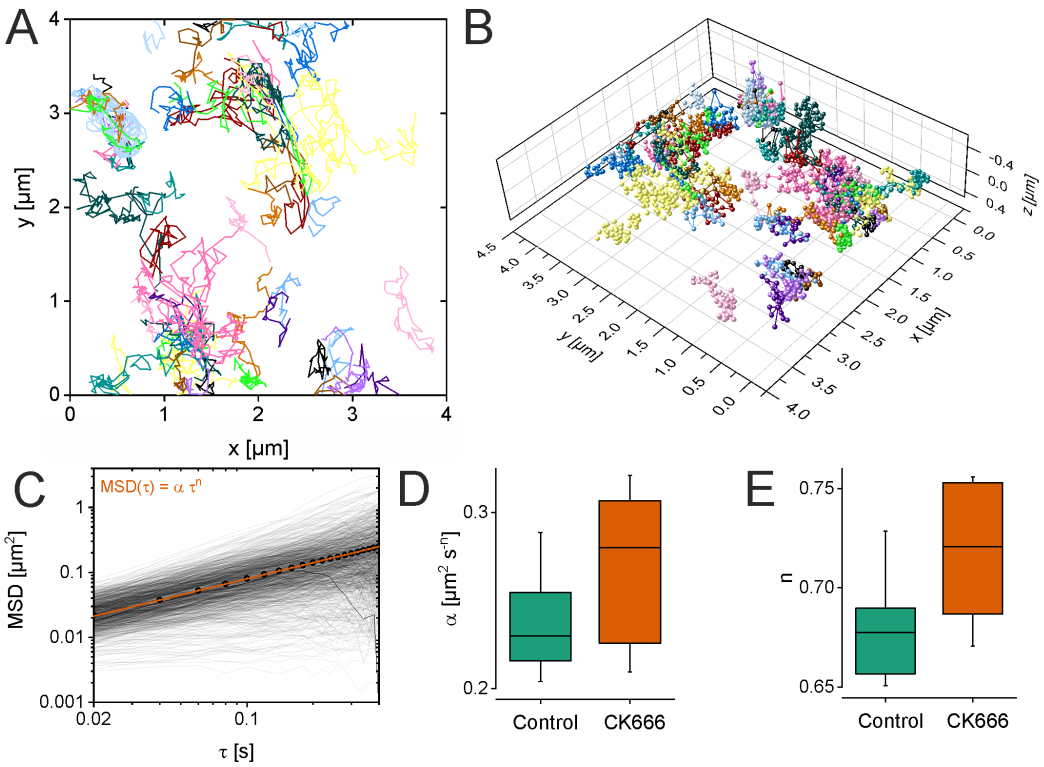

Figure 4.13.: Single particle tracking of CD56 receptors on the plasma membrane of HEK293T cells. (A) Individual, color-coded tracks of receptors on the membrane, projected to the xy plane. (B) Same data, showing the 3D extent of the receptor diffusion. (C) The MSDs of individual receptors (gray lines) can be ensemble-averaged (black dots) and fit by a power law (orange line). (D) Treating the cells with CK-666 increases the generalized diffusion constant α. (E) The anomalous diffusion coefficient n increases significantly with the CK-666 treatment.

exponent [MG15]. The distribution of the ensemble MSD coefficients are shown as box plots in (D-E).

The resulting anomalous diffusion exponent significantly ($p < 0.05$) increases from $n = (0.678 \pm 0.012)$ to $n = (0.721 \pm 0.032)$ upon addition of CK-666 (mean $\pm$ SE). This brings the anomalous diffusion coefficient closer to unhindered Brownian motion at $n = 1$. The generalized diffusion constant also increases from $\alpha = (0.230 \pm 0.019)$ µm^{2}s^{-n} to $\alpha = (0.280 \pm 0.027)$ µm^{2}s^{-n}, although not statistically significant ($p > 0.05$). P values were calculated using a two sided t test.

These data show that the mobility of CD56 on the plasma membrane is influenced by the actin skeleton dynamics of the cell. Specifically, we can conclude that the CD56 mobility is affected by Arp2/3 complex dependent actin nucleation and assembly that is suppressed by the cell-permeable CK-666 inhibitor in our experiments. These results hint that actin plays an important role in the dynamics of CD56 to fulfill its biological role as adhesion receptor and can be connected with previous experiments showing that CD56 translocation to the NK-fungal interaction site is dependent on actin re-arrangements [Zie+17].

For these experiments, lattice light-sheet illumination uniquely empowers the observation of CD56 receptors on the apical plasma membrane far away from the cover slip, with minimal illumination intensity and illumination volume, therefore no impact on the cell health and dynamics of the receptor can be expected.

5 Conclusion & Outlook

Most single molecule localization microscopy (SMLM) experiments to date have been performed in two dimensions and near the cover slip. For many questions, this is sufficient and provides detailed images of cellular structures. In fact, even though SMLM is hardly a decade old and still under heavy development as a method, it is already widely adapted as an important tool in biology, pharmaceutics and medicine [SH17]. However, the demand for volumetric imaging has been constantly growing. Just like multi-color imaging can provide *structural context*, volumetric imaging provides much needed *spatial context* for many biological questions and allows for imaging big volumes with the same parameters at once. The field of physics fruitfully interfaces here with biology by developing new optical approaches to target specific questions and improve the answers to long-posed ones.

In this thesis, I have optimized the design of the lattice light-sheet microscope and built it to combine its unique illumination strategy with 3D-*d*STORM for the first time, enabling single-molecule localization in whole cells. This allows for perturbation-free imaging and localizing single molecules in three dimensions in whole cells during a single measurement, because only those dyes are illuminated that are detectable at the same time. SMLM measurements are no longer confined to the cover slip and can provide new insights, since quantitative data can be compared across the whole volume, a feature that is unique to this technique.

By designing a maximally symmetric fundamental square optical lattice and simulating its properties, I could verify a suitable candidate light-sheet that restricts the illumination to the detectable volume and matches the 3D detection range of astigmatic PSF engineering. Measuring the detection, excitation and overall PSF for this light-sheet confirmed its suitability. At the same time, I could also show different excitation strategies, when restriction to the detection volume is not the primary concern.

Using the square lattice light-sheet, I could demonstrate the fruitful interaction

of lattice light-sheet illumination and *d*STORM imaging by imaging the distribution of CD56 receptors on the whole plasma membrane of HEK293T cells. The 3D localization data could further be used to derive quantitative data about the receptor density on the apical and basal membrane, as well as on the interface between individual cells. Compared to previous efforts using PAINT single molecule microscopy in combination with lattice light-sheet illumination [Leg+16], *d*STORM has the advantage of significantly shorter acquisition times and does not suffer from non-linear sample swelling during acquisition that required cumbersome corrections in the PAINT approach.

In living cells, I could use the LLSM to track CD56 receptors in 3D at 37 °C. The data show significant differences in the diffusion of the receptor on the plasma membrane of the cell, if the actin skeleton dynamics of the cell was suppressed by the CK-666 inhibitor. This indicates, that CD56 is interacting with the actin cytoskeleton to fulfill its biological role as adhesion receptor.

Many of these measurements routinely amount to ∼TByte of image data that needs to be processed on a daily basis. This in itself can be a major obstacle on the way to quantitative super-resolution data and demands efficient data handling and processing. To this end, I have developed a Python package with the aim of largely automating data processing and introducing a central data structure. Instead of re-implementing well-established algorithms in the package itself, I chose to focus on building a bridge between the various isolated software tools that already exist. To me, this appeared to be the most efficient way and granted me more time to use the LLSM on various interesting projects.

Some of these projects were also benefiting from the established diffraction-limited detection of the LLSM. Here, I could show several examples of the outstanding compatibility of lattice light-sheet illumination with living specimen and the great spatiotemporal resolution that can be achieved with the system. In fixed specimen, the LLSM can be used to image big volumes labeled with up to three different dyes without the effect of premature photobleaching. In living cells, I could measure the actin dynamics for extended periods of time without any change in morphology of the cells that would indicate photodamage or phototoxicity. To observe fast dynamics, the system is capable of capturing the volume of whole cells at 1 Hz and go down to 145 ms per volume for smaller acquisition volumes that allow imaging of subcellular compartments. In the conventional detection mode,

the superior signal-to-noise ratio due to lattice light-sheet illumination plays a key role in the applicability of deconvolution algorithms to further improve the contrast and resolution of the volumetric data.

Looking forward, there have been some recent developments in the field that I think will be relevant to this work to improve the method even more. Some of them might be worth considering in the near future.

First, a very intriguing preprint was published recently [Cha+18], that could help improve the power throughput of the LLSM system dramatically. This would allow higher excitation intensities, leading to faster photoswitching and therefore allowing shorter cycle times in *d*STORM measurements. This would eventually lead to faster volumetric *d*STORM acquisitions. In the preprint, the beam shaping with a SLM is completely omitted. Instead, the annulus mask is directly illuminated with the line-shaped laser focus formed by focusing with a cylindrical lens. Different lattices can then be created by illuminating different parts of the mask with a galvanometric scanning mirror during the camera integration time. The authors show theoretically and experimentally, that the averaged illumination field during the integration time is equal to that generated by a static SLM pattern. Since much of the excitation light is lost at the SLM, using this approach could dramatically increase the power throughput, making excitation with higher laser power densities at the sample feasible. In the preprint, a proof of concept was carried out with low-NA objectives. Implementing this on the high-NA LLSM system would certainly be one of the next steps and will significantly reduce the cost of further LLSM implementations as a byproduct.

For the diffraction-limited detection mode of the LLSM, I could already show the great improvements of deconvolution using the Richardson-Lucy algorithm. Recently, advances have been made to leverage machine-learning algorithms for content-aware image restoration [Wei+18]. Using these algorithms, the authors show remarkable results, pushing the limits of necessary SNR, exposure time and illumination intensity, while keeping the image quality constant. Applying the algorithm to LLSM data to further reduce illumination intensity or exposure time would be a logical next step.

By connecting the sample bath to a peristaltic pump, several interesting exper-

iments can be envisioned. One could for example start measuring living cells and keep monitoring them until a biological relevant event happens. At this point, the buffer can be exchanged with fixation buffer to freeze the sample in this state. Subsequently, one could label the cells and image them with *d*STORM. It could be even possible to do the *d*STORM labeling outside the microscope and put the sample back in afterwards, since the positioning of the sample holder is fairly reproducible.

To address the issue of incompatible multi-color staining when using dyes such as BODYPI or certain fluorescent proteins due to their broad absorption spectra (cf. chapter 4.2), a second camera could be fitted to the microscope. This would allow for discerning dyes based on their emission spectra. I already prepared the LLSM for a second camera and designed the necessary parts to mount it. Unfortunately, due to supply difficulties of the camera manufacturer, the second camera could not be acquired in time.

All in all, the LLSM platform is a very versatile tool that holds great potential and I hope it will continue helping to expand the limits of science and our understanding of biological processes.

A | Supplementary Figures and Tables

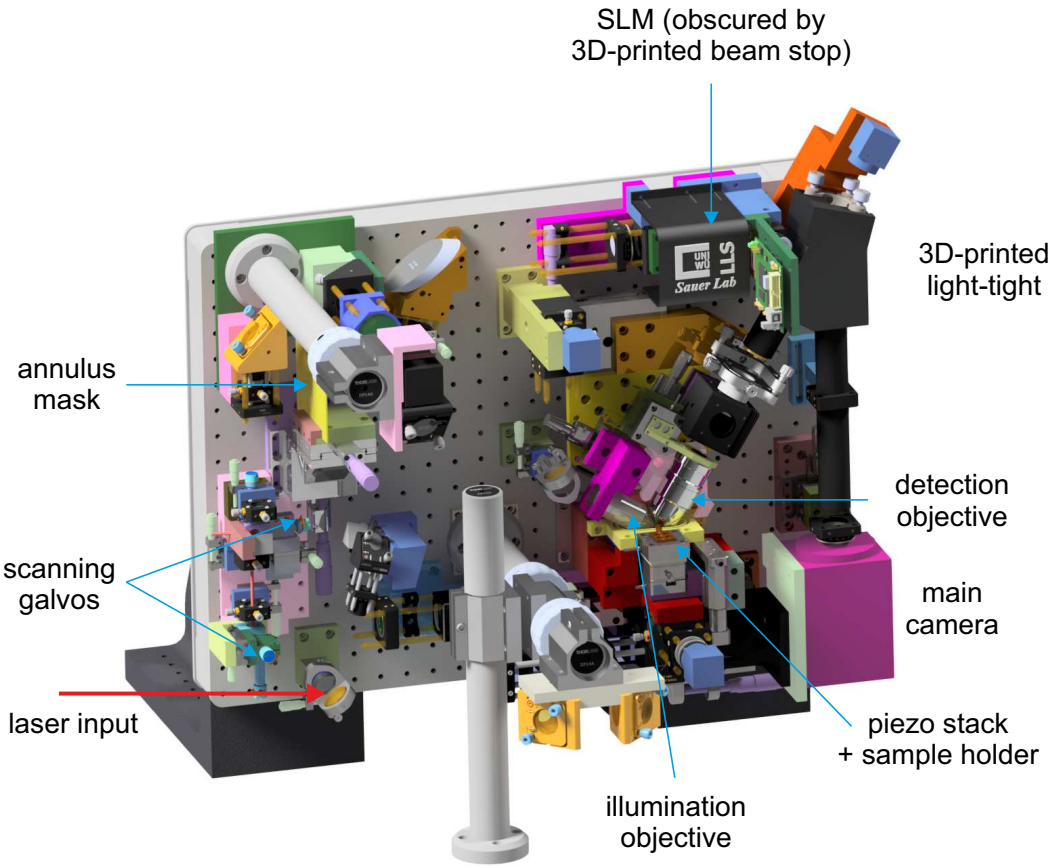

Figure A.1.: Rendering of the optimechanical 3D model of the LLSM. All components are mounted to a vertical optical breadboard to enable a water dipping objective configuration. I have designed some 3D printed parts to further improve the systems laser safety and light-tightness.

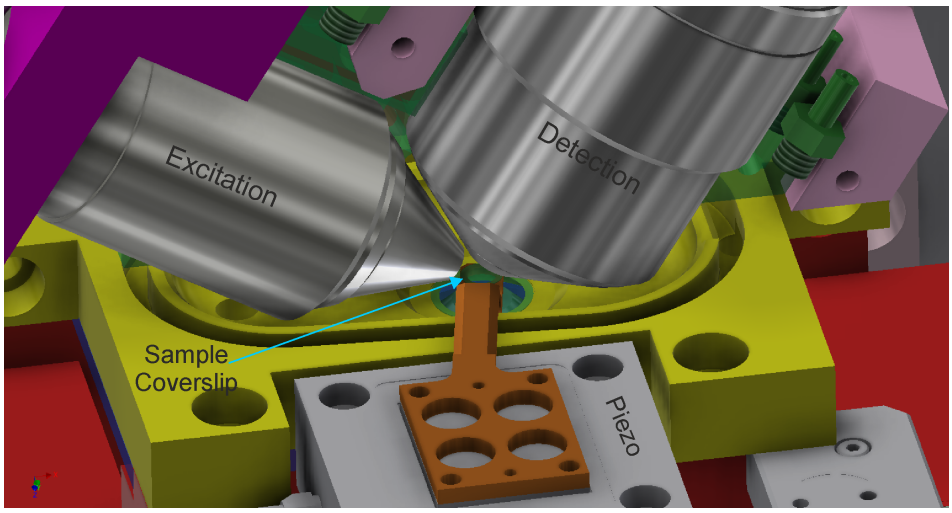

Figure A.2.: Close-up rendering of the sample chamber with the sample mounted on the tip of the sample holder (orange), which is submerged in the sample bath (yellow) that is filled with medium. The window in the bottom of the sample chamber is visible, allowing access for the epi objective.

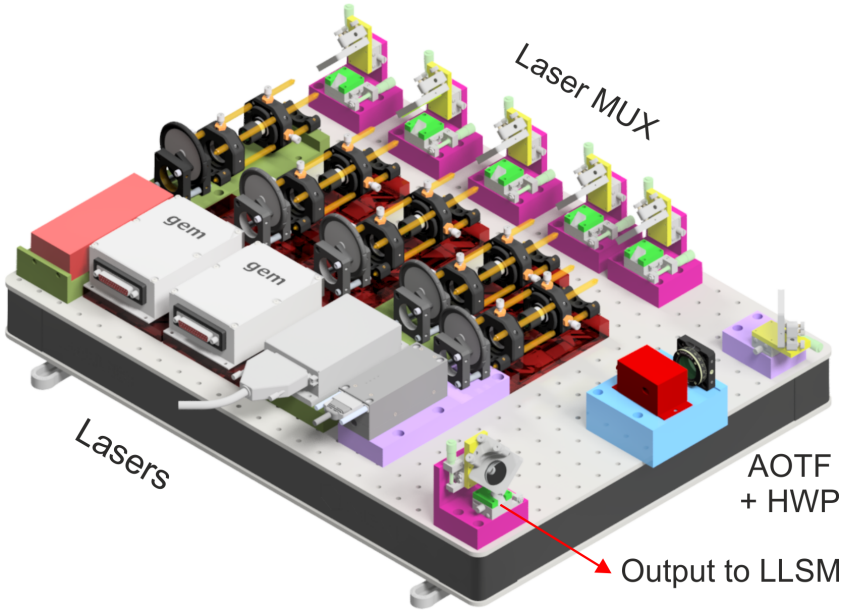

Figure A.3.: Laser combiner serving the LLSM. Shown are the four lasers used in this thesis (in descending order of wavelength from top to bottom) and an additional 405 nm laser that was planned to be used as well.

Table A.1.: Parts of the LLSM related to light generation, filtering and modulation.

Part	Manufacturer
Lasers	
2RU-VFL-P-2000-647-B1R 647 nm, 2000 mW laser	MPB Communications
Gem 561 nm, 500 mW laser with SMD12 driver	Laser Quantum
Gem 532 nm, 500 mW laser with SMD12 driver	Laser Quantum
Sapphire 488-300 CW CDRH 488 nm, 300 mW laser	Coherent
Spectral Filters	
ZET642/20x clean-up filter for 647 nm laser	Chroma
ZET561/10x clean-up filter for 561 nm laser	Chroma
ZET532/10x clean-up filter for 532 nm laser	Chroma
ZET488/10x clean-up filter for 488 nm laser	Chroma
LM01-503 LaserMUX for 488 nm laser	Semrock
LM01-552 LaserMUX for 532 nm laser	Semrock
LM01-613 LaserMUX for 561 nm laser	Semrock
ZT405/488/561/640RPC-UF1 dichroid	Chroma
ZET405/488/561/640M emission filter	Chroma
Di03-R405/488/532/635-t1 dichroid	Semrock
FF01-446/510/581/703 emission filter	Semrock
ET525/50m band pass emission filter	Chroma
ET595/50m band pass emission filter	Chroma
ET655lp long pass emission filter	Chroma
Laser Combination and Modulation	
AOTF.nC-400.650-TN acousto-optical tunable filter	AA Opto Electronic
MPDS8C-B66-22-74.158-RS synthesizer for AOTF	AA Opto Electronic
AHWP3 Halfwave Achromatic retarder plates	Bolder Vision Optik

Table A.2.: Key parts of the LLSM.

Part	Manufacturer
Spatial Light Modulator, Annulus Mask & Galvanometer Scanners	
QXGA-3DM-STR SLM	Forth Dimension Displays
Annulus Mask	Photo Sciences Inc.
8315K scanners with 671-1HP-FS60 servo drivers	Cambridge Technology
Key Electronic Components	
PCIe-7852R FPGA high-speed signal-processing card	National Instruments
SIM900 Mainframe	Stanford Research Systems
SIM983 Scaling Amplifier	Stanford Research Systems
Sample and Objective Positioning	
Piezos and Motorized Stage	Physik Instrumente
P-621.1CD 100 µm piezo for sample and detection objective scanning	Physik Instrumente
E-625.CR driver for P-621.1CD	Physik Instrumente
U-521.24 piezos for sample positioning	Physik Instrumente
C-867.2U2 driver for U-521.24's	Physik Instrumente
M-122.2DD1 linear stepper for sample z positioning	Physik Instrumente
C-863.11 controller for M-122.2DD1	Physik Instrumente
Objectives	
MRD77220 CFI-75 Apo 25x 1.10W WD 2.0 mm infinity-corrected detection objective	Nikon
28.6x 0.7 WI WD 3.74 mm illumination objective	Special Optics Inc.
N2667700 LUMPLFLN 40x 0.8 W epi objective	Olympus
Cameras	
Orca Flash 4.0 V3 C13440 sCMOS Camera	Hamamatsu Photonics
AQ240-Pro water cooling system	innovatek OS
Guppy Pro F-146 CCD Camera	Allied Vision Technology
Miscellaneous Components	
Computer T7910 with 48 threads, 128 GB RAM and GeForce 1080Ti GPU	Dell
Lenses, mirrors and off-the-shelf optomechanical components	Thorlabs & Edmund Optics
Angle plates for vertical mounting of optical breadboard and sample holder	Erwin Halder KG
Heating System	
Precision GP02 water bath	Thermo Scientific
M400K-V micro pump for circulation	TCS Micropumps

Glossary

BFP Back Focal Plane.
CD Cluster of Differentiation.
DLA Diffraction-Limited Area.
DOF Degrees of Freedom.
dSTORM *direct* Stochastic Optical Reconstruction Micropscopy.
EMCCD Electron Multiplying Charge-Coupled Device.
ER Endoplasmic Reticulum.
eV electron Volt, $1\,\mathrm{eV} \approx 1.602 \times 10^{-19}\,\mathrm{J}$.
FFP Front Focal Plane.
FOV Field of View.
FWHM Full Width at Half Maximum.
HBSS Hank's Balanced Salt Solution.
HWP Half Wave Plate.
JIF Jeff's Image Format.
LLSM Lattice Light-Sheet Microscopy / Microscope.
LSM Laser-Scanning Microscope.
NA Numerical Aperture.
NCAM Neural Cell Adhesion Molecule.
NK Natural Killer (cells).
OPL Optical Path Length.
OTF Optical Transfer Function.
PAINT Points Accumulation for Imaging in Nanoscale Topography.
PALM Photoactivated Localization Microscopy.
PBS Phosphate buffered saline.
SAF Supercritical Angle Fluorescence.
sCMOS scientific Complementary Metal-Oxide-Semiconductor.
SIM Structured Illumination Micropscopy / Microscope.
SMLM Single Molecule Localization Microscopy / Miscroscope.
SNR Signal-to-Noise Ratio.
STED Stimualted Emission Depletion.
STORM Stochastic Optical Reconstruction Micropscopy.
TTL Transistor-Transistor Logic.
UV Ultra Violet.

Bibliography

[AAM18] Mostafa Aakhte, Ehsan A. Akhlaghi, and H.-Arno J. Müller. "SSPIM: a beam shaping toolbox for structured selective plane illumination microscopy." In: *Scientific reports* 8.1 (2018), p. 10067. DOI: 10.1038/s41598-018-28389-8.

[Abb73] E. Abbe. "Beiträge zur Theorie des Mikroskops und der mikroskopischen Wahrnehmung." In: *Archiv für Mikroskopische Anatomie* 9.1 (1873), pp. 413–468. DOI: 10.1007/BF02956173.

[All+16] Daniel Allan, Thomas Caswell, Nathan Keim, and Casper van der Wel. *Trackpy: Trackpy V0.3.2*. 2016. DOI: 10.5281/ZENODO.60550.

[Ari+18] Andrey Aristov, Benoit Lelandais, Elena Rensen, and Christophe Zimmer. "ZOLA-3D allows flexible 3D localization microscopy over an adjustable axial range." In: *Nature Communications* 9.1 (2018), p. 1642. DOI: 10.1038/s41467-018-04709-4.

[Axe01] Daniel Axelrod. "Total Internal Reflection Fluorescence Microscopy in Cell Biology." In: *Traffic* 2.11 (2001), pp. 764–774. DOI: 10.1034/j.1600-0854.2001.21104.x.

[Bab19] Hazen Babcock. *storm-analysis*. Github Repository. 2019. URL: https://github.com/ZhuangLab/storm-analysis (visited on 01/14/2019).

[Bab18] Hazen P. Babcock. "Multiplane and Spectrally-Resolved Single Molecule Localization Microscopy with Industrial Grade CMOS cameras." In: *Scientific reports* 8.1 (2018), p. 1726. DOI: 10.1038/s41598-018-19981-z.

[BSZ12] Hazen Babcock, Yaron M. Sigal, and Xiaowei Zhuang. "A high-density 3D localization algorithm for stochastic optical reconstruction microscopy." In: *Optical Nanoscopy* 1.1 (2012), p. 6. DOI: 10.1186/2192-2853-1-6.

[BBZ05] Mark Bates, Timothy R. Blosser, and Xiaowei Zhuang. "Short-Range Spectroscopic Ruler Based on a Single-Molecule Optical Switch." In: *Physical Review Letters* 94.10 (2005), p. 108101. DOI: 10.1103/PhysRevLett.94.108101.

[Bau+16] Florian Baumgart, Andreas M. Arnold, Konrad Leskovar, Kaj Staszek, Martin Fölser, Julian Weghuber, Hannes Stockinger, and Gerhard J. Schütz. "Varying label density allows artifact-free analysis of membrane-protein nanoclusters." In: *Nature methods* 13.8 (2016), pp. 661–664. DOI: 10.1038/nmeth.3897.

[Bet95] E. Betzig. "Proposed method for molecular optical imaging." In: *Optics Letters* 20.3 (1995), pp. 237–239. DOI: 10.1364/OL.20.000237.

[Bet16] E. Betzig. "Bessel Beam Plane Illumination Microscope." United States Patent US9448395. Howard Hughes Medical Institute, Ashburn, VA. 2016.

[Bet05a] Eric Betzig. "Excitation strategies for optical lattice microscopy." In: *Optics Express* 13.8 (2005), pp. 3021–3036. DOI: 10.1364/OPEX.13.003021.

[Bet05b] Eric Betzig. "Sparse and composite coherent lattices." In: *Physical Review A* 71.6 (2005). DOI: 10.1103/PhysRevA.71.063406.

[BW18] Eric. Betzig and Kai Wang. "Structured Plane Illumination Microscopy." United States Patent US10051240B2. Howard Hughes Medical Institute, Ashburn, VA. 2018.

[Bet+06] Eric Betzig, George H. Patterson, Rachid Sougrat, O. Wolf Lindwasser, Scott Olenych, Juan S. Bonifacino, Michael W. Davidson, Jennifer Lippincott-Schwartz, et al. "Imaging intracellular fluorescent proteins at nanometer resolution." In: *Science (New York, N.Y.)* 313.5793 (2006), pp. 1642–1645. DOI: 10.1126/science.1127344.

[Bir17] Udo J. Birk. *Super-resolution microscopy. A practical guide*. Mainz: Wiley-VCH, 2017. ISBN: 9783527341337.

[BW93] Max Born and Emil Wolf. *Principles of optics. Electromagnetic theory of propagation, interference and diffraction of light*. 6. ed., reprinted (with corrections). Oxford: Pergamon Press, 1993. ISBN: 0080264824.

[Bou+15] N. Bourg, C. Mayet, G. Dupuis, T. Barroca, P. Bon, S. Lécart, E. Fort, and S. Lévêque-Fort. "Direct optical nanoscopy with axially localized detection." In: *Nature Photonics* 9.9 (2015), pp. 587–593. DOI: 10.1038/nphoton.2015.132.

[Bra00] Ronald Newbold Bracewell. *The Fourier transform and its applications*. 3. ed., internat. ed. McGraw-Hill series in electrical and computer engineering. Boston, Mass.: McGraw Hill, 2000. ISBN: 0073039381.

[Cha+17] Jae-Byum Chang, Fei Chen, Young-Gyu Yoon, Erica E. Jung, Hazen Babcock, Jeong Seuk Kang, Shoh Asano, Ho-Jun Suk, et al. "Iterative expansion microscopy." In: *Nature methods* 14.6 (2017), p. 593. DOI: 10.1038/nmeth.4261.

[Cha+18] Bo-Jui Chang, Mark Kittisopikul, Kevin M. Dean, Philippe Roudot, Erik Welf, and Reto P. Fiolka. *Universal Light-Sheet Generation with Field Synthesis*. 2018. DOI: 10.1101/427468.

[Che+14] B.-C. Chen, W. R. Legant, K. Wang, L. Shao, D. E. Milkie, M. W. Davidson, C. Janetopoulos, X. S. Wu, et al. "Lattice light-sheet microscopy: Imaging molecules to embryos at high spatiotemporal resolution // Lattice light-sheet microscopy: imaging molecules to embryos at high spatiotemporal resolution." In: *Science* 346.6208 (2014), p. 1257998. DOI: 10.1126/science.1257998.

[CTB15] Fei Chen, Paul W. Tillberg, and Edward S. Boyden. "Expansion microscopy." Optical imaging. In: *Science* 347.6221 (2015), pp. 543–548. DOI: 10.1126/science.1260088.

[Coo00] Geoffrey M. Cooper. *The Cell: A Molecular Approach*. Sinauer Associates, 2000.

[CG96] John C. Crocker and David G. Grier. "Methods of Digital Video Microscopy for Colloidal Studies." In: *Journal of Colloid and Interface Science* 179.1 (1996), pp. 298–310. DOI: 10.1006/jcis.1996.0217.

[Dem13] Wolfgang Demtröder. *Molekülphysik. Theoretische Grundlagen und experimentelle Methoden*. 2nd ed. München: Oldenbourg, 2013. ISBN: 9783486706789. DOI: 10.1524/9783486714890.

[Dem17] Wolfgang Demtröder. *Experimentalphysik 2. Elektrizität und Optik*. 7., korrigierte und erweiterte Auflage. Springer-Lehrbuch. Berlin, Heidelberg: Springer, 2017. ISBN: 9783662557891. DOI: 10.1007/978-3-662-55790-7.

[DMR14] Joran Deschamps, Markus Mund, and Jonas Ries. "3D superresolution microscopy by supercritical angle detection." In: *Optics Express* 22.23 (2014), pp. 29081–29091. DOI: 10.1364/OE.22.029081.

[DSM17] Alex von Diezmann, Yoav Shechtman, and W. E. Moerner. "Three-Dimensional Localization of Single Molecules for Super-Resolution Imaging and Single-Particle Tracking." In: *Chemical reviews* 117.11 (2017), pp. 7244–7275. DOI: 10.1021/acs.chemrev.6b00629.

[Dur87] J. Durnin. "Exact solutions for nondiffracting beams I The scalar theory." In: *Journal of the Optical Society of America A* 4.4 (1987), p. 651. DOI: 10.1364/JOSAA.4.000651.

[DJE87] J. Durnin, J. J. Miceli JR, and J. H. Eberly. "Diffraction-free beams." In: *Physical Review Letters* 58.15 (1987), p. 1499. DOI: 10.1103/PhysRevLett.58.1499.

[DME88] J. Durnin, Miceli, Jr., J. J., and J. H. Eberly. "Comparison of Bessel and Gaussian beams." In: *Optics Letters* 13.2 (1988), pp. 79–80. DOI: 10.1364/OL.13.000079.

[Ein05] A. Einstein. "Über einen die Erzeugung und Verwandlung des Lichtes betreffenden heuristischen Gesichtspunkt." In: *Annalen der Physik* 322.6 (1905), pp. 132–148. DOI: 10.1002/andp.19053220607.

[FR10] Florian O. Fahrbach and Alexander Rohrbach. "A line scanned light-sheet microscope with phase shaped self-reconstructing beams." In: *Optics Express* 18.23 (2010), pp. 24229–24244. DOI: 10.1364/OE.18.024229.

[FR12] Florian O. Fahrbach and Alexander Rohrbach. "Propagation stability of self-reconstructing Bessel beams enables contrast-enhanced imaging in thick media." In: *Nature Communications* 3 (2012), p. 632. DOI: 10.1038/ncomms1646.

[FSR10] Florian O. Fahrbach, Philipp Simon, and Alexander Rohrbach. "Microscopy with self-reconstructing beams." In: *Nature Photonics* 4.11 (2010), pp. 780–785. DOI: 10.1038/nphoton.2010.204.

[FSv16] Christian Franke, Markus Sauer, and Sebastian van de Linde. "Photometry unlocks 3D information from 2D localization microscopy data." In: *Nature methods* (2016). DOI: 10.1038/nmeth.4073.

[Fuc+02] Eran Fuchs, Jules Jaffe, Richard Long, and Farooq Azam. "Thin laser light sheet microscope for microbial oceanography." In: *Optics Express* 10.2 (2002), p. 145. DOI: 10.1364/OE.10.000145.

[Gah+13] Andreas Gahlmann, Jerod L. Ptacin, Ginni Grover, Sean Quirin, Alexander R. S. von Diezmann, Marissa K. Lee, Mikael P. Backlund, Lucy Shapiro, et al. "Quantitative multicolor subdiffraction imaging of bacterial protein ultrastructures in three dimensions." In: *Nano letters* 13.3 (2013), pp. 987–993. DOI: 10.1021/nl304071h.

[Gam+19] Davide Gambarotto, Fabian U. Zwettler, Maeva Le Guennec, Marketa Schmidt-Cernohorska, Denis Fortun, Susanne Borgers, Jörn Heine, Jan-Gero Schloetel, et al. "Imaging cellular ultrastructures using expansion microscopy (U-ExM)." In: *Nature methods* 16.1 (2019), p. 71. DOI: 10.1038/s41592-018-0238-1.

[Gao+14] Liang Gao, Lin Shao, Bi-Chang Chen, and Eric Betzig. "3D live fluorescence imaging of cellular dynamics using Bessel beam plane illumination microscopy." In: *Nature protocols* 9.5 (2014), pp. 1083–1101. DOI: 10.1038/nprot.2014.087.

[GL92] Sarah Frisken Gibson and Frederick Lanni. "Experimental test of an analytical model of aberration in an oil-immersion objective lens used in three-dimensional light microscopy." In: *JOSA A* 9.1 (1992), pp. 154–166. DOI: 10.1364/JOSAA.9.000154.

[Goo17] Joseph W. Goodman. *Introduction to fourier optics*. Fourth edition. New York: W.H. Freeman Macmillan learning, 2017. ISBN: 9781319119164.

[Gus00] M. G. L. Gustafsson. "Surpassing the lateral resolution limit by a factor of two using structured illumination microscopy." In: *Journal of Microscopy* 198.2 (2000), pp. 82–87. DOI: 10.1046/j.1365-2818.2000.00710.x.

[GPM18] Anna-Karin Gustavsson, Petar N. Petrov, and W. E. Moerner. "Light sheet approaches for improved precision in 3D localization-based super-resolution imaging in mammalian cells [Invited]." In: *Optics Express* 26.10 (2018), p. 13122. DOI: 10.1364/OE.26.013122.

[Hec17] Eugene Hecht. *Optics*. 5 ed/fifth edition, Global edition. Pearson global edition. Boston, Columbus, and Indianapolis: Pearson, 2017. ISBN: 9780133977226.

[Hei+02] Mike Heilemann, Dirk P. Herten, Rainer Heintzmann, Christoph Cremer, Christian Müller, Philip Tinnefeld, Kenneth D. Weston, Jürgen Wolfrum, et al. "High-Resolution Colocalization of Single Dye Molecules by Fluorescence Lifetime Imaging Microscopy." In: *Analytical Chemistry* 74.14 (2002), pp. 3511–3517. DOI: 10.1021/ac025576g.

[Hei+05] Mike Heilemann, Emmanuel Margeat, Robert Kasper, Markus Sauer, and Philip Tinnefeld. "Carbocyanine dyes as efficient reversible single-molecule optical switch." In: *Journal of the American Chemical Society* 127.11 (2005), pp. 3801–3806. DOI: 10.1021/ja044686x.

[Hei+09] Mike Heilemann, Sebastian van de Linde, Anindita Mukherjee, and Markus Sauer. "Super-resolution imaging with small organic fluorophores." In: *Angewandte Chemie (International ed. in English)* 48.37 (2009), pp. 6903–6908. DOI: 10.1002/anie.200902073.

[Hei+08] Mike Heilemann, Sebastian van de Linde, Mark Schuttpelz, Robert Kasper, Britta Seefeldt, Anindita Mukherjee, Philip Tinnefeld, and Markus Sauer. "Subdiffraction-resolution fluorescence imaging with conventional fluorescent probes." In: *Angewandte Chemie (International ed. in English)* 47.33 (2008), pp. 6172–6176. DOI: 10.1002/anie.200802376.

[HC99] Rainer Heintzmann and Christoph G. Cremer. "Laterally modulated excitation microscopy: improvement of resolution by using a diffraction grating." In: *Proc. SPIE* 3568 (1999), pp. 185–196. DOI: 10.1117/12.336833.

[HH17] Rainer Heintzmann and Thomas Huser. "Super-Resolution Structured Illumination Microscopy." In: *Chemical reviews* 117.23 (2017), pp. 13890–13908. DOI: 10.1021/acs.chemrev.7b00218.

[HW94] Stefan W. Hell and Jan Wichmann. "Breaking the diffraction resolution limit by stimulated emission: stimulated-emission-depletion fluorescence microscopy." In: *Optics Letters* 19.11 (1994), p. 780. DOI: 10.1364/OL.19.000780.

[HM17] Ekbert Hering and Rolf Martin. *Optik für Ingenieure und Naturwissenschaftler. Grundlagen und Anwendungen, Tabellen, Beispielen.* München: Fachbuchverlag Leipzig im Carl Hanser Verlag, 2017. ISBN: 9783446445093.

[Her45a] J. F. W. Herschel. "Formula No. I. On a Case of Superficial Colour Presented by a Homogeneous Liquid Internally Colourless." In: *Philosophical Transactions of the Royal Society of London* 135.0 (1845), pp. 143–145. DOI: 10.1098/rstl.1845.0004.

[Her45b] J. F. W. Herschel. "Formula No. II. On the Epipolic Dispersion of Light, Being a Supplement to a Paper Entitled, "On a Case of Superficial Colour Presented by a Homogeneous Liquid Internally Colourless"." In: *Philosophical Transactions of the Royal Society of London* 135.0 (1845), pp. 147–153. DOI: 10.1098/rstl.1845.0005.

[HGM06] Samuel T. Hess, Thanu P.K. Girirajan, and Michael D. Mason. "Ultra-High Resolution Imaging by Fluorescence Photoactivation Localization Microscopy." In: *Biophysical Journal* 91.11 (2006), pp. 4258–4272. DOI: 10.1529/biophysj.106.091116.

[HUK11] Seamus J. Holden, Stephan Uphoff, and Achillefs N. Kapanidis. "DAOSTORM: an algorithm for high- density super-resolution microscopy." In: *Nature methods* 8.4 (2011), p. 279. DOI: 10.1038/nmeth0411-279.

[HS16] Seamus Holden and Daniel Sage. "Imaging: Super-resolution fight club." In: *Nature Photonics* 10.3 (2016), p. 152. DOI: 10.1038/nphoton.2016.22.

[HMS07] Laurent Holtzer, Tobias Meckel, and Thomas Schmidt. "Nanometric three-dimensional tracking of individual quantum dots in cells." In: *Applied Physics Letters* 90.5 (2007), p. 053902. DOI: 10.1063/1.2437066.

[HCL16] Ying S. Hu, Hu Cang, and Björn F. Lillemeier. "Superresolution imaging reveals nanometer- and micrometer-scale spatial distributions of T-cell receptors in lymph nodes." In: *Proceedings of the National Academy of Sciences of the United States of America* 113.26 (2016), pp. 7201–7206. DOI: 10.1073/pnas.1512331113.

[Hua+08a] Bo Huang, Sara A. Jones, Boerries Brandenburg, and Xiaowei Zhuang. "Whole-cell 3D STORM reveals interactions between cellular structures with nanometer-scale resolution." In: *Nature Methods* 5.12 (2008), pp. 1047–1052. DOI: 10.1038/nmeth.1274.

[Hua+08b] Bo Huang, Wenqin Wang, Mark Bates, and Xiaowei Zhuang. "Three-dimensional super-resolution imaging by stochastic optical reconstruction microscopy." In: *Science* 319.5864 (2008), pp. 810–813. DOI: 10.1126/science.1153529.

[Hua+18] Xiaoshuai Huang, Junchao Fan, Liuju Li, Haosen Liu, Runlong Wu, Yi Wu, Lisi Wei, Heng Mao, et al. "Fast, long-term, super-resolution imaging with Hessian structured illumination microscopy." In: *Nature biotechnology* 36.5 (2018), p. 451. DOI: 10.1038/nbt.4115.

[Hui+04] J. Huisken, J. Swoger, F. Del Bene, J. Wittbrodt, and Stelzer, Ernst H. K. "Optical sectioning deep inside live embryos by selective plane illumination microscopy." In: *Science* 305.5686 (2004), pp. 1007–1009.

[HS09] Jan Huisken and Didier Y. R. Stainier. "Selective plane illumination microscopy techniques in developmental biology." In: *Development (Cambridge, England)* 136.12 (2009), pp. 1963–1975. DOI: 10.1242/dev.022426.

[Ize+12] Ignacio Izeddin, Mohamed El Beheiry, Jordi Andilla, Daniel Ciepielewski, Xavier Darzacq, and Maxime Dahan. "PSF shaping using adaptive optics for three-dimensional single-molecule super-resolution imaging and tracking." In: *Optics Express* 20.5 (2012), pp. 4957–4967. DOI: 10.1364/OE.20.004957.

[Jue+08] Manuel F. Juette, Travis J. Gould, Mark D. Lessard, Michael J. Mlodzianoski, Bhupendra S. Nagpure, Brian T. Bennett, Samuel T. Hess, and Joerg Bewersdorf. "Three-dimensional sub–100 nm resolution fluorescence microscopy of thick samples." In: *Nature methods* 5.6 (2008), p. 527. DOI: 10.1038/nmeth.1211.

[Kan+10] Pakorn Kanchanawong, Gleb Shtengel, Ana M. Pasapera, Ericka B. Ramko, Michael W. Davidson, Harald F. Hess, and Clare M. Waterman. "Nanoscale architecture of integrin-based cell adhesions." In: *Nature* 468.7323 (2010), p. 580. DOI: 10.1038/nature09621.

[KV94] H. P. Kao and A. S. Verkman. "Tracking of single fluorescent particles in three dimensions: use of cylindrical optics to encode particle position." In: *Biophysical Journal* 67.3 (1994), pp. 1291–1300. DOI: 10.1016/S0006-3495(94)80601-0.

[Kel+08] Philipp J. Keller, Annette D. Schmidt, Joachim Wittbrodt, and Ernst H.K. Stelzer. "Reconstruction of Zebrafish Early Embryonic Development by Scanned Light Sheet Microscopy." In: *Science* 322.5904 (2008), pp. 1065–1069. DOI: 10.1126/science.1162493.

[Kir+13] H. Kirshner, F. Aguet, D. Sage, and M. Unser. "3-D PSF fitting for fluorescence microscopy: implementation and localization application." In: *Journal of Microscopy* 249.1 (2013), pp. 13–25. DOI: 10.1111/j.1365-2818.2012.03675.x.

[Kla+00] T. A. Klar, S. Jakobs, M. Dyba, A. Egner, and S. W. Hell. "Fluorescence microscopy with diffraction resolution barrier broken by stimulated emission." In: *Science* 97.15 (2000), pp. 8206–8210. DOI: 10.1073/pnas.97.15.8206.

[KPS14] Teresa Klein, Sven Proppert, and Markus Sauer. "Eight years of single-molecule localization microscopy." In: *Histochemistry and cell biology* 141.6 (2014), pp. 561–575. DOI: 10.1007/s00418-014-1184-3.

[Kul+11] Nikolaj Kulahin, Lars Groth Grunnet, Morten Lundh, Dan Ploug Christensen, Rasmus Jorgensen, Anders Heding, Nils Billestrup, Vladimir Berezin, et al. "Direct demonstration of NCAM cis-dimerization and inhibitory effect of palmitoylation using the BRET2 technique." In: *FEBS letters* 585.1 (2011), pp. 58–64. DOI: 10.1016/j.febslet.2010.11.043.

[Lak06] Joseph R. Lakowicz. *Principles of fluorescence spectroscopy*. 3rd ed. New York: Springer, 2006. ISBN: 0387312781. DOI: 10.1007/978-0-387-46312-4.

[Lam18] Talley J. Lambert. *LLSpy*. Github Repository. 2018. URL: https://github.com/tlambert03/LLSpy (visited on 01/13/2019).

[Leg+16] Wesley R. Legant, Lin Shao, Jonathan B. Grimm, Timothy A. Brown, Daniel E. Milkie, Brian B. Avants, Luke D. Lavis, and Eric Betzig. "High-density three-dimensional localization microscopy across large volumes." In: *Nature methods* 13.4 (2016), pp. 359–365. DOI: 10.1038/nmeth.3797.

[Li+17] Yiming Li, Markus Mund, Philipp Hoess, Ulf Matti, Bianca Nijmeijer, Vilma Jimenez Sabinina, Jan Ellenberg, Ingmar Schoen, et al. *Fast, robust and precise 3D localization for arbitrary point spread functions*. 2017. DOI: 10.1101/172643.

[LC05] Jeff W. Lichtman and José-Angel Conchello. "Fluorescence microscopy." In: *Nature Methods* 2.12 (2005), pp. 910–919. DOI: 10.1038/nmeth817.

[Lid+05] Keith A. Lidke, Bernd Rieger, Thomas M. Jovin, and Rainer Heintzmann. "Superresolution by localization of quantum dots using blinking statistics." In: *Optics Express* 13.18 (2005), pp. 7052–7062. DOI: 10.1364/OPEX.13.007052.

[Lin+17] Ruisheng Lin, Alexander H. Clowsley, Isuru D. Jayasinghe, David Baddeley, and Christian Soeller. "Algorithmic corrections for localization microscopy with sCMOS cameras - characterisation of a computationally efficient localization approach." In: *Optics Express* 25.10 (2017), pp. 11701–11716. DOI: 10.1364/OE.25.011701.

[Luc+13] Giulia M.R. De Luca, Ronald M.P. Breedijk, Rick A.J. Brandt, Christiaan H.C. Zeelenberg, Babette E. de Jong, Wendy Timmermans, Leila Nahidi Azar, Ron A. Hoebe, et al. "Re-scan confocal microscopy: scanning twice for better resolution." In: *Biomedical Optics Express* 4.11 (2013), pp. 2644–2656. DOI: 10.1364/BOE.4.002644.

[MG15] Carlo Manzo and Maria F. Garcia-Parajo. "A review of progress in single particle tracking: from methods to biophysical insights." In: *Reports on progress in physics. Physical Society (Great Britain)* 78.12 (2015), p. 124601. DOI: 10.1088/0034-4885/78/12/124601.

[Mar+17] Koen J. A. Martens, Arjen N. Bader, Sander Baas, Bernd Rieger, and Johannes Hohlbein. "Phasor based single-molecule localization microscopy in 3D (pSMLM-3D): An algorithm for MHz localization rates using standard CPUs." In: *The Journal of Chemical Physics* 148.12 (2017), p. 123311. DOI: 10.1063/1.5005899.

[Mid+08] Claas v. Middendorff, Alexander Egner, Claudia Geisler, StefanW. Hell, and Andreas Schönle. "Isotropic 3D Nanoscopy based on single emitter switching." In: *Optics Express* 16.25 (2008), pp. 20774–20788. DOI: 10.1364/OE.16.020774.

[MK89] W. E. Moerner and L. Kador. "Optical detection and spectroscopy of single molecules in a solid." In: *Physical Review Letters* 62.21 (1989), p. 2535. DOI: 10.1103/PhysRevLett.62.2535.

[Mor+10] Kim I. Mortensen, L. Stirling Churchman, James A. Spudich, and Henrik Flyvbjerg. "Optimized localization analysis for single-molecule tracking and super-resolution microscopy." In: *Nature Methods* 7.5 (2010), pp. 377–381. DOI: 10.1038/nmeth.1447.

[ME10] Claus B. Müller and Jörg Enderlein. "Image scanning microscopy." In: *Physical review letters* 104.19 (2010), p. 198101. DOI: 10.1103/PhysRevLett.104.198101.

[NOG17] Philip R. Nicovich, Dylan M. Owen, and Katharina Gaus. "Turning single-molecule localization microscopy into a quantitative bioanalytical tool." In: *Nature Protocols* 12.3 (2017), p. 453. DOI: 10.1038/nprot.2016.166.

[Nob19] Nobelprize.org. *The Nobel Prize in Chemistry 2014*. 2019. URL: https://www.nobelprize.org/prizes/chemistry/2014/summary/ (visited on 01/05/2019).

[NH06] Lukas Novotny and Bert Hecht. *Principles of nano-optics*. Cambridge: Cambridge University Press, 2006. ISBN: 9780521539883. DOI: 10.1017/CBO9780511813535.

[Ola+18] Omar E. Olarte, Jordi Andilla, Emilio J. Gualda, and Pablo Loza-Alvarez. "Light-sheet microscopy: a tutorial." In: *Advances in Optics and Photonics* 10.1 (2018), pp. 111–179. DOI: 10.1364/AOP.10.000111.

[OAH06] John P. Overington, Bissan Al-Lazikani, and Andrew L. Hopkins. "How many drug targets are there?" In: *Nature reviews. Drug discovery* 5.12 (2006), pp. 993–996. DOI: 10.1038/nrd2199.

[Ove+14] Martin Ovesný, Pavel Křížek, Josef Borkovec, Zdeněk Svindrych, and Guy M. Hagen. "ThunderSTORM: a comprehensive ImageJ plug-in for PALM and STORM data analysis and super-resolution imaging." In: *Bioinformatics (Oxford, England)* 30.16 (2014), pp. 2389–2390. DOI: 10.1093/bioinformatics/btu202.

[Pal+15] Matthieu Palayret, Helen Armes, Srinjan Basu, Adam T. Watson, Alex Herbert, David Lando, Thomas J. Etheridge, Ulrike Endesfelder, et al. "Virtual-'Light-Sheet' Single-Molecule Localisation Microscopy Enables Quantitative Optical Sectioning for Super-Resolution Imaging." In: *PloS one* 10.4 (2015), e0125438. DOI: 10.1371/journal.pone.0125438.

[PCG94] K. I. Petsas, A. B. Coates, and G. Grynberg. "Crystallography of optical lattices." In: *Physical Review A* 50.6 (1994), pp. 5173–5189. DOI: 10.1103/PhysRevA.50.5173.

[Pit+13] Peter G. Pitrone, Johannes Schindelin, Luke Stuyvenberg, Stephan Preibisch, Michael Weber, Kevin W. Eliceiri, Jan Huisken, and Pavel Tomancak. "OpenSPIM: an open-access light-sheet microscopy platform." In: *Nature methods* 10.7 (2013), pp. 598–599. DOI: 10.1038/nmeth.2507.

[Pla+11] Thomas A. Planchon, Liang Gao, Daniel E. Milkie, Michael W. Davidson, James A. Galbraith, Catherine G. Galbraith, and Eric Betzig. "Rapid three-dimensional isotropic imaging of living cells using Bessel beam plane illumination." In: *Nature methods* 8.5 (2011), pp. 417–423. DOI: 10.1038/nmeth.1586.

[Pon+18] Aleks Ponjavic, James McColl, Alexander R. Carr, Ana Mafalda Santos, Klara Kulenkampff, Anna Lippert, Simon J. Davis, David Klenerman, et al. "Single-Molecule Light-Sheet Imaging of Suspended T Cells." In: *Biophysical Journal* 114.9 (2018), pp. 2200–2211. DOI: 10.1016/j.bpj.2018.02.044.

[PH17] Rory M. Power and Jan Huisken. "A guide to light-sheet fluorescence microscopy for multiscale imaging." In: *Nature methods* 14.4 (2017), pp. 360–373. DOI: 10.1038/nmeth.4224.

[Pra+04] Prashant Prabhat, Sripad Ram, E. Sally Ward, and Raimund J. Ober. "Simultaneous imaging of different focal planes in fluorescence microscopy for the study of cellular dynamics in three dimensions." In: *IEEE transactions on nanobioscience* 3.4 (2004), pp. 237–242.

[Pro+14] Sven Proppert, Steve Wolter, Thorge Holm, Teresa Klein, Sebastian van de Linde, and Markus Sauer. "Cubic B-spline calibration for 3D super-resolution measurements using astigmatic imaging." In: *Optics Express* 22.9 (2014), pp. 10304–10316. DOI: 10.1364/OE.22.010304.

[Ray96] Rayleigh. "XV. On the theory of optical images, with special reference to the microscope." In: *Philosophical Magazine Series 5* 42.255 (1896), pp. 167–195. DOI: 10.1080/14786449608620902.

[Ret13] Michael Reth. "Matching cellular dimensions with molecular sizes." In: *Nature immunology* 14.8 (2013), pp. 765–767. DOI: 10.1038/ni.2621.

[RW59] B. Richards and E. Wolf. "Electromagnetic Diffraction in Optical Systems. II. Structure of the Image Field in an Aplanatic System." In: *Proceedings of the Royal Society A: Mathematical, Physical and Engineering Sciences* 253.1274 (1959), pp. 358–379. DOI: 10.1098/rspa.1959.0200.

[RS14] Bernd Rieger and Sjoerd Stallinga. "The lateral and axial localization uncertainty in super-resolution light microscopy." In: *Chemphyschem : a European journal of chemical physics and physical chemistry* 15.4 (2014), pp. 664–670. DOI: 10.1002/cphc.201300711.

[Rie19] Jonas Ries. *SMAP*. Github Repository. 2019. URL: https://github.com/jries/SMAP (visited on 01/13/2019).

[Ros+13] Jérémie Rossy, Dylan M. Owen, David J. Williamson, Zhengmin Yang, and Katharina Gaus. "Conformational states of the kinase Lck regulate clustering in early T cell signaling." In: *Nature immunology* 14.1 (2013), pp. 82–89. DOI: 10.1038/ni.2488.

[RV04] Thomas Ruckstuhl and Dorinel Verdes. "Supercritical angle fluorescence (SAF) microscopy." In: *Optics Express* 12.18 (2004), p. 4246. DOI: 10.1364/OPEX.12.004246.

[RBZ06] Michael J. Rust, Mark Bates, and Xiaowei Zhuang. "Sub-diffraction-limit imaging by stochastic optical reconstruction microscopy (STORM)." In: *Nature methods* 3.10 (2006), p. 793. DOI: 10.1038/nmeth929.

[Sag+18] Daniel Sage, Thanh-An Pham, Hazen Babcock, Tomas Lukes, Thomas Pengo, Jerry Chao, Ramraj Velmurugan, Alex Herbert, et al. "Super-resolution fight club: A broad assessment of 2D & 3D single-molecule localization microscopy software." In: *bioRxiv* (2018). DOI: 10.1101/362517.

[San11] P. A. Santi. "Light Sheet Fluorescence Microscopy: A Review." In: *Journal of Histochemistry & Cytochemistry* 59.2 (2011), pp. 129–138. DOI: 10.1369/0022155410394857.

[Sau13] Markus Sauer. "Localization microscopy coming of age: from concepts to biological impact." In: *Journal of Cell Science* 126.Pt 16 (2013), pp. 3505–3513. DOI: 10.1242/jcs.123612.

[SH17] Markus Sauer and Mike Heilemann. "Single-Molecule Localization Microscopy in Eukaryotes." In: *Chemical reviews* 117.11 (2017), pp. 7478–7509. DOI: 10.1021/acs.chemrev.6b00667.

[Sch+19] Lothar Schermelleh, Alexia Ferrand, Thomas Huser, Christian Eggeling, Markus Sauer, Oliver Biehlmaier, and Gregor P. C. Drummen. "Super-resolution microscopy demystified." In: *Nature Cell Biology* 21.1 (2019), p. 72. DOI: 10.1038/s41556-018-0251-8.

[Sch+12] Johannes Schindelin, Ignacio Arganda-Carreras, Erwin Frise, Verena Kaynig, Mark Longair, Tobias Pietzsch, Stephan Preibisch, Curtis Rueden, et al. "Fiji: an open-source platform for biological-image analysis." In: *Nature Methods* 9.7 (2012), pp. 676–682. DOI: 10.1038/nmeth.2019.

[Sch10] Jason Daniel Schmidt. *Numerical simulation of optical wave propagation.* 1st ed. Bellingham: SPIE, 2010. ISBN: 978-0-8194-8326-3.

[She+14] Yoav Shechtman, Steffen J. Sahl, Adam S. Backer, and W. E. Moerner. "Optimal point spread function design for 3D imaging." In: *Physical review letters* 113.13 (2014), p. 133902. DOI: 10.1103/PhysRevLett.113.133902.

[She+16] Yoav Shechtman, Lucien E. Weiss, Adam S. Backer, Maurice Y. Lee, and W. E. Moerner. "Multicolour localization microscopy by point-spread-function engineering." In: *Nature Photonics* 10.9 (2016), pp. 590–594. DOI: 10.1038/nphoton.2016.137.

[SVR06] Yoko Shibata, Gia K. Voeltz, and Tom A. Rapoport. "Rough Sheets and Smooth Tubules." In: *Cell* 126.3 (2006), pp. 435–439. DOI: 10.1016/j.cell.2006.07.019.

[Sht+09] Gleb Shtengel, James A. Galbraith, Catherine G. Galbraith, Jennifer Lippincott-Schwartz, Jennifer M. Gillette, Suliana Manley, Rachid Sougrat, Clare M. Waterman, et al. "Interferometric fluorescent super-resolution microscopy resolves 3D cellular ultrastructure." In: *Proceedings of the National Academy of Sciences* 106.9 (2009), pp. 3125–3130. DOI: 10.1073/pnas.0813131106.

[SZ02] H. Siedentopf and R. Zsigmondy. "Uber Sichtbarmachung und Größenbestimmung ultramikoskopischer Teilchen, mit besonderer Anwendung auf Goldrubingläser." In: *Annalen der Physik* 315.1 (1902), pp. 1–39. DOI: 10.1002/andp.19023150102.

[SS14] Alex Small and Shane Stahlheber. "Fluorophore localization algorithms for super-resolution microscopy." In: *Nature methods* 11.3 (2014), pp. 267–279. DOI: 10.1038/nmeth.2844.

[Smi+10] Carlas S. Smith, Nikolai Joseph, Bernd Rieger, and Keith A. Lidke. "Fast, single-molecule localization that achieves theoretically minimum uncertainty." In: *Nature methods* 7.5 (2010), pp. 373–375. DOI: 10.1038/nmeth.1449.

[SR10] Sjoerd Stallinga and Bernd Rieger. "Accuracy of the Gaussian Point Spread Function model in 2D localization microscopy." In: *Optics Express* 18.24 (2010), pp. 24461–24476. DOI: 10.1364/OE.18.024461.

[Sto52] G. G. Stokes. "On the Change of Refrangibility of Light." In: *Philosophical Transactions of the Royal Society of London* 142 (1852), pp. 463–562. DOI: 10.1098/rstl.1852.0022.

[TLW02] R. E. Thompson, Larson, and W. W. Webb. "Precise nanometer localization analysis for individual fluorescent probes." In: *Biophysical Journal* 82.5 (2002), pp. 2775–2783. DOI: 10.1016/S0006-3495(02)75618-X.

[TIS08] Makio Tokunaga, Naoko Imamoto, and Kumiko Sakata-Sogawa. "Highly inclined thin illumination enables clear single-molecule imaging in cells." In: *Nature Methods* 5.2 (2008), pp. 159–161. DOI: 10.1038/nmeth1171.

[Tsu+18] Taka A. Tsunoyama, Yusuke Watanabe, Junri Goto, Kazuma Naito, Rinshi S. Kasai, Kenichi G. N. Suzuki, Takahiro K. Fujiwara, and Akihiro Kusumi. "Super-long single-molecule tracking reveals dynamic-anchorage-induced integrin function." In: *Nature chemical biology* 14.5 (2018), pp. 497–506. DOI: 10.1038/s41589-018-0032-5.

[van+11] Sebastian van de Linde, Anna Löschberger, Teresa Klein, Meike Heidbreder, Steve Wolter, Mike Heilemann, and Markus Sauer. "Direct stochastic optical reconstruction microscopy with standard fluorescent probes." In: *Nature protocols* 6.7 (2011), pp. 991–1009. DOI: 10.1038/nprot.2011.336.

[van+98] A.M van Oijen, J. Köhler, J. Schmidt, M. Müller, and G.J Brakenhoff. "3-Dimensional super-resolution by spectrally selective imaging." In: *Chemical Physics Letters* 292.1-2 (1998), pp. 183–187. DOI: 10.1016/S0009-2614(98)00673-3.

[VBS93] A. H. Voie, D. H. Burns, and F. A. Spelman. "Orthogonal-plane fluorescence optical sectioning: Three-dimensional imaging of macroscopic biological specimens." In: *Journal of Microscopy* 170.3 (1993), pp. 229–236. DOI: 10.1111/j.1365-2818.1993.tb03346.x.

[Wäl+15] Sina Wäldchen, Julian Lehmann, Teresa Klein, Sebastian van de Linde, and Markus Sauer. "Light-induced cell damage in live-cell super-resolution microscopy." In: *Scientific reports* 5 (2015), p. 15348. DOI: 10.1038/srep15348.

[Wei+18] Martin Weigert, Uwe Schmidt, Tobias Boothe, Andreas Müller, Alexandr Dibrov, Akanksha Jain, Benjamin Wilhelm, Deborah Schmidt, et al. "Content-aware image restoration: pushing the limits of fluorescence microscopy." In: *Nature methods* 15.12 (2018), p. 1090. DOI: 10.1038/s41592-018-0216-7.

[Wol+10] S. Wolter, M. Schüttpelz, M. Tscherepanow, Sebastian van de Linde, M. Heilemann, and M. Sauer. "Real-time computation of subdiffraction-resolution fluorescence images." In: *Journal of Microscopy* 237.1 (2010), pp. 12–22. DOI: 10.1111/j.1365-2818.2009.03287.x.

[Wol+12] Steve Wolter, Anna Löschberger, Thorge Holm, Sarah Aufmkolk, Marie-Christine Dabauvalle, Sebastian van de Linde, and Markus Sauer. "rapidSTORM: accurate, fast open-source software for localization microscopy." In: *Nature Methods* 9.11 (2012), pp. 1040–1041. DOI: 10.1038/nmeth.2224.

[WS18] Yicong Wu and Hari Shroff. "Faster, sharper, and deeper: structured illumination microscopy for biological imaging." In: *Nature Methods* 18 (2018), p. 685. DOI: 10.1038/s41592-018-0211-z.

[Yor+13] Andrew G. York, Panagiotis Chandris, Damian Dalle Nogare, Jeffrey Head, Peter Wawrzusin, Robert S. Fischer, Ajay Chitnis, and Hari Shroff. "Instant super-resolution imaging in live cells and embryos via analog image processing." In: *Nature methods* 10.11 (2013), pp. 1122–1126. DOI: 10.1038/nmeth.2687.

[Zie+17] Sabrina Ziegler, Esther Weiss, Anna-Lena Schmitt, Jan Schlegel, Anne Burgert, Ulrich Terpitz, Markus Sauer, Lorenzo Moretta, et al. "CD56 Is a Pathogen Recognition Receptor on Human Natural Killer Cells." In: *Scientific reports* 7.1 (2017), p. 6138. DOI: 10.1038/s41598-017-06238-4.

Acknowledgments

Being part of the Department of Biotechnology and Biophysics in Würzburg was a great experience and a time I am going to cherish. For this I am grateful to the people who supported me and made it such a good time.

First of all, I would like to thank Markus Sauer for trusting me with this project, for your support and for the opportunity to participate in many exciting research projects, collaborations and conferences. Your open mind and enthusiasm truly shapes the outstanding atmosphere in this group.

I would also like to thank Bert Hecht for immediately taking the part of second reviewer of my thesis.

To Sören Doose I am grateful for allowing me my first glimpse into the realm of fluorescence microscopy and for many fruitful discussions.

I am grateful to Andreas Kurz, with whom I shared most of my time at the University of Würzburg. Thanks for your friendship and all the productive discussions and activities on and off campus.

For many interesting samples and an introduction to many aspects of biology I would like to thank Jan Schlegel and Gerti Beliu. Your spirit always made measurements worthwhile and kept me going.

To my Master's student Ando Zehrer I am grateful for the good work and wish you all the best for your PhD in Berlin.

For lots of help with manufacturing optomechanical components I am grateful to Albert Gessner, who really stepped out of his way to make this microscope reality. For help with electronic components and computer infrastructure I thank Oliver Reichert. For help with biological sample preparation I thank Lisa Behringer-Pließ and Petra Geßner.

I was very lucky to share the office with Sina, Christian, Andi, Franzi and Fabi. You guys made sure the time in the office never got dull and there was always somebody to discuss problems with.

My time off campus was enriched by many activities with people from the lab, allowing to clear one's head and have lots of fun. Thanks for all the rock climbing, freeriding, bicycle tours, dips in the Main river and everything else! Keep on pushing, Sina, Sebastian, Andrea, Franzi, Juli, Sarah, Lena!

Finally, I want to thank my family for always supporting me through my studies and building a foundation of confidence that I could always lean on. My deepest thanks go to Sina for always having my back, for supporting me when times were rough and for having so much fun with me. You are my best friend and the love of my life.